An optical echo study of caesium-noble gas collisions

Thesis

AN OPTICAL ECHO STUDY OF CAESIUM-NOBLE GAS COLLISIONS

Keith William Godfrey M.A. (Cantab.)

A thesis submitted in partial fulfilment of the requirements for the degree of Doctor of Philosophy in Physics at The Open University.

3 April 1989

Date of Submission: 3rd April 1989
Date of Award : 14th June 1989

ProQuest LLC
789 East Eisenhower Parkway
P.O. Box 1346
Ann Arbor, MI 48106 - 1346

Abstract

The work described in this thesis is an experimental study of collisional relaxation of two-excitation-pulse optical echoes on the caesium 6S-7P transitions perturbed by noble gases using the echo polarisation rotation discrimination technique.

Theoretical preliminaries include the development of a Schrödinger interaction representation theory of the formation of echoes resulting from two resonant excitation pulses applied to a two-state system. Rotation of the echo polarisation enables a polariser to be used to discriminate against the excitation pulses in favour of the echo. To illustrate the mechanisms behind this rotation, a simplified theory based on a nearly degenerate two level system is developed. The theory of collisional relaxation of echoes by phase interrupting and quantum diffractive velocity changing collisions is introduced. In traditional line profile spectroscopy the former type of collision cause line broadening whilst the effects of the latter are unobservable.

The experimental work of this thesis involves the measurement of collisional relaxation of two-excitation-pulse echoes on the caesium $6S_{1/2}$-$7P_{1/2}$ (459nm) and $6S_{1/2}$-$7P_{3/2}$ (455nm) transitions perturbed by low pressure (< 1 torr) of noble gas (He, Ar or Xe). The experiments were carried out using a range of interpulse times from about 30 to 200ns. The broadening constants, determined to about 3% from the relaxation measurements, show significant discrepancies with traditional line profile measurements. For the longer interpulse times there is evidence for the quantum diffractive velocity changing aspects of the collisions. The associated cross-sections and average magnitudes of the mean velocity changes are estimated from the data.

Contents

List of Figures

List of Tables

Acknowledgements

I would like to thank Dr Alan Durrant and Dr Joy Manners who conceived and supervised this research. I also wish to thank Steve Daniels, Andy Boddington, Dr Sue Brooks and Mrs Marilyn Moffat, the computing research advisors, for their help in the production of this manuscript. I would also like to thank Dr Tom Smith for helpful comments concerning theoretical aspects of this thesis. In addition, I wish to thank the physics technical and workshop staff, Nobby Lowndes, Roger Bence and Martin Sydee, for their valuable assistance. I also wish to acknowledge the help of William Dove in obtaining the results of section 5.5.4.

Finally, for their encouragement, support and help I wish to thank my parents.

Prologue

The principle objective of this work was the study of collisional parameters for the caesium $6S_{1/2}$-$7P_{1/2}$ and $6S_{1/2}$-$7P_{3/2}$ transitions perturbed by noble gases. This was undertaken with a view to obtaining broadening constants to add to the existing information and to measure previously undetermined aspects of these collisions.

The method used for these studies employed the two-excitation-pulse echo using the polarisation rotation technique for discrimination. This technique had not previously been routinely used for collisional studies and therefore needed to be established as a valid method of measurement by investigating possible sources of systematic error.

The organisation of this thesis is as follows:

- In chapter 1 traditional collisional theories are outlined. Frequency and time domain spectroscopy are discussed. The two-excitation-pulse echo is introduced in section 1.2.2(ii). This chapter ends with a resumé of the published measurements of broadening constants for the caesium 6S-7P lines perturbed by noble gases (He, Ar and Xe).

- In chapter 2 a simple theory is presented based on a two level atom to describe the formation of the two-excitation-pulse echo. Calculations are performed for the cases of both collinear and non-collinear excitation pulses.

- In chapter 3 the echo polarisation rotation technique is introduced. This technique is the one used in the experiments of chapter 5 to discriminate in favour of the echo. The theoretical analysis of this

chapter is performed on a three level system. This is the most simple system to exhibit polarisation rotation. The analysis is performed on this simple system in order to show the physical mechanisms involved without the need for complicated calculations. Polarisation rotation on the caesium 6S-7P transitions is also briefly discussed.

- In chapter 4 the theory of collisional relaxation is introduced into the echo description. The phase interrupting collisions of chapter 1 are related to echo relaxation in echo spectroscopy. The relaxation rate is then related to the broadening constant. Diffractive velocity changing collisions and their effects are also described.

- In chapter 5 the main work of this thesis is described. This was experimental work to measure collisional relaxation of echoes on the caesium $6S_{1/2}$-$7P_{1/2}$ and $6S_{1/2}$-$7P_{3/2}$ transitions perturbed by noble gases.

- In chapter 6 possible future work that could be performed on the caesium-noble gas system is described. This includes a discussion of the three-excitation-pulse stimulated echo.

Chapter 1

Collision Studies In Gases

By studying collisions in gases information about atomic 'sizes', the collisional cross sections, can be deduced. The spectral line broadening constant is a parameter that succinctly expresses certain experimental aspects of spectroscopic collisional studies. The role of this constant is the main subject of this chapter which is organised as follows. In section 1.1 spectral line shapes in low pressure gases are discussed. In section 1.2 frequency and time domain spectroscopy are briefly reviewed. Doppler-free techniques are also discussed in this section. Finally, in section 1.3 a resumé is given of the published measurements of broadening constants for the caesium 6S-7P lines perturbed by noble gases.

1.1 Theoretical Background

1.1.1 Spectral line shapes

An elementary discussion of spectral line shapes is now given to establish some notation and conventions. Reviews can be found by many authors [15, 22, 55, 67, 88]. To a good approximation a single atom will absorb and emit radiation at fairly well defined frequencies giving rise to spectral lines in absorption and emission respectively. On close inspection any spectral line will be seen to be composed of a spread of frequencies. The intensity of any line varies over this range of frequencies giving the line a shape or profile. At sufficiently low pressures the profile is symmetrical and centred at or near

the frequency, ν_0, corresponding to the energy difference between the upper and lower energy levels of the transition, E_u and E_l,

$$\nu_0 = \frac{E_u - E_l}{h}$$

with a spread or broadening that can be characterised by a half width, $\delta\nu$, which is half the frequency width at half the maximum intensity, where

$$\delta\nu = \frac{\nu_2 - \nu_1}{2} \quad \text{with} \quad I(\nu_1) = I(\nu_2) = I(\nu_0)/2$$

$I(\nu)$ being the intensity at frequency ν. The range of frequencies within $\delta\nu$ of ν_0 is called the line centre or the line core and the outer parts are called wings (see figure 1.1). The three main causes of line broadening are now discussed.

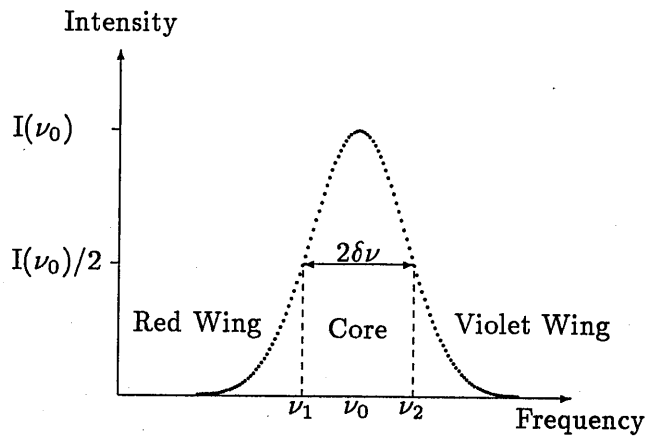

Figure 1.1 A spectral line profile.

(i) Natural broadening

In a classical description, a freely radiating atom can be considered as a damped oscillating electric dipole, with the magnitude of the radiated dipole field having the form

$$E(t) \propto \exp(-t/2\tau_0)\sin(2\pi\nu_0 t)$$

where τ_0 $(\gg 1/\nu_0)$ is the lifetime. Fourier analysis shows the intensity of

the emitted radiation to have a Lorentzian frequency profile

$$\mathrm{I}(\nu) \propto \frac{1}{(\nu - \nu_0)^2 + (\delta\nu_{\mathrm{natural}})^2}$$

where $\delta\nu_{\mathrm{natural}}$ is the natural half width at half the maximum intensity of the line and is related to the lifetime, τ_0, by

$$\delta\nu_{\mathrm{natural}} = 1/4\pi\tau_0$$

The natural broadening of a particular transition is the same for all atoms and is therefore an example of what is called homogeneous broadening. Though fundamental to any radiative transition, natural broadening is usually obscured by other types of broadening.

(ii) Doppler broadening

The process that usually provides the largest contribution to the observed broadening of a spectral line is the Doppler effect which causes the observed frequency, ν, of a moving oscillator to be shifted in proportion to its line-of-sight velocity component towards the observer, v,

$$\nu = (1 + \mathrm{v}/\mathrm{c})\nu_0 \qquad (\mathrm{v}/\mathrm{c} \ll 1)$$

where ν_0 is the frequency of a stationary oscillator and c the speed of light. The atoms of a gas in thermal equilibrium will have a Gaussian distribution of velocity components. In the absence of other broadening mechanisms, the spectrum emitted by a set of oscillators with such a Gaussian distribution of velocity components would be broadened with a Gaussian profile,

$$\mathrm{I}(\nu) \propto \exp -\{(\nu - \nu_0)^2 \log_e 2/(\delta\nu_{\mathrm{Doppler}})^2\}$$

where $\delta\nu_{\mathrm{Doppler}}$ is the half width at half the maximum intensity of the Doppler profile. It is related to the thermal equilibrium temperature of the gas, T, by

$$\delta\nu_{\mathrm{Doppler}} = \frac{\nu_0}{\mathrm{c}}\sqrt{\frac{2k_BT\log_e 2}{M}}$$

where M is the atomic mass and k_B is Boltzmann's constant. The intensity at each frequency arises from a subgroup of the oscillators moving with a

specific velocity component. This type of broadening is called inhomogeneous. A spectral line that is Doppler broadened is, of course, also subject to natural broadening. This leads to the line shape being a convolution of the Lorentzian and Gaussian profiles. This shape is called a Voigt profile and is basically shaped like a Lorentzian in the wings and a Gaussian in the core region.

(iii) Pressure broadening

Collisions between atoms or molecules in a gas influence the width, central frequency and shape of spectral lines. Details of some of the mechanisms involved will be discussed in section 1.1.2. At very high pressures, of order atmospheres, the profiles develop asymmetries and other complex features. At low pressures the main features are a Lorentzian broadening, of half width $\delta\nu_{\text{pressure}}$, and a shift, δ, of the line away from ν_0. In the absence of Doppler broadening, the overall line shape is then

$$\mathrm{I}(\nu) \propto \frac{1}{(\nu - \nu_0 - \delta)^2 + (\delta\nu_{\text{pressure}})^2}$$

Comparison of the different types of line broadening

Spectral lines at low pressures are usually dominated by Doppler broadening. This can be seen by considering the full widths at half height of the three main types of broadening for a typical optical transition. The 6S-7P transition in caesium is taken as an example and gives, to order of magnitude,

$$\delta\nu_{\text{natural}} \sim 10^6\text{Hz} \quad \delta\nu_{\text{pressure}} \sim 10^8\text{Hz} \quad \delta\nu_{\text{Doppler}} \sim 10^9\text{Hz}$$

where room temperature and a torr of foreign gas are taken as typical experimental conditions.

As can be seen from figure 1.2, a Lorentzian profile has a greater amplitude in the wings than a Gaussian profile of the same area and half width. Traditional spectroscopic studies of pressure broadening therefore concentrate on the wings of the spectral line and use relatively high pressures

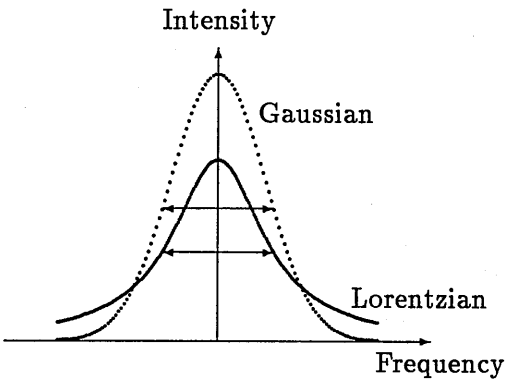

Figure 1.2 Comparison of Lorentzian and Gaussian profiles with equal areas and half widths.

($\gg$1 torr), see section 1.2.1(i). The use of Doppler-free laser spectroscopic techniques can eliminate the obscuring effects of Doppler broadening so that collisional studies can be carried out at very low pressures (<1 torr), see sections 1.2.1(ii) and 1.2.2(ii).

1.1.2 Classical theory of low pressure collisional mechanisms

In this work only elastic collisions between a radiating atom (active atom) and a neutral atom of a different species, a foreign gas atom in its ground state, (perturber atom) are considered. Inelastic collisions, where an atom is excited to a different state by the collision, are negligible if the states to which an atom could be excited are well separated in comparison with thermal energies. Collisions with charged particles and with atoms of the same species, involving resonant energy exchanges, are not relevant to this work. The effects of resonant collisions can be made negligible by working with the number density of the active atoms very much lower than that of the perturber atoms (typically 1:10^6). Active atom-perturber atom collisions will then dominate the line broadening. Furthermore in this work only the case of low pressures of perturber gas will be considered. General reviews are given by many authors [19, 33, 48, 65, 80, 86] and state that at low pressures ($<$ 1 torr) the impact and binary approximations are valid. The impact approximation states that the average time between collisions, T_{coll},

is very much greater than the average duration of collisions, t_{coll}.

$$T_{coll} \gg t_{coll}$$

The binary approximation states that only one perturber atom interacts with an active atom during a collision. This simplifies the analysis because then only one distance parameter is required: that between the atomic centres.

The first significant analysis of pressure broadening was performed in 1895 by Michelson [66], who assumed that the atoms followed classical rectilinear trajectories and that the broadening was due to collisions causing phase interruptions of the oscillations. In 1906 Lorentz [61] showed that the effects on the radiation of collisions were equivalent to a damping, proportional to velocity, exerted on the oscillating electrons. The line profile then has the familiar Lorentzian form. In 1932 Weisskopf [92] provided a mechanism for the collisional phase interruptions. He assumed that the upper and lower energy levels of the transition, E_u and E_l, are generally perturbed by different amounts in a collision and so the oscillation frequency, $\nu_0 = (E_u - E_l)/h$, varies slightly during the collision (see figure 1.3). A collision, typically of duration $t_{coll} \sim 10^{-11}$s, lasts many optical periods ($\nu^{-1} \sim 10^{-14}$s). During a collision the oscillator radiates at a varying frequency and this leads to an accumulated phase change. Weisskopf [92] distinguished between collisions with small impact parameters where the total accumulated phase change is larger than 1 radian, called *phase interrupting collisions*, and large impact parameter collisions where the phase change is less than 1 radian. The critical impact parameter separating these two regimes is called the Weisskopf radius, b_W. For small impact parameter collisions ($b < b_W$) the phase is effectively randomised by the collision and a Fourier analysis of the resulting wave train has a Lorentzian frequency distribution with a half width, $\delta\nu_{\text{pressure}}$, related to the average time between collisions, T_{coll}, by $\delta\nu_{\text{pressure}} = 1/2\pi T_{coll}$. For the large impact parameter collisions ($b > b_W$) the small phase change is unidirectional, and leads to a frequency shift, δ, of the line. Hence the overall line shape is a shifted

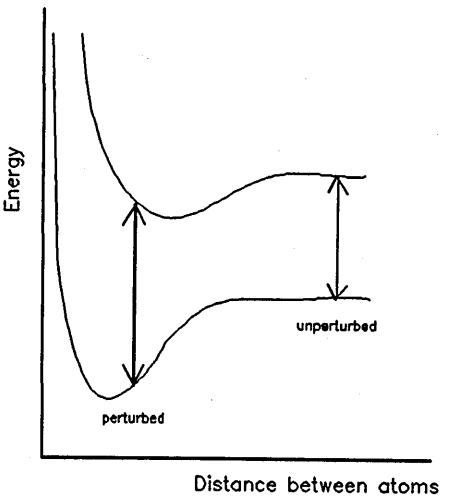

Figure 1.3 Energy levels plotted against atomic separation. Different transition energies, and hence frequencies, are indicated at two distinct atomic separations.

Lorentzian

$$\mathrm{I}(\nu) \propto \frac{1}{(\nu - \nu_0 - \delta)^2 + (\delta\nu_{\text{pressure}})^2}$$

where δ is the frequency shift of the central maximum. This formula was first obtained by Lindholm in 1941 [60]. T_{coll} decreases as the pressure increases. Therefore this type of broadening increases with pressure. Indeed in the impact regime a useful parameter, to describe collision broadening, is the broadening constant, γ.

$$\gamma = \frac{\delta\nu_{\text{pressure}}}{N} = \frac{1}{2\pi T_{coll} N} \tag{1.1}$$

where N is the number density of perturber atoms.

In the above analysis the impact approximation is used to justify ignoring the light emitted during collisions. In addition, all atoms are considered equally likely to suffer collisions irrespective of their velocity. More recent calculations [43, 54, 84, 90] do not make these assumptions and predict asymmetric, non-Lorentzian, line shapes. However the alterations introduced by considering these effects are very small for experiments performed well within the impact regime.

1.2 Experimental Approaches

1.2.1 Frequency domain spectroscopy

(i) Traditional line shape measurements

Traditional pressure broadening experiments for measuring broadening, shift and asymmetry have been carried out using the alkali metals as well as other metals as the active atoms. The alkali metals are convenient because a working vapour pressure of about 10^{-5} torr of monatomic gas can be easily obtained in heated ovens or cells. The noble gases are used as the perturber atoms since they will not combine chemically with the very reactive active atoms, are also monatomic and have relatively simple 'filled shell' structures.

Traditionally spectral line shapes have been observed in both absorption and emission using high resolution diffraction gratings [54, 78, 84, 85] or Fabry-Pérot [20] interferometers. Collision broadening studied in the low pressure binary and impact regimes by traditional spectroscopy is complicated because the observed line shape is a convolution of the Gaussian Doppler profile, the instrumental profile, and the collisional line profile which contains the sought-after information: the width, shift and any asymmetry. The deconvolution of the experimentally measured profiles are now usually performed by computer [54]. To reduce the errors introduced by this procedure the pressure broadening must form a substantial part of the experimental profile and so high pressures of perturber gas are usually used. These experiments are therefore not usually performed strictly in the impact and binary regimes. A general review is given by Lewis [59] and references for work on the 6S-7P transitions in caesium can be found in section 1.3.

The problems associated with Doppler broadening can be avoided by the use of non-linear Doppler-free laser spectroscopy. However the traditional techniques are still the only ones applicable to astrophysical studies where the light source is incoherent stellar radiation.

(ii) Doppler-free laser spectroscopy

Developments in non-linear spectroscopy have led to techniques which eliminate or substantially reduce the Doppler broadening, and so allow low pressure collisional interactions to be studied. Two relevant frequency domain Doppler-free techniques are now described.

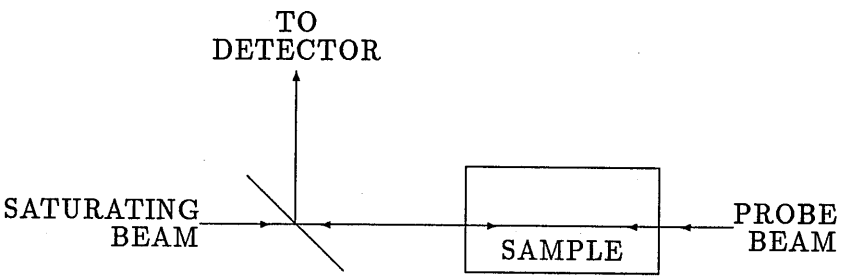

(a)

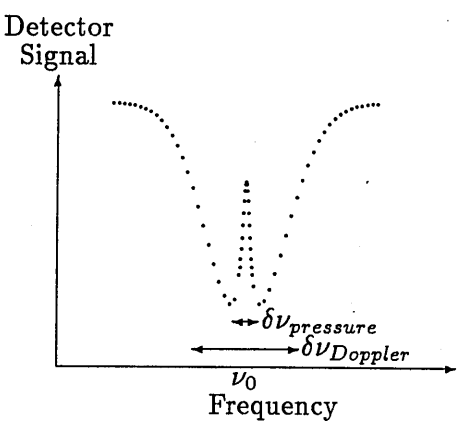

(b)

Figure 1.4 Saturation spectroscopy of sample with resonant frequency ν_0 a) Experimental arrangement and b) Idealised results.

Saturation spectroscopy can be performed by passing anti-parallel laser beams of the same frequency through a vapour (See figure 1.4). When the beams are tuned to a frequency away from a resonant frequency of the vapour neither beam is absorbed significantly and a large transmitted signal

is measured from the weaker of the two beams, called the probe beam. The stronger beam, the saturating beam, is not incident on the detector. With the laser beams tuned to a frequency near resonance, the high intensity beam excites to saturation those atoms that are Doppler shifted into resonance. The counter propagating beam, the probe, has exactly the same frequency in the laboratory frame, and so is absorbed by atoms with the opposite Doppler shift. As the laser frequency is tuned nearer to the resonant frequency the transmitted probe intensity decreases as a greater proportion of the atoms have the necessary Doppler shift to absorb the beam. Thus the detector signal begins to show a Doppler profile. When the beams are tuned to within a natural or pressure broadened linewidth of the resonant frequency, the atoms with no Doppler shift (i.e. zero velocity component along the beam) are saturated by the saturating beam, and the probe, which is resonant with these same atoms, will not be attenuated. Thus the advantage of this technique is that the transmitted intensity of the probe beam then gives the spectral line shape free from Doppler broadening. However only atoms with zero line of sight velocity components contribute and so the high power of a laser is required to give a signal of measurable intensity. Le Gouët [40] measured the broadening of the 3510nm transition in xenon ($5p^5 5d[\frac{7}{2}]_3 \rightarrow 5p^5 6p[\frac{5}{2}]_2$) perturbed by helium at pressures up to about a torr using this technique. Bréchignac et al [16] used saturation spectroscopy to study the 557nm transition of krypton ($4p^6 \rightarrow 4p^5 5s[\frac{3}{2}]_2$) perturbed by xenon at pressures up to 30 mtorr. In their work resonant collisions are important because a comparatively high pressure of krypton is used (70 mtorr).

Two-photon absorption is another Doppler free technique. In this technique the sample is subjected to two counter propagating laser beams tuned to half the resonant frequency under study. In the frame of reference of a moving atom the two beams have different frequencies due to the equal and opposite Doppler shifts. The total energy carried by two counter propagating photons is to first order, see figure 1.5, equal to the transition energy. This is true for atoms with all velocities, and so unlike saturation spectroscopy, all atoms contribute to the signal thus improving the signal-

$$\begin{aligned} \text{TOTAL PHOTON ENERGY} &= h\nu_2 + h\nu_1 \\ \text{(To first order in v/c)} \quad &= h\tfrac{\nu_0}{2}(1-\tfrac{v}{c}) + h\tfrac{\nu_0}{2}(1+\tfrac{v}{c}) \\ &= h\nu_0 \end{aligned}$$

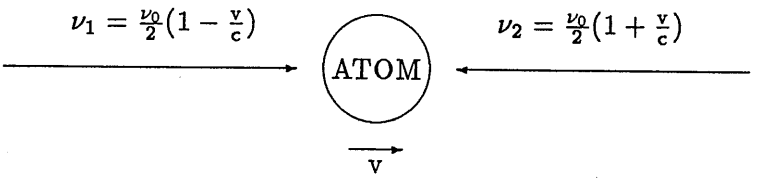

Figure 1.5 Two-photon spectroscopy. Atom has speed v and resonant frequency ν_0.

to-noise ratio for the line profile. Measuring the absorption whilst varying the laser frequency, $(\nu_0/2)$, gives the Doppler-free line shape. Biraben et al [11] used this technique to study the 3S-5S and 3S-4D transitions in sodium perturbed by noble gases at pressures of about a torr. Borstel et al [14] studied the broadening and shift of thallium 6P-nP(n=7,9,10) perturbed by noble gases at pressures of up to 12 torr. A disadvantage of this technique is that the probability of two-photon absorption is very small except when the atom has an intermediate energy level nearly half way between the two levels being studied. The selection rules for two-photon absorption ($\Delta l = 0, \pm 2$) mean that only electric dipole forbidden transitions can be investigated. Two-photon absorption and saturation spectroscopy are therefore complimentary techniques.

1.2.2 Time domain spectroscopy

Coherent optical transients provide the basis for time domain spectroscopy. Reviews are given by Berman et al [8], Shoemaker [83] and Allen and Eberlly [1]. In the frequency domain the effects of natural life time, collisions and the random thermal motion are observed as a broadening of spectral lines. In the time domain these effects result in a decay of the intense light emitted in the forward direction following pulsed excitation. There are three main coherent optical transient effects:

Optical nutation This is an alternating absorption and stimulated emission of radiation that begins when a step wise resonant radiation field is applied to a sample.

Free induction decay This is the decay of the intense light emitted in the forward direction following pulsed excitation and a brief description is given below (i).

The optical echo This is a coherent forward emission at a time when no excitation pulses are applied. The optical echo is introduced below (ii).

(i) Free induction decay

Consider a gas of active atoms or molecules in the absence of perturbers. The gas atoms are all initially in the ground state, and at time $t = 0$ are subjected to a short pulse of laser light resonant with an absorption frequency of the gas. Following the excitation pulse, the light emitted by a single isolated atom will decay exponentially in time with a decay constant $1/\tau_0$, where τ_0 is the lifetime of the upper level. The light emitted laterally by the gaseous sample of n atoms would decay in a similar fashion (modified by self absorption and possible collisional effects in dense media) and would be n times more intense than that for a single atom. For radiation propagating in the forward direction the emitted light is initially coherent and therefore n^2 times more intense than that of a single atom. However the thermal motions of the radiating atoms gives rise to Doppler shifts in emission, so that different atoms radiate at different frequencies. The spread of frequencies causes a rapid dephasing of the radiation, which destroys the initial pulse-induced coherence for forward emission. This rapid decay of the forward emission is called free induction decay. The time scale of the free induction decay is approximately Δ_0^{-1} where Δ_0 is the frequency range excited by the laser pulse. $\Delta_0 = \delta\nu_{\text{Doppler}}$ if the whole Doppler profile is excited. In the microwave region where the free induction decay is not prohibitively rapid fruitful studies of free induction decay itself [17, 36] and

optical nutation [82] have been made using the stark shifting technique. Shoemaker gives a general review [83].

In experiments in the optical regime, such as those discussed in chapter 5, the whole of the Doppler profile is excited by the laser pulses and therefore the free induction decay occurs in a time $\sim (\delta\nu_{\text{Doppler}})^{-1}$, about 1ns following an intense 7ns excitation pulse. Because it occurs immediately after the intense excitation pulse the free induction decay signal is difficult to detect and measure experimentally.

When perturber atoms are present, active atoms suffering elastic collisions with impact parameters smaller than the Weisskopf radius have the phase of their radiation randomised (see section 1.1.2) and so no longer contribute to the coherent forward emission. The decay constant of the free induction decay therefore carries information about collision rates and hence collisional cross sections. However, as described above, this information is not often easy to obtain because the rapid free induction decay occurs immediately after the intense laser excitation pulses. In other words collisional effects are masked by the Doppler effect just as in traditional frequency domain spectroscopy.

(ii) Doppler-free echo spectroscopy

The optical echo technique overcomes the masking effect of the rapid free induction decay by arranging a rephasing of the free induction decay signal at a later time so that the slower decay mechanisms due to collisions or finite lifetimes can be explored. This rephasing of the free induction decay signal is called the optical echo. In a two-excitation-pulse echo experiment, with laser excitation pulses separated by time τ, this rephasing is induced to occur at a time 2τ after the initial laser excitation pulse, see figures 1.6 and 1.7. A theoretical explanation of the formation of two-excitation-pulse optical echoes in a two level system is given in chapter 2 and their application to collision studies is explained in chapter 4. It will be seen, in chapter 4, that the broadening constant can be determined from measurements of the decay, or relaxation, of echo intensity with increasing foreign gas pressure.

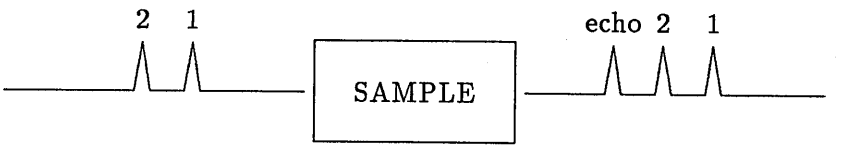

Figure 1.6 Schematic diagram of a two-excitation-pulse echo experiment.

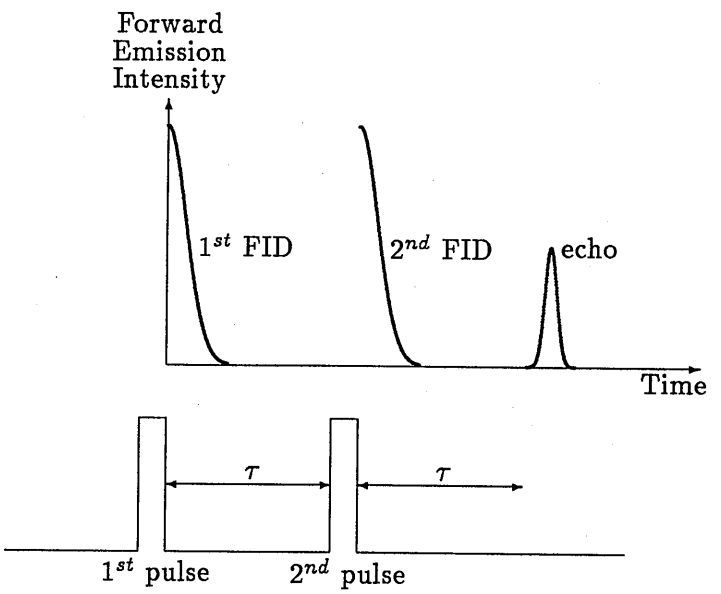

Figure 1.7 The free induction decay (FID) sequences and excitation pulse sequence for a two-excitation-pulse echo.

Such measurements can also give information about aspects of collisions not considered in section 1.1.2.

1.3 Noble Gas Broadening Experiments on the 6S-7P Caesium Lines

Collisional studies of noble gas broadening on the 6S-7P caesium lines have been performed by a number of workers. The results of interest to this work are summarised in table 1.1 and the experimental techniques are discussed below.

Ch'en et al in 1969 [20] studied the broadening by argon of the $6S_{1/2}$-$7P_{3/2}$ caesium line in emission using a 5mA discharge run at 90°C. They varied the pressure of argon between 1 and 60 torr. Their analysis of their profiles from a pressure scanned Fabry-Pérot etalon, corrected for overlap from other line components and other orders, was performed assuming a Voigt profile. Their instrumental and Doppler widths were $0.017cm^{-1}$ and $0.025cm^{-1}$ respectively (0.51 and 0.75GHz).

Rostas and Lemaire in 1971 [78] studied both $6S_{1/2}$-$7P_{1/2}$ and $6S_{1/2}$-$7P_{3/2}$ caesium lines in absorption. They used a number of sealed cells containing a few milligrams of caesium and a range of perturber gas number densities ($1–4\times10^{18}atoms/cm^3$ i.e. 40–160 torr) and worked at about 120°C. The line profiles were obtained using the 13^{th} order of a solar spectrograph which gave a dispersion of 6mm/Å. These profiles were analysed in terms of the Voigt function after deconvoluting the $0.025cm^{-1}$ (0.75GHz) Lorentzian instrument profile.

In 1975 Smith [85] studied the noble gas broadening in absorption using caesium at about 120°C and perturber pressures between 10 and 150 torr. He obtained experimental profiles from the 6^{th} order of a solar spectrograph giving a dispersion of 6.8mm/Å, the instrument profile of which was determined at negligibly small perturber pressures. This instrument profile was convoluted with a range of calculated absorption profiles to obtain the absorption profile corresponding to the experimental ones. Using this analysis

Perturber	Reference	455.5nm ($6S_{1/2}$-$7P_{3/2}$)	459.3nm ($6S_{1/2}$-$7P_{1/2}$)
He	DM	3.24 ± 0.20	3.99 ± 0.22
	RL	3.51 ± 0.20	4.40 ± 0.25
Ar	CLS	2.88 ± 0.36	-
	DM	2.74 ± 0.21	2.97 ± 0.20
	RL	2.95 ± 0.15	3.35 ± 0.25
	S	3.23 ± 0.15	3.44 ± 0.15
Xe	DM	2.62 ± 0.20	2.63 ± 0.17
	KA	2.78 ± 0.51	2.84 ± 0.10
	S	-	3.15 ± 0.21

CLS: Ch'en et al [20]
DM: Durrant and Manners [26]
KA: Kielkopf and Allard [54]
RL: Rostas and Lemaire [78]
S: Smith [85]

Table 1.1 Broadening constants, γ, (equation 1.1) for the 6S-7P transitions in caesium (in units of $10^{-20}\text{cm}^{-1}/\text{cm}^{-3}$) adjusted to 400K assuming a van der Waals interaction (i.e. $T^{0.3}$ temperature dependance).

technique Smith found the line shape to have a small asymmetry.

Kielkopf and Allard in 1980 [54] studied the caesium 6S-7P transitions perturbed by Xenon, with number densities between $10^{18} - 10^{19}\text{atoms/cm}^3$ (40–400 torr), at about 380K (110°C). The experimental profiles were obtained from a 3 metre long high-resolution scanning echelle spectrometer with a premonochromater. Fourier analysis was used to deconvolve the asymmetric line core from the instrumental and Doppler effects.

In 1984 Durrant and Manners [26] used optical echo spectroscopy to study the 6S-7P transitions of caesium perturbed by noble gases at pressures below 0.5 torr. They worked with caesium vapour at about 50°C. Since this is a Doppler free technique deconvolution was not required. However since the measurements were all performed with the same interpulse time, τ=32.5ns, the calculated broadening constant could not be considered to be totally due to phase interrupting collisional effects (see chapter 4).

Chapter 2

A Theoretical Treatment Of Two-excitation-pulse Echoes In Non-degenerate Two Level Systems

A simple theory describing the formation of the two-excitation-pulse echo in a two state system using Schrödinger's equation is the main subject of this chapter. Firstly in section 2.1 a brief review of optical (and infrared) echo phenomena is given.

2.1 Echo Phenomena

The first analysis of echoes on a two level system was given by Hahn [42] in 1950 for nuclear spin echoes generated by a sequence of radio frequency pulses. The development of the laser gave the experimentalists a source of intense optical frequency pulses and in 1964 an optical echo was observed in ruby by Kurnit et al [56]. In 1968 Scully et al [81] predicted the existence of an optical echo in a gaseous medium. This was an important step because for some time it had been thought that the thermal motions in a gas would prevent the rephasing necessary for the formation of an echo. In the same year Patel and Slusher [77] used a pulsed CO_2 laser (10.6μm) to produce echoes in a molecular gas (SF_6) and Bölger and Diels [13] reported echoes in caesium vapour on the $6S_{1/2}$-$6P_{3/2}$ transition at 852nm using a temperature tuned diode laser. Echoes on the visible 6S-7P caesium transition were not

reported until 1976 [4].

A large amount of echo work was performed in the early 1970's using a stark shifting technique [83] where vibrational rotational transitions in molecular gases were pulsed into resonance with a fixed frequency microwave laser by application of a pulsed electric field. With the development of the tunable dye laser the number of systems that were suitable for optical echo study greatly increased and encompassed transitions between electronic energy levels of atomic and molecular gases. Most echo work is concerned with measuring collision rates and cross sections associated with optical coherence and populations. Reviews of echo techniques for use in collisional studies are given by Mossberg et al [73, 74]. Echoes can be generated using three or more pulses acting on one or two optical transitions. Examples of these echo phenomena include tri-level echoes [68, 72] and Raman echoes [58], which are used in collisional studies of electric dipole forbidden transitions. Two-excitation-pulse echoes, tri-level echoes and Raman echoes have been used mainly to study the collision rates for optical coherence. Stimulated echoes, using three excitation pulses, have been used to study state populations following collisions, see for example [49, 53]. Rydberg atoms have also been investigated by echo techniques [31]. Mossberg et al [69] give a general density matrix treatment of these different echo phenomena. Russian workers have concentrated on theoretical investigations of optical echo phenomena and in particular on the effects of differing excitation pulse shapes and polarisations, see for example [28, 29, 30, 94]. A treatment of two-excitation-pulse echoes and other coherent transients in a two state system using optical Bloch Equations is given by Shoemaker [83] and by Allen and Eberly [1].

The effects of level degeneracy and the polarisation properties of echoes [57] are discussed in a simple manner in chapter 3, thus explaining the mechanism behind the echo polarisation rotation discrimination technique used for the experimental work described in this thesis.

2.2 Principle Assumptions and Method

The treatment given below is based on a non-degenerate two level system and is used firstly, in section 2.3, to describe the response of a vapour subjected to a single resonant light pulse—the free induction decay. The model is then used, in section 2.4, to describe the formation of an echo when the vapour is subjected to a sequence of two collinear resonant light pulses. Finally in section 2.5 the formation of an echo using non-collinear excitation pulses is discussed.

The main assumptions of this theoretical analysis are:

1 The active atoms can be described by two state systems.

2 The electric dipole approximation is valid.

3 All atoms are excited at the same time by the excitation radiation field. This assumption is not strictly necessary and is not made in some other works [69, 83]. It amounts to neglecting propagation times through the sample.

4 The durations of the excitation pulses are negligible in comparison with all other times of interest, such as the time between excitation pulses.

5 Inhomogeneous broadening can be neglected during the action of the pulses. That is, all atoms are assumed to be in resonance with the excitation radiation. This assumption also allows for the atom's motion to be neglected during the excitation pulses.

6 Spontaneous and collisional decay can be neglected (These are considered in chapter 4).

7 The vapour is optically thin.

8 The analysis can be performed using semi-classical theory in which the radiation field is a classical Maxwellian wave. In this approach the expectation value of the atomic dipole moment is regarded as a classical radiating dipole.

9 Non-resonance terms in the interaction can be neglected. This is called the rotating wave approximation.

The calculations involved in giving a description of both free induction decay and echo formation follow the same steps. For this reason sections 2.3 and 2.4 have identical subdivisions. The analyses in these two sections follow four steps:

1. Calculating the state of an atom in the sample following the excitation pulse sequence
2. Evaluating the expectation value of the atomic dipole moment of the atom at position $\mathbf{R}$ and time t
3. Averaging the atomic dipole moments, at $\mathbf{R}$ and t, over the thermal velocity distribution and then determining the average dipole moment per unit volume or macroscopic polarisation
4. Determining the optical forward emission intensity from the macroscopic polarisation

2.3 Response Following a Single Resonant Pulse—Free Induction Decay

2.3.1 Description of the state of the atom

Consider the two state system with upper and lower levels represented by kets $|u\rangle$ and $|l\rangle$ coupled by an electric dipole transition as shown in figure 2.1. The state of the system can be described at any time t by the superposition state

$$|t\rangle = a_l(t)|l\rangle + a_u(t)|u\rangle e^{-i\omega t} \tag{2.1}$$

$$|a_l(t)|^2 + |a_u(t)|^2 = 1$$

where $a_l(t)$ and $a_u(t)$ are the interaction representation amplitudes and $\omega = (\mathrm{E}_u - \mathrm{E}_l)/\hbar$. Note from assumption 5 that the inhomogeneous broadening is neglected during an excitation pulse ($t_p \ll 1/\delta\nu_{\mathrm{Doppler}}$ where t_p is

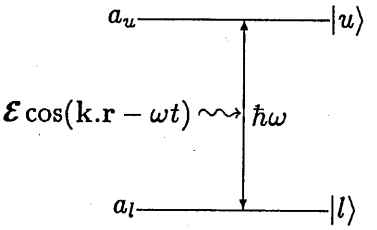

Figure 2.1 The two state system.

the duration of the pulse). Under this assumption all atoms can be assumed to be resonant with the pulse. The atom interacts with a resonant light pulse described by

$$\mathrm{E}(\mathbf{r},t) = \boldsymbol{\mathcal{E}}(t)\cos(\mathrm{k.r}-\omega t) \qquad (0 < t < t_p)$$

The pulse is assumed to arrive at time $t = 0$ for all atoms in the sample (assumption 3). The electric field envelope, $\boldsymbol{\mathcal{E}}(t)$, varies slowly over an optical period. k is the wavevector of the radiation and r is the position of the atom at the time the pulse arrives. From assumption 5 the atom's position remains constant for the duration of the pulse.

Schrödinger's equation for the atom can be written as

$$(\hat{\mathcal{H}}_0 + \hat{\mathcal{H}}_{\mathrm{int}})|t\rangle = -\frac{\hbar}{i}\frac{d}{dt}|t\rangle \tag{2.2}$$

where $\hat{\mathcal{H}}_0$ is the atomic Hamiltonian with eigenvalues zero and $\hbar\omega$ and corresponding eigenvectors $|l\rangle$ and $|u\rangle$ respectively. The interaction Hamiltonian for an atom at position r in the dipole approximation is

$$\hat{\mathcal{H}}_{\mathrm{int}} = -\boldsymbol{\mathcal{E}}(t).\hat{\mathbf{d}}\cos(\mathrm{k.r}-\omega t) \tag{2.3}$$

$\hat{\mathbf{d}}$ is the electric dipole operator with matrix elements

$$\langle u|\hat{\mathbf{d}}|u\rangle = \langle l|\hat{\mathbf{d}}|l\rangle = 0 \text{ and } \langle u|\hat{\mathbf{d}}|l\rangle = \langle l|\hat{\mathbf{d}}|u\rangle = \mathbf{D} \tag{2.4}$$

D is real for a suitable choice of kets $|u\rangle$ and $|l\rangle$. Substituting equations 2.1 and 2.3 into equation 2.2 and using the orthogonality of $|u\rangle$ and $|l\rangle$ and equations 2.4, gives two coupled differential equations

$$\left.\begin{aligned} \dot{a}_u &= i\frac{\boldsymbol{\mathcal{E}}(t).\mathbf{D}}{2\hbar}(e^{i\mathrm{k.r}} + e^{-i\mathrm{k.r}}e^{i2\omega t})a_l \\ \dot{a}_l &= i\frac{\boldsymbol{\mathcal{E}}(t).\mathbf{D}}{2\hbar}(e^{i\mathrm{k.r}}e^{-2i\omega t} + e^{-i\mathrm{k.r}})a_u \end{aligned}\right\}$$

The term containing $e^{i2\omega t}$ varies rapidly, at twice an optical frequency, and is neglected in the so-called 'rotating wave approximation' (RWA) assumption 9, giving

$$\left.\begin{aligned} \dot{a}_u &= i\frac{\boldsymbol{\mathcal{E}}(t).\mathbf{D}}{2\hbar}e^{i\mathbf{k}.\mathbf{r}}a_l \\ \dot{a}_l &= i\frac{\boldsymbol{\mathcal{E}}(t).\mathbf{D}}{2\hbar}e^{-i\mathbf{k}.\mathbf{r}}a_u \end{aligned}\right\}$$

The general solution to these coupled differential equations is

$$\left.\begin{aligned} a_u(t) &= A_u\cos(\vartheta(t)/2) + ie^{i\mathbf{k}.\mathbf{r}}A_l\sin(\vartheta(t)/2) \\ a_l(t) &= A_l\cos(\vartheta(t)/2) + ie^{-i\mathbf{k}.\mathbf{r}}A_u\sin(\vartheta(t)/2) \end{aligned}\right\} \qquad (2.5)$$

where the initial amplitudes are given by

$$a_u(0) = A_u \quad \text{and} \quad a_l(0) = A_l$$

with $|A_u|^2 + |A_l|^2 = 1$ for normalisation. Also

$$\vartheta(t) = \int_0^t \frac{\boldsymbol{\mathcal{E}}(s).\mathbf{D}}{\hbar}ds \qquad 0 \le t \le t_p$$

where, it is recalled, that t_p is the pulse duration and the pulse has been assumed to arrive at time $t = 0$. Since the interaction representation amplitudes do not evolve after the pulses, for times $t \ge t_p$ the pulse area, θ, defined by

$$\theta = \vartheta(t_p)$$

can be substituted into equations 2.5 to give, for $t > t_p$,

$$\left.\begin{aligned} a_u(t) &= A_u\cos(\theta/2) + ie^{i\mathbf{k}.\mathbf{r}}A_l\sin(\theta/2) \\ a_l(t) &= A_l\cos(\theta/2) + ie^{-i\mathbf{k}.\mathbf{r}}A_u\sin(\theta/2) \end{aligned}\right\} \qquad (2.6)$$

These equations with equation 2.1 then describe the state of the atom following a single resonant pulse. An atom initially in the lower state (i.e. $A_l = 1$ and $A_u = 0$) is, at time t after the pulse, in the state

$$|t\rangle = \cos(\theta/2)|l\rangle + ie^{i\mathbf{k}.\mathbf{r}}\sin(\theta/2)|u\rangle e^{-i\omega t} \qquad (t > t_p) \qquad (2.7)$$

2.3.2 Evaluation of the expectation value for the atomic dipole moment

For the atom described by equation 2.7, the expectation value for the atomic dipole moment is given by

$$\langle t|\hat{\mathbf{d}}|t\rangle = i\frac{1}{2}\sin\theta e^{i\mathbf{k}.\mathbf{r}}e^{-i\omega t}\mathbf{D} + \text{c.c.} \tag{2.8}$$

where c.c. means complex conjugate, the expectation value $\langle t|\hat{\mathbf{d}}|t\rangle$ being, of course, real.

2.3.3 The average atomic dipole moment and the macroscopic polarisation

The macroscopic polarisation, $\mathbf{P}$, at position $\mathbf{R}$ in the sample at time t after the pulse is given by the sum of the atomic dipole moments in the unit volume at $\mathbf{R}$ at time t, or equivalently in this analysis by the average of the atomic dipole moments multiplied by the number of atoms per unit volume, n. Equation 2.8 therefore leads to

$$\mathbf{P}(\mathbf{R},t) = n\langle i\frac{1}{2}\sin\theta e^{i\mathbf{k}.\mathbf{r}}e^{-i\omega t}\mathbf{D}\rangle_{\mathbf{v}} + \text{c.c.} \tag{2.9}$$

where $\mathbf{r}$ is the position of the atom during excitation and t is the time since the excitation. The angled brackets indicate an average over the velocity $\mathbf{v}$ of all atoms at $\mathbf{R}$ at time t. To perform this average it is necessary to relate the position $\mathbf{R}$ in the sample at time t to the position $\mathbf{r}$ of the atoms in question at the time $t = 0$ of the excitation pulse. From figure 2.2 it can be seen that

$$\mathbf{r} = \mathbf{R} - \mathbf{v}t$$

Substituting this equation into equation 2.9 and taking terms independent of $\mathbf{v}$ outside the average gives

$$\mathbf{P}(\mathbf{R},t) = in\frac{1}{2}\sin\theta\ \mathbf{D}e^{-i\omega t}e^{i\mathbf{k}.\mathbf{R}}\langle e^{-i\mathbf{k}ut}\rangle_{\mathbf{v}} + \text{c.c.} \tag{2.10}$$

where k.v has been written as ku, k being the magnitude of the wave vector and u the component of atomic velocity along this wave vector. The average

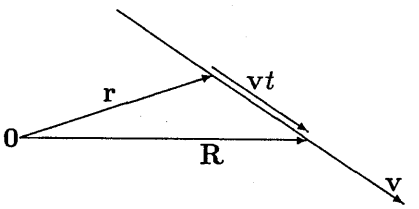

Figure 2.2 Vector diagram to show relationship between **r**, **R** and **v**.

in equation 2.10 can be calculated since u has a Gaussian probability distribution (derived from the Maxwell-Boltzmann distribution) with half width at half maximum $u_0\sqrt{\log_e 2}$, where u_0 is equal to the root mean square value of the thermal velocities. This average in equation 2.10 is given by

$$\langle e^{-iku t}\rangle_v = \int_{-\infty}^{\infty} e^{-iku t}\frac{\exp(-u^2/u_0^2)}{u_0\sqrt{\pi}}du = e^{-k^2u_0^2t^2/4} \qquad (2.11)$$

Substituting this average into equation 2.10 gives

$$\begin{aligned} P(R,t) = \mathcal{P} + \text{c.c.} &= in\frac{1}{2}\sin\theta\, D e^{-i\omega t}e^{ik.R}e^{-k^2u_0^2t^2/4} + \text{c.c.} \\ &= n\frac{1}{2}\sin\theta\, D e^{-k^2u_0^2t^2/4} 2\sin(k.R - \omega t) \end{aligned} \qquad (2.12)$$

This describes the free induction decay of the polarisation following the pulse at $t = 0$. It may be of interest to the reader to note that equation 2.11 is essentially a Fourier transform from the frequency domain to the time domain and that $ku_0 = \delta\nu_{\text{Doppler}}$ is the half width at half maximum of the Doppler broadened line.

2.3.4 Calculation of the forward emission intensity

The electric field radiated by a spatial distribution of polarisation is found by solving Maxwell's inhomogeneous wave equation. For this application

where the sample is optically thin [83] the field radiated is given by

$$\mathrm{E}(L,t) = i\frac{\mathrm{k}L}{2\varepsilon_0}\boldsymbol{\mathcal{P}}(L,t) + \mathrm{c.c.}$$

where L is the length of the sample and $\mathrm{k} = |\mathrm{k}|$. Substituting equation 2.12 into this equation gives

$$\mathrm{E}(\mathbf{R},t) = -\frac{\mathrm{k}L}{2\varepsilon_0}n\frac{1}{2}\sin\theta\ \mathrm{D}e^{-\mathrm{k}^2\mathrm{u}_0^2t^2/4}2\cos(\mathrm{k}.\mathbf{R} - \omega t)$$

The forward coherent emission intensity, I, is proportional to the square of the modulus of the radiated field averaged over an optical cycle (no detector can respond at optical frequencies). Using the above equation, gives

$$\mathrm{I}(t) \propto \frac{\mathrm{k}^2}{{\varepsilon_0}^2}n^2L^2\sin^2\theta\ |\ \mathrm{D}|^2e^{-\mathrm{k}^2\mathrm{u}_0^2t^2/2} \tag{2.13}$$

It can be seen that the initial value of the intensity is very large being proportional to the square of the number of excited atoms per unit cross section of the sample, $(Ln)^2$, but falls off very rapidly following the excitation, $t > 0$. The intensity will decay to $1/e$ of its initial value in a time given by $\sqrt{2}/\mathrm{ku}_0$. This is typically about $\frac{1}{10^7 10^2}\mathrm{s} = 10^{-9}\mathrm{s}$ =1ns, see figure 2.3. This free induction decay is due to Doppler dephasing and corresponds to Doppler broadening in the frequency domain. It should be noted that the free induction decay is a decay of coherence and is in principle reversible since the atomic dipole moments continue to oscillate, assumption 6. Optical echoes result from such a reversal of this dephasing.

2.4 Response Following Two Collinear Resonant Pulses—Echo Formation

In this section the response of the system of figure 2.1 following two short pulses separated by a time interval, τ (see figure 1.7), is considered. The pulse duration, t_p, is assumed small in comparison with τ and also in comparison with the free induction decay time, $(\mathrm{ku}_0)^{-1}$, (assumptions 4 and 5).

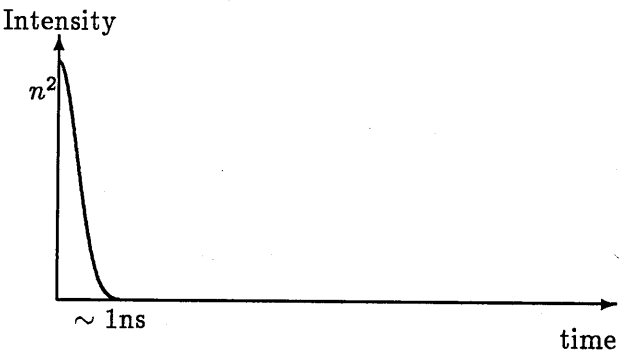

Figure 2.3 Free induction decay.

2.4.1 Description of the state of the atom

The first pulse interacts with the atom in the ground state at time $t = 0$. The initial conditions are thus

$$\left.\begin{aligned} a_u(t) &= 0 \\ a_l(t) &= 1 \end{aligned}\right\} \quad t < 0$$

After the first pulse, the amplitudes can be calculated using equation 2.6 with $A_u = 0$ and $A_l = 1$ to give

$$\left.\begin{aligned} a_u(t) &= ie^{i\mathbf{k}.\mathbf{r}(0)}\sin(\theta_1/2) \\ a_l(t) &= \cos(\theta_1/2) \end{aligned}\right\} \quad 0 < t < \tau \tag{2.14}$$

where at time $t = 0$ the atom is considered to be at a position given by $\mathbf{r}(0)$ and the first pulse to have an area θ_1 and wavevector $\mathbf{k}$. The second pulse, also with wavevector $\mathbf{k}$ but with pulse area θ_2, encounters the atom at a time $t = \tau$ and a position $\mathbf{r}(\tau)$. Using equation 2.14 gives the initial conditions A_u and A_l for the second pulse, at time $t = \tau$, as

$$\left.\begin{aligned} A_u &\equiv a_u(\tau) = ie^{i\mathbf{k}.\mathbf{r}(0)}\sin(\theta_1/2) \\ A_l &\equiv a_l(\tau) = \cos(\theta_1/2) \end{aligned}\right\} \quad t = \tau$$

Equations 2.6 then give the amplitudes following the second pulse as

$$\left.\begin{aligned} a_u(t) = {} & ie^{i\mathbf{k}.\mathbf{r}(0)} \sin(\theta_1/2)\cos(\theta_2/2) \\ & + ie^{i\mathbf{k}.\mathbf{r}(\tau)} \cos(\theta_1/2)\sin(\theta_2/2) \\ a_l(t) = {} & \cos(\theta_1/2)\cos(\theta_2/2) \\ & + ie^{-i\mathbf{k}.\mathbf{r}(\tau)} ie^{i\mathbf{k}.\mathbf{r}(0)} \sin(\theta_1/2)\sin(\theta_2/2) \end{aligned}\right\} \quad t > \tau \qquad (2.15)$$

Substituting these equations into equation 2.1 gives the state of the atom, $|t\rangle$, for times $t > \tau$.

2.4.2 Evaluation of the expectation value for the atomic dipole moment

The expectation value of the dipole moment, $\langle t|\hat{\mathbf{d}}|t\rangle$, can be found from the state of the atom by using equations 2.4. For any time $t > \tau$ the expectation value of the dipole moment (from equations 2.1, 2.4 and 2.15) will be given by

$$\begin{aligned} \langle t|\hat{\mathbf{d}}|t\rangle = i\mathbf{D}\{ & \sin\frac{\theta_1}{2}\cos\frac{\theta_1}{2}\cos^2\frac{\theta_2}{2}\, e^{i\mathbf{k}.\mathbf{r}(0)} \\ & - \sin\frac{\theta_2}{2}\cos\frac{\theta_2}{2}(\sin^2\frac{\theta_1}{2} - \cos^2\frac{\theta_1}{2})\, e^{i\mathbf{k}.\mathbf{r}(\tau)} \\ & - \sin\frac{\theta_1}{2}\cos\frac{\theta_1}{2}\sin^2\frac{\theta_2}{2}\, e^{i\mathbf{k}.(2\mathbf{r}(\tau)-\mathbf{r}(0))}\}e^{-i\omega t} + \text{c.c.} \\ = i\mathbf{D}\{ & \frac{1}{2}\sin\theta_1\cos^2\frac{\theta_2}{2}\, e^{i\mathbf{k}.\mathbf{r}(0)} \\ & + \frac{1}{2}\sin\theta_2\ \cos\theta_2\, e^{i\mathbf{k}.\mathbf{r}(\tau)} \\ & - \frac{1}{2}\sin\theta_1\ \sin^2\frac{\theta_2}{2}\, e^{i\mathbf{k}.(2\mathbf{r}(\tau)-\mathbf{r}(0))}\}e^{-i\omega t} + \text{c.c.} \end{aligned} \qquad (2.16)$$

2.4.3 The average atomic dipole moment and the macroscopic polarisation

The macroscopic polarisation, $\mathbf{P}(\mathbf{R}, t)$, following two pulses is given by the velocity average of the above dipole moment for all atoms at position $\mathbf{R}$ and at time t, multiplied by the mean number density, n, of atoms. The averaging is similar to that done in section 2.3.3. Using figure 2.4, the positions of the

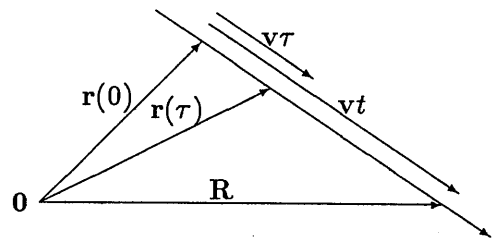

Figure 2.4 Vector diagram relating atomic positions with velocity.

atom during the excitations, $\mathbf{r}(0)$ and $\mathbf{r}(\tau)$, can be expressed in terms of $\mathbf{R}$, t and the constant atomic velocity, $\mathbf{v}$, as

$$\left.\begin{aligned} \mathbf{r}(0) &= \mathbf{R} - \mathbf{v}t \\ \mathbf{r}(\tau) &= \mathbf{R} - \mathbf{v}(t-\tau) \end{aligned}\right\} \tag{2.17}$$

Using these relationships and taking terms independent of $\mathbf{v}$ outside the average, the macroscopic polarisation for $t > \tau$ is seen to be

$$\begin{aligned} \mathbf{P}(\mathbf{R},t) = i\tfrac{n}{2}\ \mathbf{D}\{&\sin\theta_1\ \cos^2\frac{\theta_2}{2} e^{i\mathbf{k}.\mathbf{R}} \langle e^{-i\mathbf{k}.\mathbf{v}t}\rangle_{\mathbf{v}} \\ &+ \sin\theta_2\ \cos\theta_1\ e^{i\mathbf{k}.\mathbf{R}} \langle e^{-i\mathbf{k}.\mathbf{v}(t-\tau)}\rangle_{\mathbf{v}} \\ &- \sin\theta_1\ \sin^2\frac{\theta_2}{2} e^{i\mathbf{k}.\mathbf{R}} \langle e^{-i\mathbf{k}.\mathbf{v}(t-2\tau)}\rangle_{\mathbf{v}}\} e^{-i\omega t} \\ &+ \text{c.c.} \qquad (t > \tau) \end{aligned} \tag{2.18}$$

Performing integrations similar to those done in section 2.3.3, the three averages in equation 2.18 are seen to be respectively

$$e^{-\mathbf{k}^2\mathbf{u}_0^2 t^2/4}, e^{-\mathbf{k}^2\mathbf{u}_0^2(t-\tau)^2/4} \text{ and } e^{-\mathbf{k}^2\mathbf{u}_0^2(t-2\tau)^2/4} \quad (t > \tau)$$

Each of these Gaussian time functions has the form expected for a free induction decay signal, the first and second at $t = 0$ and $t = \tau$ respectively, the times of the excitation pulses, and the third is centred on $t = 2\tau$ a time when no external excitation is applied. This corresponds to the echo.

2.4.4 Calculation of the forward emission intensity

At times near $t = 2\tau$ the first two Gaussian time functions above are negligibly small so that only the echo term in equation 2.18 need be retained giving the macroscopic polarisation near the echo time as

$$\begin{aligned} \mathbf{P}_e(\mathbf{R},t) &= -i\frac{n}{2}\mathbf{D}\sin\theta_1 \sin^2\frac{\theta_2}{2}e^{i\mathbf{k}.\mathbf{R}}e^{-i\omega t}e^{-\mathbf{k}^2\mathbf{u}_0^2(t-2\tau)^2/4} + \text{c.c.} \\ &= n\mathbf{D}\sin\theta_1\sin^2\frac{\theta_2}{2}e^{-\mathbf{k}^2\mathbf{u}_0^2(t-2\tau)^2/4}\sin(\mathbf{k}.\mathbf{R}-\omega t) \end{aligned} \tag{2.19}$$

The electric field radiated by an optically thin sample with this polarisation can be found as in section 2.3.4 and is given by

$$\mathbf{E}_e(\mathbf{R},t) = \frac{\mathrm{k}L}{2\varepsilon_0}n\mathbf{D}\sin\theta_1\sin^2\frac{\theta_2}{2}e^{-\mathbf{k}^2\mathbf{u}_0^2(t-2\tau)^2/4}\cos(\mathbf{k}.\mathbf{R}-\omega t)$$

This is a plane wave travelling in the same direction with the same wavevector, k, as the two excitation pulses. The forward emission intensity, the echo intensity, is proportional to the square of the modulus of the radiated field averaged over an optical cycle and is therefore given by

$$\mathrm{I}_e(t) \propto \frac{\mathrm{k}^2}{{\varepsilon_0}^2}n^2L^2\sin^2\theta_1\sin^4\frac{\theta_2}{2}\ |\mathbf{D}|^2e^{-\mathbf{k}^2\mathbf{u}_0^2(t-2\tau)^2/2} \tag{2.20}$$

Again this is proportional to the square of the number of excited atoms per unit cross section of the sample, $(nL)^2$. It rises and decays away in a typical time of 1ns (ie $\frac{\sqrt{2}}{\mathrm{ku}_0}$). It can also be seen that the echo pulse intensity is maximised for a pulse sequence where the first pulse has a pulse area of $\pi/2$ and the second of π.

2.5 Echo Formation Following Non-collinear Excitation Pulses

An echo may still be formed, but with reduced intensity, even if the excitation pulses are not exactly collinear [2, 81]. This is important for experiment work because the excitation pulses, which preceed the echo, can then be blocked using aperatures whilst the echo, which follows a different

path to both excitation pulses, can be allowed to pass. Such spatial filtering has been used to help protect the detector from the very intense excitation pulses [6]. The reduction in intensity of such an echo is now calculated.

In experiments both excitation pulses are usually from the same laser therefore their wave vectors will have the same magnitude, k, but directions assumed to be separated by angle ϕ. Taking the wave vectors of the first and second pulses as k_1 and k_2 respectively, with $\mid \mathrm{k}_1 \mid = \mid \mathrm{k}_2 \mid = \mathrm{k}$, and working through the analysis as in section 2.4 as far as equation 2.18 gives, omitting the two free induction decay terms which are negligibly small for $t > \tau$, the following expression for the echo polarisation of the medium

$$\mathbf{P}_e(\mathbf{R},t) = \mathbf{C}e^{i\{(2\mathrm{k}_2-\mathrm{k}_1).\mathrm{R}-\omega t\}}\langle e^{-i\{2\mathrm{k}_2.\mathrm{v}(t-\tau)-\mathrm{k}_1.\mathrm{v}t\}}\rangle_{\mathrm{v}} + \text{c.c.} \quad (t > \tau) \quad (2.21)$$

where $\mathbf{C} = -i\frac{n}{2}\mathbf{D}\sin\theta_1 \sin^2(\theta_2/2)$. The first exponential describes a plane wave of polarisation with wavevector $\mathrm{k}_e = 2\mathrm{k}_2 - \mathrm{k}_1$ and frequency ω. In section 2.5.2 the phase matching condition will be obtained from this. Firstly however, in section 2.5.1 the velocity average will be examined and from it a modified echo time will be obtained. Also from the velocity average the reduction in the macroscopic polarisation at this echo time is calculated.

2.5.1 Dependance of the echo macroscopic polarisation on excitation pulse angular separation

The atomic velocity, which will be different for different atoms, can be resolved into components, v_e and v_n, parallel and perpendicular to the direction defined by the propagation vector $\mathrm{k}_e = 2\mathrm{k}_2 - \mathrm{k}_1$. Take the unit vector in the echo direction as $\tilde{\mathrm{e}}$ and the unit vector normal to this as $\tilde{\mathrm{n}}$, and define $\mathrm{k}_e = \mathrm{k}_e\tilde{\mathrm{e}}$ and ψ as the angle between k_e and k_1 (ψ and ϕ are, of course, related). Figure 2.5 shows the relationship between these quantities for a particular atomic velocity, v. The velocity average in equation 2.21 is then

$$\begin{aligned}\langle e^{-i\{2\mathrm{k}_2.\mathrm{v}(t-\tau)-\mathrm{k}_1.\mathrm{v}t\}}\rangle_{\mathrm{v}} &= \langle e^{-i(\mathrm{k}_e(t-\tau)-\mathrm{k}_1\tau).(\mathrm{v}_e\tilde{\mathrm{e}}+\mathrm{v}_n\tilde{\mathrm{n}})}\rangle_{\mathrm{v}} \\ &= \langle e^{-i\{\mathrm{k}_e(t-\tau)\mathrm{v}_e-\mathrm{k}\tau\mathrm{v}_e\cos\psi-\mathrm{k}\tau\mathrm{v}_n\sin\psi\}}\rangle_{\mathrm{v}}\end{aligned}$$

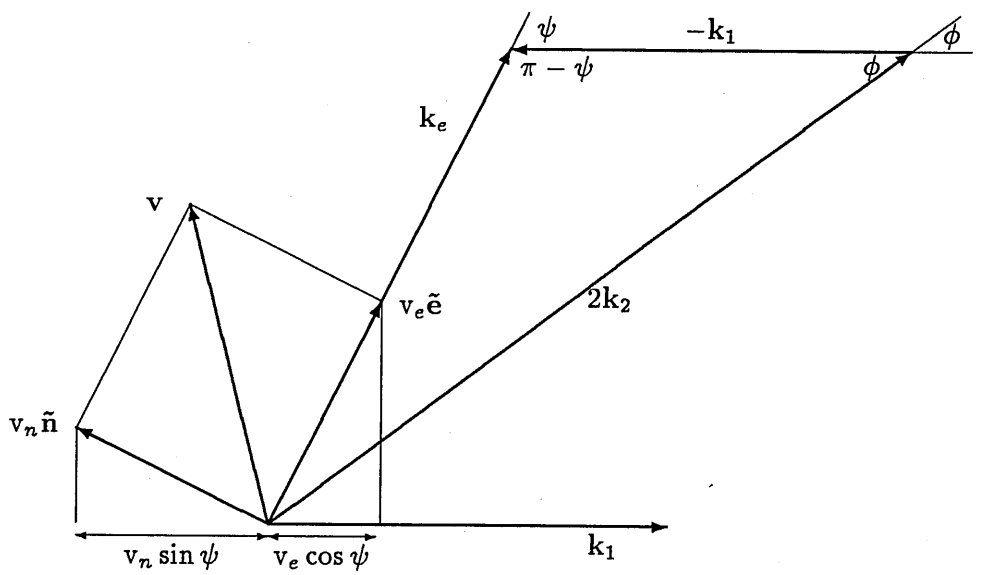

Figure 2.5 The wave vector triangle drawn with a particular atomic velocity.

Factoring terms in v_e and v_n gives

$$\langle e^{-i\{2k_2.v(t-\tau)-k_1.vt\}}\rangle_v = \langle e^{-i\{v_e(k_e(t-\tau)-k\tau\cos\psi)-v_nk\tau\sin\psi\}}\rangle_v$$

Velocity components in any two perpendicular directions will be statistically independent and each will have a Gaussian probability distribution over the ensemble as in equation 2.11. Carrying out the velocity average by integrating over both v_e and v_n gives

$$\langle e^{-i\{2k_2.v(t-\tau)-k_1.vt\}}\rangle_v = \int_{-\infty}^{\infty}\int_{-\infty}^{\infty} e^{-iv_e\{k_e(t-\tau)-k\tau\cos\psi\}}e^{iv_nk\tau\sin\psi} \times e^{-(v_e/u_o)^2}e^{-(v_n/u_o)^2}dv_edv_n$$

$$= e^{-u_0^2k_e^2(t-(1+\frac{k\cos\psi}{k_e})\tau)^2/4}e^{-u_0^2k^2\tau^2(\sin^2\psi)/4} \quad (2.22)$$

The first exponential factor describes rephasing at time

$$t_e = (1+\frac{k\cos\psi}{k_e})\tau \quad (2.23)$$

This is the new echo time. Note that when the pulses are collinear $k_e = k_1 = k_2$, and $\psi = 0$, so $t_e = 2\tau$ and the results of section 2.4 are recovered.

The echo intensity is proportional to the square of the modulus of the macroscopic polarisation and hence is proportional to the square of the average in equation 2.22. The reduction of echo intensity with increasing ψ is therefore given by the factor

$$e^{-u_0^2k^2\tau^2(\sin^2\psi)/2}$$

Typical values of the parameters for caesium (6S-7P) are $u_0 \sim 200$m/s, $k \sim 1.4\times10^7$m^{-1} and $\tau \sim 100$ns. For the echo intensity to be within $1/e$ of the intensity at ψ=0 requires $(u_0^2k^2\tau^2\sin^2\psi)/2 < 1$. This requires $\sin\psi$ to be less than about 0.005 and ϕ is approximately half of ψ, see figure 2.5. Therefore the echo experiments need to be performed with k_1 and k_2 separated by less than about 2mrad, especially at larger pulse separations, τ, since the intensity is proportional to $e^{-\tau^2}$.

The new echo time (equation 2.23) is now investigated. Applying the cosine rule to the wavevector triangle in figure 2.5 gives

$$\begin{aligned} \mathrm{k}_e^2 &= (\mathrm{k})^2 + (2\mathrm{k})^2 - 2(\mathrm{k})(2\mathrm{k})\cos\phi \\ \Rightarrow \mathrm{k}_e^2 &= 5\mathrm{k}^2 - 4\mathrm{k}^2\cos\phi \end{aligned} \tag{2.24}$$

Applying the sine rule gives

$$\begin{aligned} \frac{\sin\phi}{\mathrm{k}_e} &= \frac{\sin(\pi-\psi)}{2\mathrm{k}} \\ \Rightarrow \frac{\sin\phi}{\mathrm{k}_e} &= \frac{\sin\psi}{2\mathrm{k}} \end{aligned}$$

Eliminating k_e, which is of course positive, between the above sine and cosine rule equations gives

$$\sin\psi = \frac{2\sin\phi}{\sqrt{5-4\cos\phi}}$$

Since ϕ is small, Taylor series approximations can be applied. This gives to fourth order

$$\begin{aligned} \sin\psi &= \frac{2(\phi-\phi^3/6)}{\sqrt{5-4(1-\phi^2/2+\phi^4/24)}} \\ &= 2\phi - \frac{7}{3}\phi^3 \end{aligned} \tag{2.25}$$

ψ can also be expanded as a fourth order Taylor series in ϕ, the coefficients of which will be obtained below,

$$\psi = W\phi + X\phi^2 + Y\phi^3 + Z\phi^4$$

Also to fourth order

$$\begin{aligned} \sin\psi &= \psi - \psi^3/6 \\ \Rightarrow \sin\psi &= W\phi + X\phi^2 + Y\phi^3 + Z\phi^4 - \frac{1}{6}(W^3\phi^3 + 3W^2X\phi^4) \\ &= W\phi + X\phi^2 + (Y - W^3/6)\phi^3 + (Z - W^2X/2)\phi^4 \end{aligned}$$

Equating powers of ϕ between this equation for $\sin\psi$ and the right hand side of equation 2.25 gives

$$W = 2,\ X = 0,\ Y = -1 \text{ and } Z = 0$$

Therefore, to fourth order in ϕ,

$$\psi = 2\phi - \phi^3$$

Using this equation and equation 2.24 the echo time (equation 2.23) can be found to fourth order in ϕ.

$$\begin{aligned} t_e &= (1 + \frac{\mathrm{k}\cos\psi}{\mathrm{k}_e})\tau \\ &= \{1 + (1 - \psi^2/2 + \psi^4/24)(1 - \phi^2 + \frac{19}{12}\phi^4))\}\tau \\ &= (2 - 3\phi^2 + \frac{17}{4}\phi^4)\tau \end{aligned}$$

That is the echo time is not shifted to first order in ϕ.

2.5.2 Phase matching

The optical echo is radiated at the same frequency, ω, as the excitation pulses and so must propagate with a wavenumber of the same magnitude, k. However as can be seen from equation 2.21 the echo macroscopic polarisation has a wavenumber $\mathrm{k}_e = |2\mathrm{k}_2 - \mathrm{k}_1|$. The difference between the wavenumbers k_e and k can be obtained from equation 2.24, which is

$$\mathrm{k}_e^2 = 5\mathrm{k}^2 - 4\mathrm{k}^2\cos\phi$$

Applying small angle approximations to fourth order and knowing k_e to be positive gives

$$\begin{aligned} \mathrm{k}_e &= \mathrm{k}\sqrt{5 - 4(1 - \phi^2/2 + \phi^4/24)} \\ &= \mathrm{k}(1 + \phi^2 - \frac{7}{12}\phi^4) \end{aligned}$$

The difference between k_e and k is therefore

$$\mathrm{k}_e - \mathrm{k} = \mathrm{k}\phi^2 - \frac{7}{12}\mathrm{k}\phi^4 \qquad (2.26)$$

This difference means that optical echoes emitted at different positions along the vapour will not be exactly in phase at the detector. Constructive interference between echoes from all parts of the sample will not occur if

the accumulated phase difference along the sample is much greater than π radians. Thus in a sample of length L, the maintenance of constructive interference requires

$$L(\mathrm{k}_e - \mathrm{k}) < \pi$$

Substituting equation 2.26 into this equation gives the phase matching requirement to second order as

$$\phi^2 < \pi/\mathrm{k}L$$

For the above typical value of k (1.4×10^7 m^{-1}) and a sample length of 100mm phase matching requires $\phi < 1.5$mrad. The phase matching requirement is independent of interpulse time. So for short delays, when the intensity reduction of section 2.5.1 (given by $e^{-2u_0^2\mathrm{k}^2\tau^2\phi^2}$) is small, this phase matching requirement will limit the angle ϕ.

2.5.3 Practical limit on angular separation between excitation pulses

As shown in sections 2.5.1 and 2.5.2 above, for the experiments with sample length of about 100mm and interpulse time of order 100ns, such as those to be described in chapter 5, the requirement to maintain a sufficiently large echo signal places a practical limit of about a milliradian, on the angular separation between the excitation pulses. Since the intrinsic laser beam divergence is of order one milliradian spatial filtering of the echo from the laser pulses, as mentioned at the beginning of this section, cannot be entirely achieved. Therefore other means of protecting the detector from the intense laser pulses must be found. Some possible techniques are briefly discussed in the next chapter where the basic theory behind the discrimination method used in the experiments of chapter 5 is also developed.

Chapter 3

Multi-state System And Theory Of The Rotation Of The Echo Polarisation

The two state model used in chapter 2 is an idealisation. Energy levels are usually degenereate or consist of two or more nearly-degenerate states. The $7P_{3/2}$ level of caesium, for example, consists of four hyperfine components with F values of 2, 3, 4 and 5 (see figure 5.2 on page 68) within a range of about 200MHz, each of which has 2F+1 Zeeman components that are exactly degenerate in zero magnetic field. If light polarisation properties of the echo are to be included in the theory it is necessary to take account of the spatial or Zeeman degeneracy of the levels. That is the main task of this chapter. The motive for this is a practical one. The detector, normally a photomultiplier tube, must be protected from the intense laser pulses that immediately preceed the echo pulses. To discriminate in favour of the echo one needs to block the excitation pulses and not the echo. This cannot be done using mechanical shutters, since the switching time needs to be a few tens of nanoseconds (i.e. much less than τ). Pockels Cell electro optical shutters [44] have opening times of this order of magnitude and have been widely used in echo experiments (see for example [51]). However they are quite difficult to set up, requiring precise alignment and accurate triggering, and so other techniques for discrimination against the laser pulses have been developed. One such approach is to use non-collinear excitation pulses and spatial filtering [6, 56]. However, as described at the end of chaper 2, the

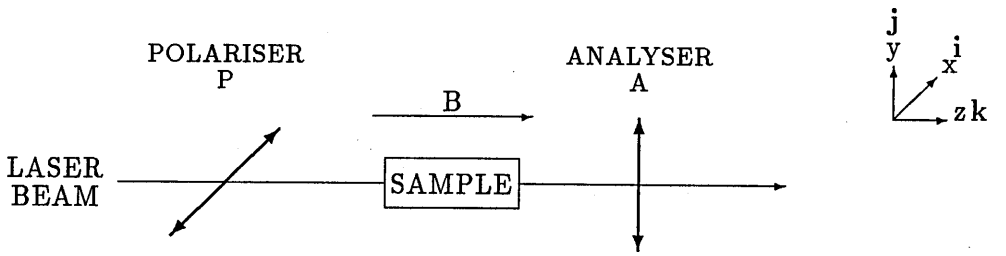

Figure 3.1 The geometry of an echo polarisation rotation experiment.

rapid fall off in echo intensity with angle, ϕ, between the excitation beams limits the effectiveness of this technique. In the experiments of chapter 5 effective discrimination is achieved by using the echo polarisation rotation technique first demonstrated by Aoki [2] and Baer and Abella [5]. In this technique (see figure 3.1) the sample sits between crossed polarisers with a weak magnetic field (a few gauss) applied in the axial direction (i.e. along the direction of propagation of the laser pulses). Thus the sample is excited by light pulses of definite polarisation, that of polariser P. The magnetic field lifts the Zeeman degeneracy of the levels and this results in the echo being formed with a polarisation different from that of the incident light pulses. Thus a component of the echo passes the analyser A. The magnetic field is too weak to allow a significant Faraday rotation [44] of the incident light pulses which are therefore effectively blocked by the analyser. With good quality polarisers the echo polarisation rotation technique is effective enough to be used without other forms of discrimination, although in practice a limited amount of spatial filtering is of additional help.

Analyses of the polarisation and quantum beating effects of degenerate and nearly-degenerate states on two-excitation-pulse echoes have been given by Gordon et al [38], Lambert et al [57] and Schenzle et al [79], and the application of the echo polarisation rotation on the caesium 6S-7P transitions has been worked out by Baer and Abella [5]($6S_{1/2}$-$7P_{1/2}$) and Aoki [2]($6S_{1/2}$-$7P_{3/2}$). The aim of this chapter is to give an outline only of the physical mechanisms involved, building on the two state theory of chapter 2.

This chapter is organised as follows. Echo polarisation rotation on a multi-level system can be analysed in terms of a number of separate three level systems. This is explained in section 3.1. In section 3.2 the three level system analysis is performed. This predicts quantum beats (echo intensity with magnetic field) as well as echo polarisation rotation (section 3.2.7). Section 3.3 introduces the additional concepts necessary for an analysis of echo polarisation rotation on a complex energy level structure and the result for caesium($6S_{1/2}$-$7P_{1/2}$) is quoted. This also shows the more complex nature of the resulting quantum beats.

3.1 Echo Polarisation Rotation

The light pulses are assumed to travel along the z-axis which is taken to be the quantisation axis of the atom. The electric vector of the light will then be polarised in the x-y plane, see figure 3.1. The first pulse, assumed to be linearly polarised, will therefore excite upward transitions from each ground level Zeeman sub-state component of magnetic quantum number m to two excited sub-states of magnetic quantum numbers $m \pm 1$, that is all σ transitions ($\Delta m = \pm 1$). For atoms such as caesium there is a large number of degenerate or nearly degenerate ground sub-states, due to hyperfine structure as well as magnetic degeneracy or near degeneracy, that will be excited by the first pulse. However, they are all initially uncorrelated in phase, and so the analysis can be carried through for each ground state sub-level independently. At the end of the calculation the echo intensities can then be simply added. The second pulse at a time τ later is also linearly polarised and will excite all σ transitions upwards from the uncorrelated ground states and downwards to ground state sub-levels from the excited states induced by the first pulse. The transitions induced from a single ground state sub-level by the two pulse sequence are shown schematically in in figure 3.2. The dipole moment of the atom (the expectation value $\langle \hat{\mathbf{d}} \rangle$) after the pulse sequence has passed will contain 'beat' terms describing the interference between excited state sub-level amplitudes and also between

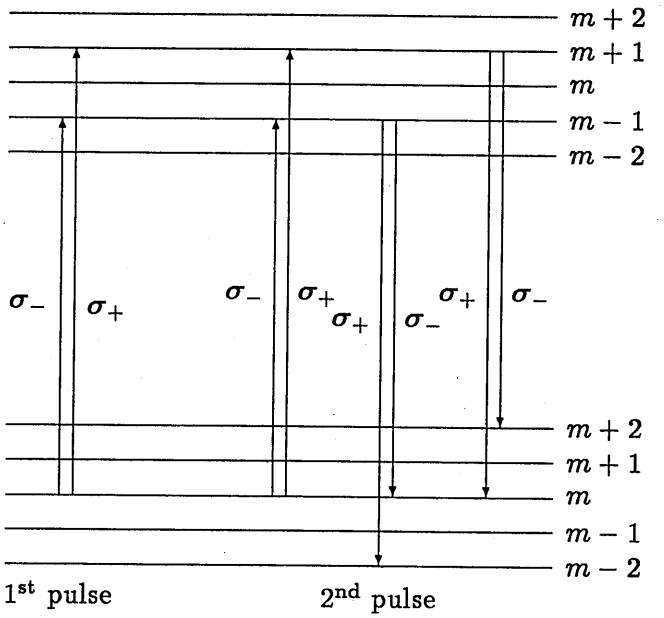

Figure 3.2 σ transitions, in a multilevel system, induced from a single ground state sub-level by a two pulse sequence of linearly polarised light.

ground state amplitudes, since the pulse sequence induces coherence between ground state sub-level amplitudes as well as between excited state sub-level amplitudes. The selection rules for the emission of σ light from the atoms restrict the number of allowed electric dipole moment terms in $\langle \hat{\mathbf{d}} \rangle$ to those for which $\Delta m = \pm 1$. For weak laser pulses this allows the transitions of figure 3.2 to be analysed separately in terms of two more simple groups of transitions describing separately beats between the excited state sub-levels and between the ground state sub-levels. Figure 3.3 shows a group of transitions for a single ground state.

For the purpose of illustrating the physical mechanisms involved the following analysis (section 3.2) will only consider the case of interference between excited sub-level amplitudes—excited state beats.

3.2 Echo Polarisation Rotation From Interference Between Upper State Amplitudes

The principle of echo polarisation rotation in its simplest form can be explained by considering the three level system of figure 3.4, which is similar

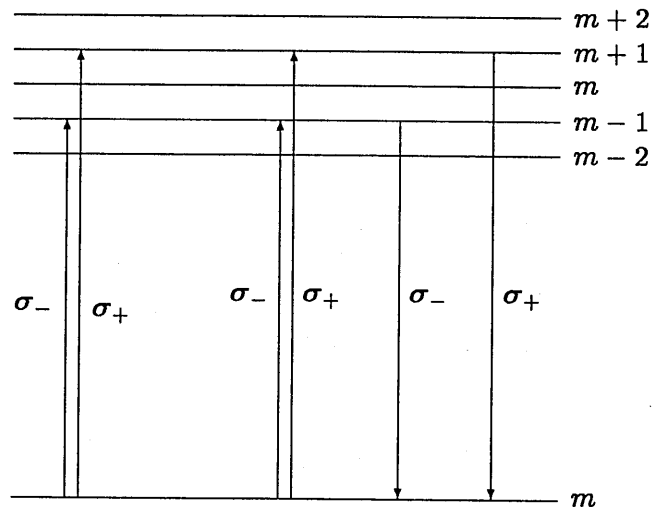

Figure 3.3 σ transitions induced in a system with a single ground state sub-level by a two pulse sequence of linearly polarised light.

to that used by Schenzle et al [79]. As explained above, in section 3.1, all other sub-levels will be ignored. The optical transition frequencies are $\omega_{\pm}$ which are detuned from the excitation laser frequency, ω_L, by

$$\Delta\omega_{\pm} = \omega_{\pm} - \omega_L$$

3.2.1 Modifications to the two state system

The following analysis will be similar to that in chapter 2 but with the modifications given below.

1. The pulse duration is short enough so that both transitions are excited in resonance. That is, it is assumed that the two upper levels are effectively degenerate during the two excitation processes but not, of course, during the free evolution periods between and after.

2. The pulse areas are assumed small enough so that the two transitions will not compete for the ground state population (see Schenzle et al [79] for the general case). Small angle approximations can then

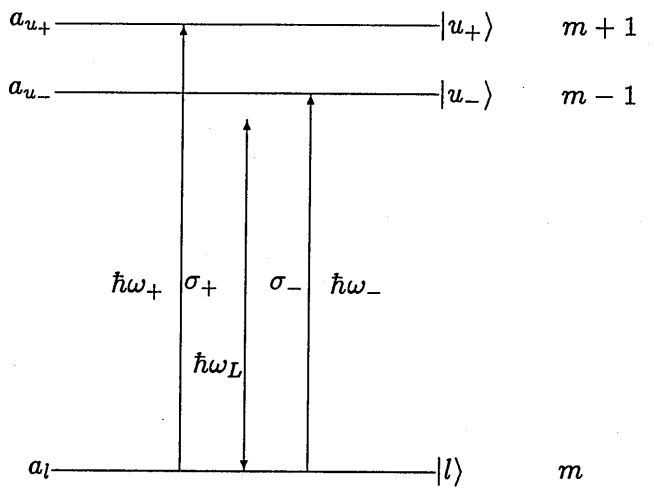

Figure 3.4 The three level system. ω_L is the laser frequency.

be applied. Thus equation 2.6 in the form

$$\begin{aligned} a_u(t) = &\quad A_u + \tfrac{i\theta}{2} e^{i\mathbf{k}.\mathbf{r}} A_l \\ a_l(t) = &\quad A_l + \tfrac{i\theta}{2} e^{-i\mathbf{k}.\mathbf{r}} A_u \end{aligned}$$

can be applied independently to each of the two transitions of the three level system.

3. The incident light is assumed to be linearly polarised along the x-axis, that is, the incident wave is

$$\mathcal{E}(t)\mathbf{i}\cos(\mathbf{k}.\mathbf{r} - \omega_L t)$$

where $\mathbf{i}$ is the unit vector in the x-direction. Also, for simplicity, it is assumed that $\mathcal{E}(t) = \mathcal{E}$, a constant, during the pulse, which has duration t_p.

4. The general state of the three level system at any time t is given by

$$|t\rangle = a_l(t)|l\rangle + a_{u-}(t)|u_-\rangle e^{-i\omega_- t} + a_{u+}(t)|u_+\rangle e^{-i\omega_+ t}$$

where $a_l(t)$, $a_{u-}(t)$ and $a_{u+}(t)$ are the slowly varying amplitudes. $\Delta\omega_\pm = \omega_\pm - \omega_L$ is very much smaller than the excitation laser frequency, ω_L, such that during the excitation process the laser can be

resonant with both optical transitions (Modification 1). However during the periods of free evolution the time dependence of the amplitudes is

$$a_{u_\pm}(t) \propto e^{-i(\omega_\pm - \omega_L)t} = e^{-i\Delta\omega_\pm t}$$

5. Because of the spatial degeneracy of the upper levels the electric dipole operator must be resolved into its components.

$$\hat{\mathbf{d}} = \hat{d}_x\mathbf{i} + \hat{d}_y\mathbf{j}$$

The spherical components [15] are

$$\begin{aligned} \hat{d}_\pm &= \mp(\hat{d}_x \mp i\hat{d}_y)/\sqrt{2} \\ \Rightarrow \hat{d}_x &= (\hat{d}_- - \hat{d}_+)/\sqrt{2} \\ \text{and } \hat{d}_y &= i(\hat{d}_- + \hat{d}_+)/\sqrt{2} \end{aligned}$$

The matrix elements of $\hat{\mathbf{d}}$ are given by

$$\begin{aligned} \mathrm{D}_+ &= \langle l|\hat{d}_-|u_+\rangle \\ &= \langle u_+|\hat{d}_+|l\rangle \end{aligned}$$

which is real by choice of ket $|u_+\rangle$,

$$\begin{aligned} \mathrm{D}_- &= \langle l|\hat{d}_+|u_-\rangle \\ &= \langle u_-|\hat{d}_-|l\rangle \end{aligned}$$

which is real by choice of ket $|u_-\rangle$, and all other matrix elements are equal to 0 [15].

6. Because of modifications 3 and 5 the pulse areas for each transition become

$$\begin{aligned} \theta_\pm &= \int_0^{t_p} \frac{\mathcal{E}}{\hbar}\mathbf{i}.\langle u_\pm|\hat{\mathbf{d}}|l\rangle dt \\ &= \frac{\mathcal{E}t_p}{\hbar}\langle u_\pm|\hat{d}_x|l\rangle \\ &= \frac{\mathcal{E}t_p}{\hbar\sqrt{2}}\langle u_\pm|\hat{d}_- - \hat{d}_+|l\rangle \\ &= \frac{\mathcal{E}t_p}{\hbar\sqrt{2}}(\mp\mathrm{D}_\pm) \end{aligned}$$

3.2.2 Excitation by a linearly polarised weak resonant light pulse

Using the above modifications and working through an analysis similar to that of chapter 2, the amplitudes following a weak resonant light pulse polarised in the x-direction can be obtained. If the pulse arrives at time $t = 0$ then the amplitudes for times $t > 0$ are (c.f. modification 2)

$$\left.\begin{aligned} a_{u_+}(t) = &\ (A_{u_+} &&+\tfrac{i}{2}\theta_+ e^{i\mathbf{k}.\mathbf{r}} A_l)e^{-i\Delta\omega_+ t} \\ a_{u_-}(t) = &\ (A_{u_-} &&+\tfrac{i}{2}\theta_- e^{i\mathbf{k}.\mathbf{r}} A_l)e^{-i\Delta\omega_- t} \\ a_l(t) = &\ A_l &&+\tfrac{i}{2}\theta_- e^{-i\mathbf{k}.\mathbf{r}} A_{u_-} \\ & && +\tfrac{i}{2}\theta_+ e^{-i\mathbf{k}.\mathbf{r}} A_{u_+} \end{aligned}\right\} \qquad (3.1)$$

where A_l, A_{u_-} and A_{u_+} are the initial ($t = 0$) amplitudes of the states $|l\rangle$,$|u_-\rangle$ and $|u_+\rangle$ respectively (i.e. before the pulse arrives). The state described by these equations is normalised only to first order in θ.

The next three sections correspond to steps 1, 2 and 3 of chapter 2 see page 22. Step 4 is more complicated when polarisation is considered and so is covered in two sections: 3.2.6 and 3.2.7.

3.2.3 Amplitudes following a two excitation pulse sequence

The excitation pulse sequence consists of pulses, labelled 1 and 2, arriving at times $t = 0$ and $t = \tau$. Before the first pulse the system is in its ground state:

$$A_{u\pm} = 0 \quad \text{and} \quad A_l = 1 \qquad\qquad (t < 0)$$

After the first pulse the amplitudes are given by applying equations 3.1

$$\left.\begin{aligned} a_{u_+}(t) &= \tfrac{i}{2}\theta_{1+} e^{i\mathbf{k}.\mathbf{r}(0)} e^{-i\Delta\omega_+ t} \\ a_{u_-}(t) &= \tfrac{i}{2}\theta_{1-} e^{i\mathbf{k}.\mathbf{r}(0)} e^{-i\Delta\omega_- t} \\ a_l(t) &= 1 \end{aligned}\right\} (0 < t < \tau) \qquad (3.2)$$

Just before the second pulse ($t = \tau$) the above three equations give the amplitudes as

$$A_{u\pm} \equiv a_{u\pm}(\tau) = \frac{i}{2}\theta_{1\pm}e^{i\mathbf{k}.\mathbf{r}(0)}e^{-i\Delta\omega_{\pm}\tau} \quad \text{and} \quad A_l \equiv a_l(\tau) = 1 \qquad (t = \tau)$$

After the second pulse the amplitudes are given by applying equations 3.1 again

$$\left.\begin{aligned} a_{u+}(t) &= (\tfrac{i}{2}\theta_{1+}e^{i\mathbf{k}.\mathbf{r}(0)}e^{-i\Delta\omega_{+}\tau} + \tfrac{i}{2}\theta_{2+}e^{i\mathbf{k}.\mathbf{r}(\tau)})e^{-i\Delta\omega_{+}(t-\tau)} \\ a_{u-}(t) &= (\tfrac{i}{2}\theta_{1-}e^{i\mathbf{k}.\mathbf{r}(0)}e^{-i\Delta\omega_{-}\tau} + \tfrac{i}{2}\theta_{2-}e^{i\mathbf{k}.\mathbf{r}(\tau)})e^{-i\Delta\omega_{-}(t-\tau)} \\ a_l(t) &= 1 + \tfrac{i}{2}\theta_{2+}e^{-i\mathbf{k}.\mathbf{r}(\tau)}\tfrac{i}{2}\theta_{1+}e^{i\mathbf{k}.\mathbf{r}(0)}e^{-i\Delta\omega_{+}\tau} \\ &\quad + \tfrac{i}{2}\theta_{2-}e^{-i\mathbf{k}.\mathbf{r}(\tau)}\tfrac{i}{2}\theta_{1-}e^{i\mathbf{k}.\mathbf{r}(0)}e^{-i\Delta\omega_{-}\tau} \end{aligned}\right\} (t > \tau) \qquad (3.3)$$

3.2.4 Evaluation of the expectation value for the atomic dipole moment

The expectation value for the atomic dipole moment after the second pulse can be found using the amplitudes of equations 3.3 for the state of the system (modification 4) and the matrix elements (modification 6). However, not all the terms thus obtained will contribute to an echo. In section 2.4.3 when the macroscopic polarisation was calculated only terms with a factor $e^{i(2\mathbf{k}.\mathbf{r}(\tau)-\mathbf{k}.\mathbf{r}(0))}$ rephased after $t = \tau$. They rephased at $t = 2\tau$ and resulted in the echo. This will also be the case for this analysis. Thus the expectation value for the atomic dipole moment, ignoring terms not leading to an echo, can be written as

$$\begin{aligned} \langle t|\hat{\mathbf{d}}|t\rangle_e = \; & -\tfrac{i}{8}e^{i(2\mathbf{k}.\mathbf{r}(\tau)-\mathbf{k}.\mathbf{r}(0))}e^{-i\omega_L t} \\ & \times\{(\theta_{1-}e^{i\Delta\omega_{-}\tau}\theta_{2-} + \theta_{1+}e^{i\Delta\omega_{+}\tau}\theta_{2+})\langle l|\hat{\mathbf{d}}|u_+\rangle\theta_{2+}e^{-i\Delta\omega_{+}(t-\tau)} \\ & +(\theta_{1-}e^{i\Delta\omega_{-}\tau}\theta_{2-} + \theta_{1+}e^{i\Delta\omega_{+}\tau}\theta_{2+})\langle l|\hat{\mathbf{d}}|u_-\rangle\theta_{2-}e^{-i\Delta\omega_{-}(t-\tau)}\} \\ & +\text{c.c.} \end{aligned} \qquad (3.4)$$

3.2.5 Averaging to give the macroscopic polarisation

Integrating equation 3.4 over the thermal velocity distribution and multiplying by n (see section 2.3.3) gives the macroscopic polarisation. At the echo time, $t = 2\tau$, and at position $\mathbf{R}$ the macroscopic polarisation will be given by

$$\begin{aligned}\mathbf{P}_e(\mathbf{R},2\tau) &= -\tfrac{in}{8}e^{i\mathbf{k}.\mathbf{R}-\omega_L 2\tau} \\ &\times\{\langle l|\hat{\mathbf{d}}|u_+\rangle\theta_{2+}(\theta_{1+}\theta_{2+}+\theta_{1-}\theta_{2-}e^{i(\Delta\omega_- -\Delta\omega_+)\tau}) \\ &+\langle l|\hat{\mathbf{d}}|u_-\rangle\theta_{2-}(\theta_{1-}\theta_{2-}+\theta_{1+}\theta_{2+}e^{i(\Delta\omega_+ -\Delta\omega_-)\tau})\} \\ &+\text{c.c.}\end{aligned} \tag{3.5}$$

The matrix elements in the above equation can be evaluated, by reference to modification 5 of section 3.2.1, and are given below:

$$\begin{aligned}\langle l|\hat{\mathbf{d}}|u_+\rangle &= \langle l|\hat{d}_x\mathbf{i}+\hat{d}_y\mathbf{j}|u_+\rangle \\ &= \langle l|\tfrac{\hat{d}_- -\hat{d}_+}{\sqrt{2}}\mathbf{i}+i\tfrac{\hat{d}_- +\hat{d}_+}{\sqrt{2}}\mathbf{j}|u_+\rangle \\ &= \tfrac{\mathrm{D}_+}{\sqrt{2}}\mathbf{i}+i\tfrac{\mathrm{D}_+}{\sqrt{2}}\mathbf{j} \\ &= \tfrac{\mathrm{D}_+}{\sqrt{2}}(\mathbf{i}+i\mathbf{j})\end{aligned}$$

also

$$\langle l|\hat{\mathbf{d}}|u_-\rangle = -\tfrac{\mathrm{D}_-}{\sqrt{2}}(\mathbf{i}-i\mathbf{j})$$

Substituting these matrix elements into equation 3.5 and expressing the pulse areas in terms of the matrix elements (modification 6) gives

$$\begin{aligned}\mathbf{P}_e(\mathbf{R},2\tau) &= -\tfrac{in}{8}e^{i(\mathbf{k}.\mathbf{R}-\omega_L 2\tau)}\tfrac{1}{\sqrt{2}}(\tfrac{t_p}{\hbar\sqrt{2}})^3\mathcal{E}_2^2\mathcal{E}_1 \\ &\times\{\mathrm{D}_+(\mathbf{i}+i\mathbf{j})\mathrm{D}_+(\mathrm{D}_+\mathrm{D}_+ + \mathrm{D}_-\mathrm{D}_-e^{i(\Delta\omega_- -\Delta\omega_+)\tau}) \\ &+\mathrm{D}_-(\mathbf{i}-i\mathbf{j})\mathrm{D}_-(\mathrm{D}_-\mathrm{D}_- + \mathrm{D}_+\mathrm{D}_+e^{i(\Delta\omega_+ -\Delta\omega_-)\tau})\} + \text{c.c.}\end{aligned}$$

where $\mathcal{E}_1$ ($\mathcal{E}_2$) is the electric field strength of the first (second) pulse.

3.2.6 The radiated echo field

Multiplying the first and second (i.e. the complex conjugate) terms of the echo macroscopic polarisation by $\pm i\frac{kL}{2\epsilon_0}$ respectively, as in section 2.3.4, gives

the radiated echo field as

$$\begin{aligned}\mathbf{E}_e(\mathbf{R},2\tau) = \; & \tfrac{n}{8}\tfrac{kL}{2\varepsilon_0}e^{i(\mathrm{k.R}-\omega_L 2\tau)}\tfrac{1}{4}(\tfrac{t_p}{\hbar})^3\mathcal{E}_2^2\mathcal{E}_1 \\ & \times\{(\mathrm{D}_+^4+\mathrm{D}_-^4)\mathbf{i}+i(\mathrm{D}_+^4-\mathrm{D}_-^4)\mathbf{j} \\ & +(\mathrm{D}_+\mathrm{D}_-)^2((e^{i(\Delta\omega_- -\Delta\omega_+)\tau}+e^{i(\Delta\omega_+ -\Delta\omega_-)\tau})\mathbf{i} \\ & +i(e^{i(\Delta\omega_- -\Delta\omega_+)\tau}-e^{i(\Delta\omega_+ -\Delta\omega_-)\tau})\mathbf{j})\} \; + \mathrm{c.c.}\end{aligned}$$

The exponentials of $\Delta\omega_\pm$ can be reduced to trigonometric functions giving

$$\begin{aligned}\mathbf{E}_e(\mathbf{R},2\tau) = \; & \tfrac{n}{64}\tfrac{kL}{\varepsilon_0}e^{i(\mathrm{k.R}-\omega_L 2\tau)}(\tfrac{t_p}{\hbar})^3\mathcal{E}_2^2\mathcal{E}_1 \\ & \times\{(\mathrm{D}_+^4+\mathrm{D}_-^4)\mathbf{i}+i(\mathrm{D}_+^4-\mathrm{D}_-^4)\mathbf{j} \\ & +2(\mathrm{D}_+\mathrm{D}_-)^2(\mathbf{i}\cos(\Delta\omega_+-\Delta\omega_-)\tau \\ & \qquad +\mathbf{j}\sin(\Delta\omega_+-\Delta\omega_-)\tau)\} \; + \mathrm{c.c.}\end{aligned} \tag{3.6}$$

The terms proportional to $\mathrm{D}_\pm^4$ describe echoes generated on a single transition involving a single ground state sub-level and a single upper state sub-level and are, of course, independent of $\Delta\omega_+$ and $\Delta\omega_-$. Terms proportional to $(\mathrm{D}_+\mathrm{D}_-)^2$ describe echoes resulting from both optical transitions. These echoes have a sinusodial dependance on the frequency difference $(\Delta\omega_+ - \Delta\omega_-)$.

The first term in the above equation, proportional to $(\mathrm{D}_+^4+\mathrm{D}_-^4)\mathbf{i}$, describes an echo with the same polarisation as the excitation pulses. The second term, proportional to $(\mathrm{D}_+^4-\mathrm{D}_-^4)\mathbf{j}$, gives an echo polarised in the orthoganal direction. However a study of the Clebsh-Gordon coefficients [15] shows that $\mathrm{D}_+^4 = \mathrm{D}_-^4$ if the substates $|u_+\rangle$ and $|u_-\rangle$ are from the same hyperfine level and $|l\rangle$ has $m = 0$ (see figure 3.4). Of more importance, if the whole of the Zeeman manifold is uniformly excited many echo terms with such 'difference' coeffecients will be formed. However, the symmetry properties of the Clebsh-Gordon coeffecients are such that all such terms cancel. If, on the other hand, the Zeeman manifold is non uniformly excited then the cancellation will not be complete and echoes with the orthogonal polarisation (along $\mathbf{j}$) will be observed. Only under exceptional experimental conditions (i.e. very narrow band width laser compared with the Zeeman splitting) would this be the case.

The final term of equation 3.6, proportional to $(D_+D_-)^2$, is the important one for the purposes of this chapter. It describes an echo with its plane of polarisation rotated through an angle $(\Delta\omega_+ - \Delta\omega_-)\tau$.

3.2.7 The transmitted component

The analyser is orientated with its pass axis along the unit vector **j**. Ignoring the term proportional to $(D_+^4 - D_-^4)$, for the reason described above in section 3.2.6, and forming the scalar product between the **j** vector and the radiated echo field of equation 3.6 gives

$$\begin{aligned}\mathbf{j}.\mathbf{E}_e(\mathbf{R},2\tau) &= \tfrac{n}{64}\tfrac{kL}{\varepsilon_0}e^{i(\mathbf{k}.\mathbf{R}-\omega_L 2\tau)}(\tfrac{t_p}{\hbar})^3\mathcal{E}_2^2\mathcal{E}_1 \\ &\quad\times\{2(D_+D_-)^2\sin((\Delta\omega_+ - \Delta\omega_-)\tau)\} + \text{c.c.}\end{aligned}$$

$$\begin{aligned}&= \tfrac{n}{16}\tfrac{kL}{\varepsilon_0}\cos(\mathbf{k}.\mathbf{R} - \omega_L 2\tau)\,(\tfrac{t_p}{\hbar})^3\mathcal{E}_2^2\mathcal{E}_1 \\ &\quad\times(D_+D_-)^2\sin((\Delta\omega_+ - \Delta\omega_-)\tau))\end{aligned}$$

Thus a component of the echo field proportional to $\sin((\Delta\omega_+ - \Delta\omega_-)\tau)$ will pass the analyser. In the case where the frequency difference is entirely due to Zeeman splitting then

$$\Delta\omega_+ - \Delta\omega_- = 2g\mu_B B/\hbar$$

for a sufficiently weak magnetic field, B, where g is the Landé factor of the upper level and μ_B the Bohr Magneton. Then peak echo intensity, I_e, would be a sinusodial function of $B\tau$.

$$I_e \propto (\frac{n}{16}\frac{kL}{\varepsilon_0}(\frac{t_p}{\hbar})^3\mathcal{E}_2^2\mathcal{E}_1(D_+D_-)^2)^2\sin^2(2g\mu_B B\tau/\hbar) \qquad (3.7)$$

If the splitting is due to hyperfine splitting then $(\Delta\omega_+ - \Delta\omega_-)$ is simply the angular frequency of this splitting. When both hyperfine and Zeeman splitting are present cross terms will also appear.

The principle of echo polarisation rotation is now clear. For the simple three level case described by equation 3.7 above, with a magnetic field $B = h/(8g\mu_B\tau)$ the rotated component of the echo polarisation is rotated by $\pi/2$ and completely passes the analyser. Varying the magnetic field, B, gives

intensity beats. In the experiments of chapter 5 the magnetic field, B, is varied to maximise the echo intensity, I_e, before performing an experimental run.

Following a similar approach as was used in this section (3.2) it can be shown that ground state Zeeman splitting will also give rise to echoes with rotated planes of polarisation.

3.3 The Caesium Atom

For a complex energy level structure, such as that of caesium (see figure 5.2 on page 68), the full analysis of polarisation rotation [2, 5] gives a series of echo amplitude terms with the polarisation beat factors $\sin((\Delta\omega_{m_1m_2} - \Delta\omega_{m_3m_4})\tau)$ where $\Delta\omega_{m_im_j}$ is the detuning of the transition frequency between the ground state sub-levels and the excited state sub-levels characterised by magnetic quantum numbers m_i and m_j. $m_1 = m_3 = m_2 + 1 = m_4 - 1$ represent echo terms involving excited state coherences as in section 3.2 while terms with $m_2 = m_4 = m_1 + 1 = m_3 - 1$ involve ground state coherences and other terms involve mixed coherences.

For example, equation 18 of reference [5] gives, for the $6S_{1/2}$(F=4)-$7P_{1/2}$ transition in caesium, the component of the echo macroscopic polarisation along the analyser pass axis direction as

$$\begin{aligned}\mathbf{P}_e(\mathbf{R}).\mathbf{j} \quad \propto\ & 924\sin(\Omega_2\tau/2) + 336\sin(\Omega_2\tau/6) \\ & + \cos(\Omega_1\tau)\{32\sin(\Omega_2\tau/2) - 12\sin(\Omega_2\tau/3) \\ & \qquad +6\sin(\Omega_2\tau/6) + 180\sin(2\Omega_2\tau/3) \\ & \qquad +126\sin(5\Omega_2\tau/6) + 56\sin(\Omega_2\tau)\}\end{aligned}$$

where $\Omega_1 = 2\pi \times 400.8$ MHz, the $7P_{1/2}$ hyperfine splitting, and $\Omega_2 = \mu_B B/\hbar$.

In an echo experiment with fixed τ, different terms will dominate the echo amplitude according to the value of B. Figure 5.19 on page 100 (see also [2, 5]) shows how the measured echo intensity on the 459nm(F=4) line varies with B for a chosen value of τ (95.1ns). The first peak in figure 5.19, for example, can be identified as being formed mainly from ground state coherences. That is when $\frac{\Omega_2\tau}{2} \simeq \frac{\pi}{2} \Rightarrow B \simeq \frac{\pi\hbar}{\mu_B\tau}$.

Theoretical treatments of the collisional relaxation of echoes formed on transitions between degenerate or near-degenerate levels [3, 91] show that in general the collisional relaxation rate can depend on the Zeeman sub-level populations and coherences involved, and hence on the chosen value of B and τ in experiments like those of chapter 5. In the case of the $6S_{1/2}$- $7P_{1/2}$ and $6S_{1/2}$- $7P_{3/2}$ caesium transitions, however, the sums of the total electronic angular momenta, j, ($\frac{1}{2} + \frac{1}{2} = 1$ and $\frac{1}{2} + \frac{3}{2} = 2$ respectively) are such that there is only one collisional relaxation rate. Therefore in the absence of possible B and τ dependent systematic errors (see section 5.5) the collisional relaxation rates measured in this work should be independent of the chosen value of B and depend on τ only through the diffractive velocity changing effects of collisions. Velocity changing collisional effects are discussed in chapter 4 and the experimental work is described in chapter 5.

Chapter 4

Collisional Relaxation Of Two-excitation-pulse Echoes

In chapters 2 and 3 an elementary theory of two-excitation-pulse echo formation was described with spontaneous decay and collisional effects neglected. In this chapter phenomenological decay constants and cross sections are used to describe collisional relaxation of echoes and these are then related to experimentally measurable quantities.

Since echo experiments are Doppler free it is possible to work at very low perturber gas pressures, where the impact and binary approximations will be valid. The theory described in this chapter, like that described in section 1.1.2, neglects resonant collisions, collisions with charged particles and inelastic collisions. Resonant collisions or active atom-active atom collisions are neglected because in echo experiments the active atom number density, n, is usually very much smaller than that of the perturber atoms, N ($N/n > 10^5$). For the caesium $6S_{1/2}$-$7P_{1/2}$ and $6S_{1/2}$-$7P_{3/2}$ transitions the energy levels are isolated and the $7P_{1/2}$-$7P_{3/2}$ inelastic 'transfer' cross section is very small [75] and makes a negligible contribution to the total collisional cross sections associated with the two optical transitions ($6S_{1/2}$-$7P_{1/2}$ and $6S_{1/2}$-$7P_{3/2}$) [20, 26, 54, 78, 85]. In a two level model of the transitions in caesium, collisions that mix the hyperfine and Zeeman populations will be regarded as elastic collisions.

The theory of chapters 2 and 3 gave the echo intensity (equations 2.20

and 3.7) as being proportional to n^2 where n was mean number density of atoms (i.e. active atoms, since the foreign gas was ignored in these chapters). This assumes that all active atoms in a given volume are radiating coherently at the echo time. With the effects of collisions and spontaneous decay included, not all active atoms will contribute fully to the echo. It can be shown [9, 10] that the effective rate of loss of contributing atoms due to spontaneous decay and collisions can be described by an equation of the form

$$\frac{dn}{dt} = -[\Gamma_{spon} + \Gamma(\tau)]n \tag{4.1}$$

where Γ_{spon} is the rate constant for loss of active atoms due to spontaneous decay ($\Gamma_{spon} \equiv 1/2\tau$ where τ_0 is the lifetime, see section 1.1.1(i)). $\Gamma(\tau)$ is an effective rate constant for loss by collisions in an echo experiment in which the interpulse time is τ. As will be shown in section 4.3 the effective rate constant increases with interpulse time, τ. This collisional rate constant is related to an effective velocity averaged collisional cross section, $\sigma(\tau)$, by

$$\Gamma(\tau) = N\sigma(\tau)\bar{v} \tag{4.2}$$

where $\bar{v} = \sqrt{8k_BT/\pi\mu}$ is the mean relative active-perturber colliding speed, μ being the reduced mass and N the number of perturber atoms per unit volume. At the low pressures studied the perturber gas pressure, P, obeys the ideal gas equation

$$P = Nk_BT \tag{4.3}$$

The effective number of active atoms at the echo time, $t = 2\tau$, can be found from integrating equation 4.1 for any fixed value of τ to give at the echo time, $t = 2\tau$,

$$n(2\tau) = n(0)e^{-2(\Gamma_{spon}+\Gamma(\tau))\tau} \tag{4.4}$$

$n(0)$ is the number of active atoms at time $t = 0$. The echo intensity is proportional to the square of the number of contributing atoms at the echo time, giving

$$I_e \propto \{n(2\tau)\}^2 \propto e^{-4\Gamma_{spon}\tau}e^{-4\Gamma(\tau)} \tag{4.5}$$

Substituting equations 4.2 and 4.3 into this equation gives

$$I_e \propto e^{-4\Gamma_{spon}\tau} e^{-\frac{4\tau\sigma(\tau)\bar{v}}{k_B T}P} \tag{4.6}$$

This equation is the basis for most echo studies of collisional processes. Two experimental approaches have been used:
(i) The measurements of echo decay with interpulse time, τ, keeping the foreign gas pressure fixed. Forber et al [35], Patel and Slusher [77] and Baer and Abella [4] and others have used this technique.
(ii) Measurements are taken with τ constant and the foreign gas (perturber) pressure, P, is varied. This technique is more commonly used in the optical region using pulsed dye lasers where it is difficult to keep the optical conditions constant while varying τ.

This latter approach is the one used in the experiments of chapter 5. Therefore equation 4.6 will be considered in the form

$$\log_e(I_e/I_0) = -\beta(\tau)P \tag{4.7}$$

where I_0 is the peak echo intensity in the absence of collisions and $\beta(\tau)$ describes the reduction in echo intensity due to collisions. $\beta(\tau)$ can be determined by measuring the decrease in echo intensity as the foreign gas pressure is increased, and the effective collisional cross section is then found from (see equation 4.6)

$$\beta(\tau) = \frac{4\sigma(\tau)\bar{v}\tau}{k_B T} \tag{4.8}$$

The effective collisional cross section, $\sigma(\tau)$, and the decay constant, $\Gamma(\tau)$, are functions of the interpulse time, τ, due to the effects of velocity changing collisions. These effects are introduced in section 4.1 and, along with phase interrupting collisions, are incorporated in a general theory of elastic collisions described in section 4.2. In section 4.3 the effective collisional cross section is interpreted in terms of phase interrupting and velocity changing collision cross sections. Finally, in section 4.4 a brief summary is given of three previous experimental echo studies of velocity changing collisions where lithium, sodium and ytterbium were used as active atoms.

4.1 Phase Interrupting and Velocity Changing Collisions

In section 1.1.2 the classical analysis of spectral line broadening by collisions [19, 33, 48, 65, 80, 86] was introduced and it was seen that the Weisskopf radius, b_W, was defined as that impact parameter which separated collisions into those with impact parameters $b < b_W$ which give rise to line broadening (random phase interruptions greater than about one radian) and those with $b > b_W$ not contributing to line broadening but resulting in line shifts (random phase interruptions less than about one radian). Collisions with $b < b_W$ shall be referred to as *phase interrupting collisions.*

In echo spectroscopy a phase interrupting collision ($b < b_W$) between an active atom and a perturber atom causes a loss of echo intensity because following such a collision the radiating dipole moment of the active atom has a large random phase, and so at the echo time it will not, on average, contribute to the echo signal. The cross section for phase interrupting collisions, σ_{pic}, can be simply related to the line broadening constants of traditional line broadening theory [19, 33, 48, 65, 80, 86] (see equation 4.16). Line shifts are not observed in echo spectroscopy since the echo is normally detected without spectral resolution. However the effects of collisions with impact parameters greater than the Weisskopf radius ($b > b_W$) can be observed in two-excitation-pulse echo experiments because of the small random velocity changes caused by these collisions. If as the result of a collision an active atom has its line-of-sight velocity component changed by a small random amount, Δv, then its emission frequency, due to the Doppler effect, changes by an amount kΔv where k is the optical wave number. After sufficient time the frequency change will result in a large random phase and so the atom will not, on average, contribute to the echo. Such velocity changes become important when

$$\mathrm{k}\Delta\mathrm{v}\Delta t \sim \pi \tag{4.9}$$

where Δt is the effective time between the collision and the observation (echo time). Such collisions, with $b > b_W$, will be referred to as *velocity chang-*

ing collisions. This terminology, however, can be misleading since phase interrupting collisions ($b < b_W$) also result in a change of the atom's centre-of-mass velocity. However the effect of these velocity changes will not be observable since the atom will have acquired a large random phase interruption immediately following the collision and will not therefore be able to contribute to the echo. Only collisions which result in velocity changes *alone*, that is those with $b > b_W$, will be called velocity changing collisions in the remaining sections of this chapter. It will be seen in section 4.2 that such velocity changing collisions arising from large impact parameter collisions ($b > b_W$) must be treated quantum mechanically and therefore are often termed diffractive velocity changing collisions.

In any experiment the effects of velocity changing collisions will only be observable if the radiating atoms are observed over a long enough period, Δt, for the random phase to become of order π (see equation 4.9), and if the coherence is not lost through any other mechanism during the interval Δt. In traditional spectroscopy the coherence time is $t_{coh} \sim (\delta\nu_{Doppler})^{-1}$ and this is much too short for collisional velocity changing effects to be observed. In Doppler-free spectroscopy $t_{coh} \sim (\delta\nu_{natural} + \delta\nu_{pressure})^{-1}$ which at low pressures can be quite large. Non-linear laser spectroscopic techniques such as saturation spectroscopy and the spectroscopy of a three level system can in principle be used to investigate velocity changing collisions. These techniques have been discussed by Berman [9, 10]. However, to date, the only unambiguous experimental information on collisional velocity changes have come from echo experiments [8, 34, 37, 49, 51, 53, 71, 74, 83]. This is because in a two-excitation-pulse echo experiment the effective observation interval, Δt, is of order the interpulse time, τ, which is an adjustable parameter limited only by laser pulse duration (short τ limit) and the effects of spontaneous decay (large τ limit).

Finally, notwithstanding the above definition of velocity changing collisions and for the sake of completeness, other types of echo experiments are mentioned where the velocity changing effects of collisions are not obscured by phase interruptions for any value of the impact parameter. This is either

because collisional phase interruptions do not occur ((i) below) or because the experiment is to some degree insensitive to collisional phase interrupting collisions ((ii) below).

(i) Collisional phase interruptions do not occur on vibrational-rotational transition belonging to the same electronic state. Echo experiments on such transitions are discussed by Shoemaker [83] and Berman et al [8]. In this case collisions perturb both energy levels of the transition to the same extent and so no phase interruption results directly from the collision (b_W is effectively zero) and all velocity changes will be observable if the observation period, 2τ, is large enough.

(ii) Stimulated echoes [49, 53, 37, 74] are generated by a sequence of three excitation pulses and it is between the second and third excitation pulses that the effects of phase interrupting collisions are not observable. This is because during this interval, τ_{23}, the echo information is carried not by the relative phase of the two level amplitudes (this would be randomised by a phase interrupting collision) but by the populations of the levels. Populations, of course, do not carry any information on the relative phase of the two levels which is why phase interrupting collision have no effect during the interval τ_{23}. The velocity changing effects of all collisions ($b > b_W$ and $b < b_W$) in this interval can therefore be studied. Stimulated echoes are further discussed in section 6.2.

4.2 A General Theory of Elastic Collisions

The analysis of collisions between atoms in energy eigenstates is a text book problem [21]. Although it may be impossible to calculate the scattering angles, due to imprecise knowledge of the interatomic potentials, this is a practical difficulty not a fundamental one. A point of considerable importance for what follows is the transition from a classical to a quantum treatment of collisions for large impact parameters.

The scattering must be treated quantum mechanically when the uncertainty in propagation direction exceeds the scattering angle. In such cases

the wavepacket of the atom follows a diffraction cone. In a classical description the active atom can be considered initially to approach the stationary perturber with forward momentum equal to p and with zero transverse momentum. The condition for a classical description can be found by considering the uncertainty principle. If the impact parameter is defined with an uncertainty δb then there is an associated uncertainty in the transverse momentum, $\delta p \geq \frac{\hbar}{2\delta b}$. This uncertainty in the transverse momentum as a fraction of the forward momentum, p, gives the angular uncertainty for the atom's direction of travel (small angle approximation). When this angular uncertainty exceeds the angle of scatter following the collision then a quantum treatment of the collision is necessary. Taking Θ to be the scattering angle the condition for a classical description is given by

$$\Theta > \frac{\delta p}{p} \geq \frac{\hbar}{2p\delta b}$$

Much of spectroscopy involves the study of atoms in superposition states. The analysis of elastic scattering of an atom in a superposition of energy eigenstates involves conceptual difficulties. The nature of these conceptual difficulties is as follows. Suppose the interaction between an active atom and a perturber is state dependent. Figure 4.1 shows the different trajectories that would be followed by ground state atoms (1) and excited state atoms (2). Now consider an atom in a linear superposition of these two states. What trajectory will the atom follow after the interaction and how is the radiating dipole moment of the atom affected?

Traditional line broadening theories [19, 33, 48, 65, 80, 86] do not address this question. Only recently has the situation become clarified mainly through the work of Berman and his associates [7, 9, 10]. The remainder of this chapter is concerned with the concepts involved in this work and the application to collisional relaxation of echoes. The main point of interest is the way in which collisions are classified as phase interrupting or velocity changing.

Consider figure 4.1 which shows an atom in a superposition state scattering from a stationary perturber. If the interaction is state dependent then it is necessary to associate different trajectories with the two components

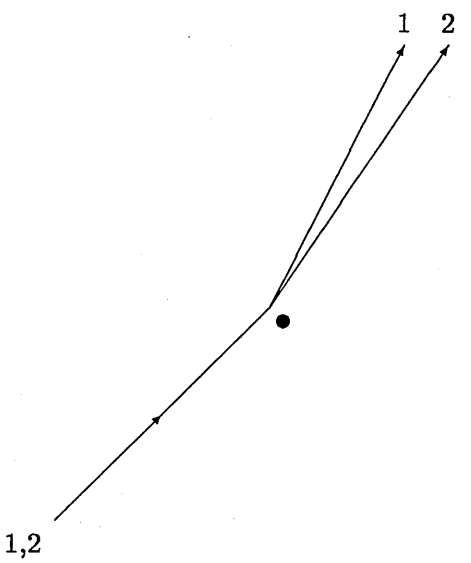

Figure 4.1 After a collision with an inert foreign gas atom the 'active' atom follows one of two distinct trajectories.

of the superposition state. The atomic dipole moment which involves the overlap integral of the two component state wave functions must vanish as the trajectories separate. Following such a collision the atom will not therefore contribute to any coherent radiation process such as the formation of an echo signal. This picture applies to small impact parameter collisions where the scattering angles are larger than the quantum uncertainties in propagation directions and could be treated classically. Now consider figure 4.2 which again shows an atom in a superposition state scattering in a state dependent manner from a stationary perturber. However in this case, because the impact parameter is large, the quantum uncertainties exceed the scattering angles and the diffractive scattering cones overlap for the two components of the superposition state. The expectation value for the atomic dipole moment therefore will be non zero and the atom will contribute to the echo unless prevented from so doing by the effects of any velocity changes induced by the collision. It is line-of-sight velocity changes that can cause a loss of echo intensity as discussed in section 4.1. A diffractive collisional calculation for large impact parameters is given at the end of this chapter to predict under what circumstances velocity changing collisional effects will be observable in the experiments of chapter 5.

Berman [9, 10], using this totally different theoretical approach, showed that the Weisskopf radius, b_W, of traditional line broadening theory was still the impact parameter that separated these two types of collision: phase interrupting (distinct trajectory) and velocity changing (overlapping diffraction cones).

4.3 Interpretation of the Effective Collisional Cross Section

The details of elastic scattering are given in the papers of Berman et al [9, 10]. When applied to two-excitation-pulse echo experiments they give the

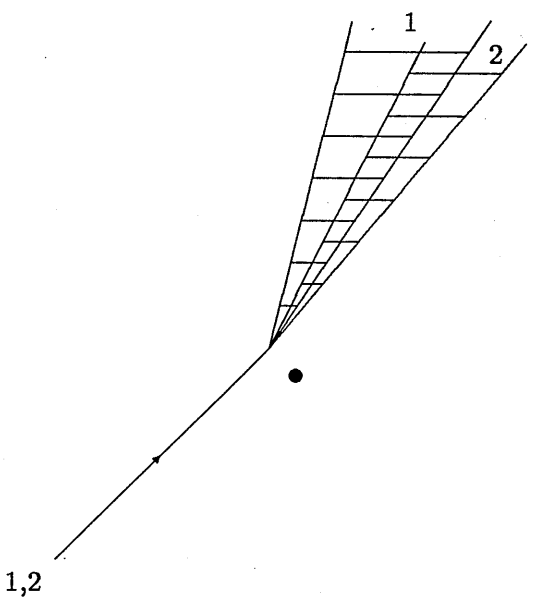

Figure 4.2 After a collision with large impact parameter the two possible paths of the active atom may overlap due to quantum mechanical uncertainty.

number of coherently radiating atoms at the echo time, 2τ, as

$$n(2\tau) = n(0)\exp -2\int_{t=0}^{\tau}\{\Gamma_{spon} + \Gamma_{pic} + \Gamma_{vcc}\langle 1 - \cos(\mathrm{k}\Delta\mathrm{v}(\tau - t))\rangle_{\Delta\mathrm{v}}\}dt \tag{4.10}$$

where $-2\int_{t=0}^{\tau}\{\Gamma_{pic} + \Gamma_{vcc}\langle 1 - \cos(\mathrm{k}\Delta\mathrm{v}(\tau - t))\rangle_{\Delta\mathrm{v}}\}dt$ equals the $-2\Gamma(\tau)\tau$ of equation 4.4. Γ_{pic} is the rate constant for phase interrupting collisions. Γ_{vcc} is the rate constant for all velocity changing collisions (with $b > b_W$) regardless of whether or not a large random phase has accumulated. The factor $-\Gamma_{vcc}\langle\cos(\mathrm{k}\Delta\mathrm{v}(\tau - t))\rangle_{\Delta\mathrm{v}}$ takes account of the fact that an atom suffering a collisional velocity change will still contribute to the echo, but with a random phase factor $\mathrm{k}\Delta\mathrm{v}(\tau - t)$. This term therefore appears in equation 4.10 as an apparent gain term. The angled brackets indicate an average over $\Delta\mathrm{v}$, the line-of-sight velocity change caused by a collision. The integral is over the interval $t = 0$ to $t = \tau$ (rather than $t = 0$ to $t = 2\tau$) because the maximum time for accumulation of random phase is τ and not 2τ due to the phase reversal induced by the second pulse (see Appendix A). There are two intervals of length τ between $t = 0$ and $t = 2\tau$ hence the factor 2 multiplying the integral in equation 4.10. Performing the integration gives

$$n(2\tau) = n(0)\exp -\{\Gamma_{spon} + \Gamma_{pic} + \Gamma_{vcc}\langle 1 - \frac{\sin \mathrm{k}\Delta\mathrm{v}\tau}{\mathrm{k}\Delta\mathrm{v}\tau}\rangle_{\Delta\mathrm{v}}\}2\tau$$

Comparing this equation with equation 4.4 shows

$$\Gamma(\tau) = \Gamma_{pic} + \Gamma_{vcc}\langle 1 - \frac{\sin \mathrm{k}\Delta\mathrm{v}\tau}{\mathrm{k}\Delta\mathrm{v}\tau}\rangle_{\Delta\mathrm{v}}$$

and using equation 4.2 and two similar equations, namely

$$\Gamma_{pic} = N\sigma_{pic}\bar{\mathrm{v}} \tag{4.11}$$

$$\Gamma_{vcc} = N\sigma_{vcc}\bar{\mathrm{v}}$$

gives

$$\sigma(\tau) = \sigma_{pic} + \sigma_{vcc}\langle 1 - \frac{\sin \mathrm{k}\Delta\mathrm{v}\tau}{\mathrm{k}\Delta\mathrm{v}\tau}\rangle_{\Delta\mathrm{v}} \tag{4.12}$$

For large interpulse times, $\mathrm{k}\Delta\mathrm{v}\tau \gg 1$, the sinc function in the above equation averages to zero and therefore

$$\sigma(\tau) = \sigma_{pic} + \sigma_{vcc} \qquad (\mathrm{k}\Delta\mathrm{v}\tau \gg 1)$$

This implies that for large interpulse times the effective collisional cross section is the sum of the collisional cross sections for phase interrupting and velocity changing collisions. That is, all collisions cause a loss of echo intensity. For short interpulse times ($k\Delta v\tau \ll 1$) equation 4.12, using second order expansion, becomes

$$\sigma(\tau) = \sigma_{pic} + \sigma_{vcc}k^2\langle\Delta v^2\rangle\tau^2/6 \qquad (k\Delta v\tau \ll 1) \qquad (4.13)$$

A graph of the effective cross section, $\sigma(\tau)$, against τ^2 is therefore initially a straight line with an ordinate intercept of σ_{pic}. Its gradient, m, with respect to τ^2 is harder to interpret since both $\langle\Delta v^2\rangle$ and σ_{vcc} are unknown. Taking M as the mass of the active atom, an analysis of scattering using a double hard sphere model [9] gives

$$\delta u = 2(2\pi)^{1/2}\hbar/M(\sigma_{pic} + \sigma_{vcc})^{1/2} \qquad (4.14)$$

δu is the average magnitude of the collisional velocity change following a diffractive velocity changing collision. It is related to the line-of-sight or axial velocity change, Δv, by

$$\langle\Delta v^2\rangle = \frac{1}{3}\delta u^2$$

Using these equations with equation 4.13 gives

$$\sigma_{vcc} = \sigma_{pic}\frac{1}{(\frac{2\hbar k}{3M})^2\frac{\pi}{m} - 1} \qquad (4.15)$$

where $m = \sigma_{vcc}k^2\langle\Delta v^2\rangle/6$ is the gradient of the line of $\sigma(\tau)$ against τ^2 (see equation 4.13).

σ_{pic} is related to the broadening constant of traditional line broadening spectroscopy where only phase interrupting collisions can be observed (see section 4.1). The effective time between phase interrupting collisions, T_{coll}, equals Γ_{pic}^{-1} and equation 1.1 becomes

$$\gamma = \frac{\Gamma_{pic}}{2\pi N}$$

Eliminating Γ_{pic}/N from this equation using equation 4.11 gives

$$\gamma = \frac{\sigma_{pic}\overline{v}}{2\pi} \qquad (4.16)$$

which relates the phase interrupting collisional cross section to the line broadening constant, γ, of traditional spectroscopy.

4.4 Experimental Observations of Diffractive Velocity Changing Collisions

A number of two-excitation-pulse echo relaxation measurements, performed on optical transitions in atomic metal vapours perturbed by noble gases, have shown that diffractive velocity changing collisional effects can make an important contribution to the echo relaxation. These are now discussed.

The effective collisional cross sections as a function of interpulse time, τ ($0 < \tau <$54ns), measured by Mossberg et al [71] for the sodium 3S-3P transitions were limited to the initial quadratic regime, shown in equation 4.13, by the short 3P lifetime (i.e. large Γ_{spon} in equation 4.4). The effective collisional cross sections for lithium 2S-2P and ytterbium $(6s^2)^1S_0$–$(6s6p)^3P_1$ have been measured by Kachru et al [51] and Forber et al [34] respectively. As predicted in section 4.3, the effective collisional cross sections show an initial quadratic rise and then asymptotically approach an upper limit as the interpulse time is increased. The results of both these experiments imply that the phase interrupting and velocity changing collisional cross sections are approximately equal. It is possible to perform these large interpulse time measurements for ytterbium because its $(6s6p)^3P_1$ state lifetime is long (875ns). The measurements were performed with interpulse times between 200 and 7000ns. Lithium's small atomic mass (7amu) means that its characteristic collisional velocity changes will be large (see below or equation 4.14). Thus for lithium velocity changing collisional effects are observable at small interpulse times and both the initial quadratic rise and asymptotic approach to an upper limit are observed between 10 and 100ns.

To predict whether diffractive velocity changing collisional effects will be observable, in the experiments of chapter 5, it is necessary to estimate the average magnitude of the change in the line-of-sight velocity component, Δv, following such a collision. These collisions need to be considered quantum

mechanically [9]. The perturber atom is treated as a stationary opaque obstacle (hard sphere) and the active atom as a plane wave, of de Broglie wavelength λ_B travelling perpendicularly to the echo direction.

$$\lambda_B = h/M\mathrm{v}$$

where M is the mass of the active atom and v its speed. The effective size of the perturber is the Weisskopf radius, b_W. Small angle Fraunhofer diffraction implies

$$\frac{\Delta \mathrm{v}}{\mathrm{v}} \sim \frac{\lambda_B}{2b_W}$$

Therefore

$$\Delta \mathrm{v} \sim \frac{h}{2Mb_W}$$

For electric dipole transitions $b_W \sim 5 - 10$Å and for caesium M=133amu. Thus Δv $\sim$2ms^{-1} and equation 4.9, with k$\sim 10^7$m^{-1}(i.e. caesium 6S-7P), implies

$$\Delta t \sim \pi/(2\mathrm{ms}^{-1} \times 10^7\mathrm{m}^{-1}) \sim 10^{-7}\mathrm{s}$$

Thus velocity changing collisional effects should be observable in the experiments of chapter 5 for delay times of about 100ns. Since the caesium 7P lifetime is about 120ns the observable diffractive velocity changing effects can be expected to be limited to the initial quadratic regime.

Chapter 5

Two-excitation-pulse Echo Experiments Using The Polarisation Rotation Technique

This chapter describes the experiments measuring the collisional relaxation of two-excitation-pulse echoes on the caesium $6S_{1/2}$-$7P_{1/2}$ (459nm) and $6S_{1/2}$-$7P_{3/2}$ (455nm) transitions perturbed by noble gases (He, Ar or Xe). The experiments were carried out using a range of inter pulse times, τ, from about 30 to 200ns and used the echo polarisation rotation discrimination technique.

The apparatus used is described in section 5.1. The preliminary experiments to establish suitable operating conditions for the experiment are discussed in section 5.2 and in section 5.3 the experimental procedure used for measuring the echo relaxation is described. In section 5.4 the results are presented and discussed. Since this is the first application of the echo polarisation rotation technique to collisional studies, an investigation of possible systematic effects that might affect the results has been made. This investigation is described in section 5.5. In section 5.6 the results of this work are compared with previous relevant results. Finally, in section 5.7 possible improvements to the apparatus are discussed.

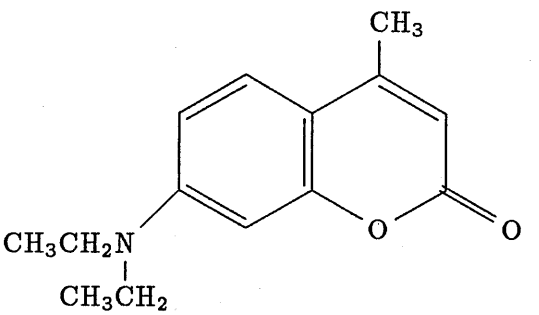

Figure 5.1 7-diethylamino-4-methylcoumarin.

5.1 Apparatus

The apparatus used in this study is a modified version of that used by Durrant and Manners [25]. Specific modifications were:

- The introduction of a variable delay time between the excitation pulses.
- The use of a boxcar averager (rather than a linear gate).
- The facility to remove the noble gas slowly from the oven.
- The use of computer monitoring and digital data handling.

The apparatus as used in the present work is described in the rest of this section.

5.1.1 The optics

A Molectron DLII dye laser, pumped by a Molectron UV12 nitrogen laser, produces pulses of about 7 nsec duration with a peak power of about 400kW at a repetition rate of 1–50Hz. The dye used is a 10^{-2}M solution of 7-diethylamino-4-methylcoumarin in ethanol (see figure 5.1), which lases at blue wavelengths. The wavelengths of interest in this work are 455.6nm and 459.4nm which are, respectively, the wavelengths of the $6S_{1/2}$- $7P_{3/2}$ and $6S_{1/2}$- $7P_{1/2}$ transitions in caesium (see figure 5.2). These wavelengths are near the peak of the dyes range. The dye laser has a linewidth of about

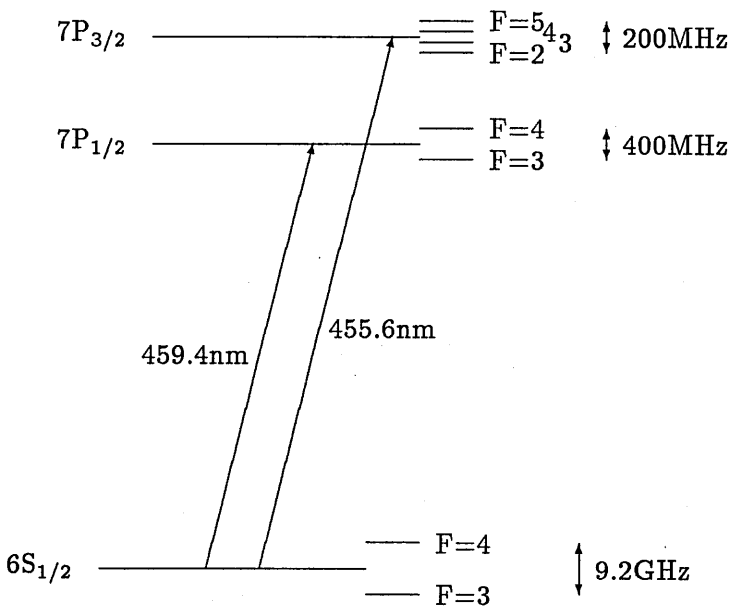

Figure 5.2 The caesium energy levels of interest in this work. The hyperfine splitting is not to scale.

10GHz which can be reduced to approximately 1GHz by using an intracavity etalon. A 1GHz linewidth will easily resolve the ground state ($6S_{1/2}$) hyperfine splitting of 9.2GHz in caesium but not the hyperfine splittings of the excited states ($7P_{1/2}$ and $7P_{3/2}$) (see figure 5.2). The dye laser pulse, on leaving the laser, contains about 10^{14} photons and the beam divergence is about one milliradian. The optical arrangement is shown in figure 5.3. A weak pulse tapped from the laser beam using a beam splitter (BS1 in figure 5.3) triggers the timing of the detection electronics by activating a fast photodiode (FPD in figure 5.3). The remainder of the laser beam is focused by a lens on to a pin hole (not shown), with a diameter of about 250μm, to improve the beam quality. The beam is then made parallel again by a second lens. These two lenses have focal lengths of 36 and 48mm respectively. A dielectric coated beam splitter (BS2 in figure 5.3) is used to split the beam in the ratio of 1:4 in intensity. The transmitted beam, which is the higher intensity one, enters a White cell optical delay line (see section 5.1.5) which introduces the required time delay, τ, between the two pulses. At beam splitter BS3 the delayed and undelayed beams are recombined, and by careful

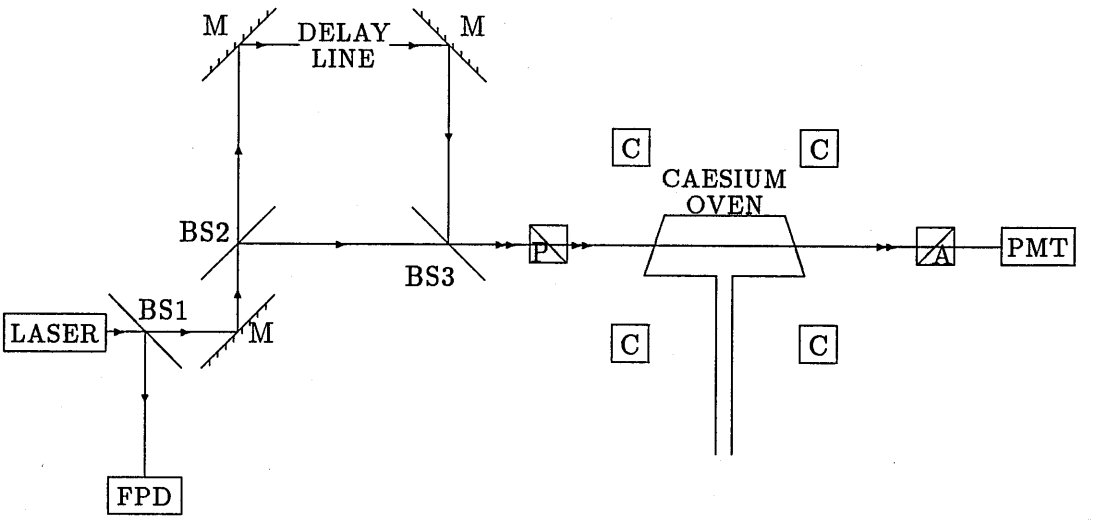

Figure 5.3 Schematic diagram of the optics. Arrowed lines represent laser beams. BS: beam splitter; M: mirror; FPD: fast photodiode; P: polariser; A: analyser; C: Helmholtz coil; PMT: photomultiplier tube.

alignment, made collinear to about one milliradian. This combined beam, composed of two pulses, then passes through a Glan Taylor polariser (P in figure 5.3). Both pulses are therefore linearly polarised in the same direction, as required for the polarisation rotation technique. The beams entering the oven have a diameter of about 4mm and a peak power during the pulse of about 100W. On leaving the oven the two excitation pulses are followed by the echo, some 10^6 times weaker in intensity. The axial magnetic field of a few gauss which is required for the polarisation rotation discrimination technique is provided by a pair of Helmholtz coils. The field (see figure 5.4) is uniform over the length of the oven to within about 4% except in the region near the baffles which constitutes about a tenth of the oven's length, where a small change occurs. Precise knowledge, or uniformity, of the field is not required as long as a suitable value is established experimentally to provide adequate discrimination for the echo (see section 3.2.7). A second Glan Taylor polariser, the analyser (A in figure 5.3), is placed after the oven with its pass axis orthogonal to the polariser's. This therefore transmits the polarisation rotated echo whilst the excitation pulses are attenuated by a factor of

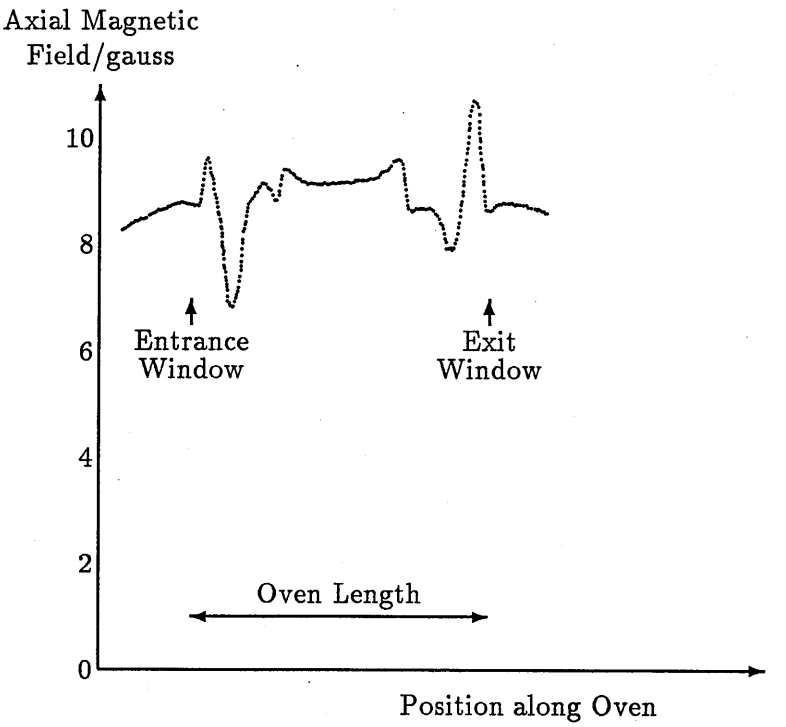

Figure 5.4 Axial magnetic field in the oven, measured using a Hall probe, for a 1 ampere current. Window positions are marked by arrows.

between 10^5 and 10^6. Faraday rotation of the excitation pulses is not a significant problem (see section 5.2.3). After passing through the analyser the pulse train consists of three pulses of approximately equal intensity: the two substantially attenuated excitation pulses and the echo. The beam is passed through neutral density filters, focused on to a pin hole at the entrance to a light-tight box and guided on to a fast, linear focused photomultiplier tube, Thorn EMI type 9826B (PMT in figure 5.3). The photomultiplier tube was run at 0.95kV and has a rise time of 2.2ns. The light-tight box is used to exclude stray scattered laser light. To reduce unwanted reflections the inside of the box is lined with black velvet. The output from the photomultiplier tube is fed to the electronic monitoring system.

5.1.2 The electronic monitoring system

The output from the photomultiplier tube, a sequence of three pulses (each a few milliamperes peak), is passed to an EG&G boxcar averager; a model 162 mainframe with two 165 gated integrators (see figure 5.5). The gate of one integrator is set to open when the pulse corresponding to the echo arrives. The other integrator, used for monitoring purposes to assess the stability of the laser, has its gate set to open at the time of the first pulse. The boxcar triggering is controlled by the output from the fast photodiode. The integrators are used with 15ns gates to isolate the appropriate pulse.

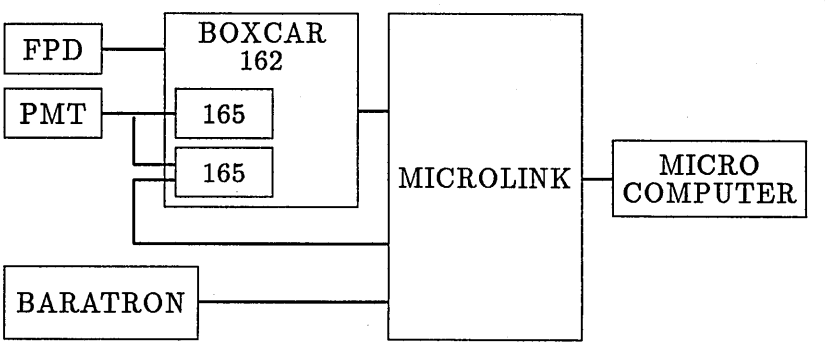

Figure 5.5 Schematic diagram of the electronic monitoring system. Solid lines represent electrical connections. PMT: photomultiplier tube; FPD: fast photodiode.

The integrator time constant of $10\mu s$ is used and gives an apparent time constant of about half a second with an improvement in the signal-to-noise ratio of about 6 [27]. The mainframe provides further smoothing so that the boxcar output is an average over the previous hundred or so pulses. A microcomputer, a Hewlett Packard HP-86, running some home written software (see Appendix C.1) stores these values of averaged pulse intensity measured simultaneously with the corresponding values of the noble gas pressure, on $5\frac{1}{4}$inch floppy disc. The pressure is measured by a baratron as discussed in section 5.1.3. The stored data is later analysed by the microcomputer as

discussed in section 5.3.3.

The boxcar and baratron outputs are analogue voltages. These are converted to digital values by a data acquisition interface, a Biodata microlink III. The present microlink system includes a 12-bit analogue to digital converter and three single channel analogue inputs, with secondary addresses of 0, 1 and 2. These are used respectively to measure the baratron output (noble gas pressure), the first boxcar output (the echo intensity) and the second boxcar output (the first pulse intensity). The computer obtains a value for the noble gas pressure, for example, by running a software sequence like:

```
SEND 5 ; TALK 7 SCG 0 MLA
ENTER 5 ; USING "#,W" ; X
SEND 5 ; UNT
```

The first of these lines SENDs a message to the IEEE-488 bus. The bus has an address of 5. The IEEE-488 bus links the computer to all its peripheral devices. These include a graphics plotter, with primary address 5, and the microlink, with primary address 7. The first line of the above software sequence sets the interface on the bus with primary address 7 (i.e. the microlink) to TALK. The SCG 0 selects the module with secondary address 0 (i.e. the module which is monitoring the baratron output) and the MLA (my listen address) sets the computer as a listener on the bus. The second line uses the ENTER statement to signal to the microlink that the computer is ready to receive data. The #,W image is used since the data is to be transferred as two bytes but then treated as a single 12 bit integer which will be stored as the variable X. The final line removes the microlink's ability to TALK with the UNTalk command. The variable X is converted to be equal to the pressure in torr before being stored on disc:

```
PRESSURE=0.9*X/4095
```

where 4095 is $2^{12} - 1$ and the 0.9 has been chosen to obtain the correct scaling.

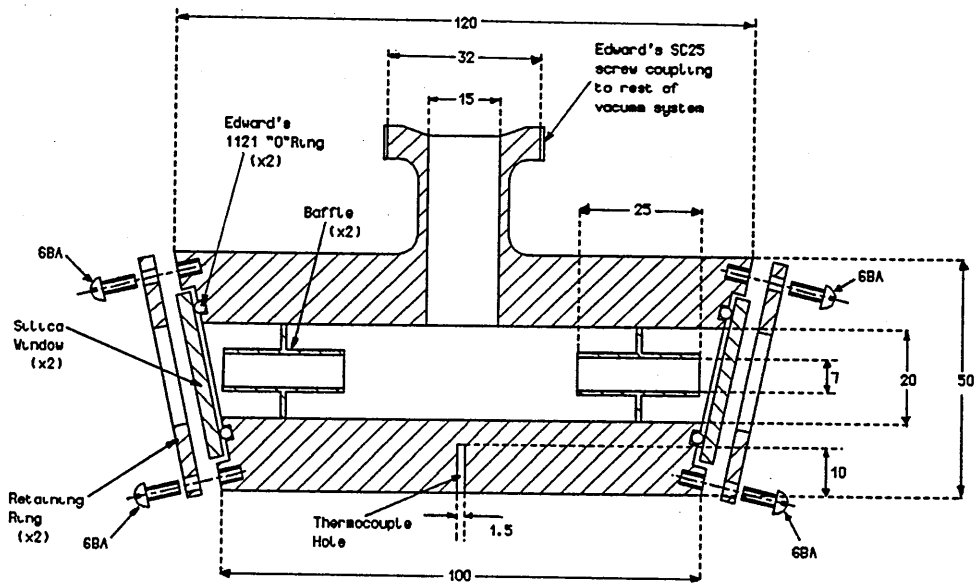

Figure 5.6 The caesium oven. All dimensions are in millimetres.

5.1.3 The oven and gas handling system

The oven which contains the caesium vapour is shown in figure 5.6. The body of the oven was turned from a piece of 2 inch stainless-steel bar and is about 100mm in length. The oven has an internal diameter of 20mm. The cylindrical baffles, of 7mm diameter, reduce the problem of window fogging (see section 5.1.4). The oven end windows are set at an angle of about 20° from the normal to the laser beam to avoid multiple reflections. These windows are silica discs which were chosen for their small strain birefringence, since the polarisation rotation technique relies on the excitation pulses maintaining their polarisation (see chapter 3). The end windows are seated on viton 'O' rings and held in place when the oven is in opera-

tion by atmospheric pressure, and not by the retaining rings since they can cause significant strain birefringence. Adequate temperature stability and homogeneity (see section 5.2.6) can be obtained by wrapping the outside of the oven in a heater tape controlled by a variac which heats the oven to its working temperature of about 50°C. At this temperature the caesium vapour pressure is about 10^{-5}torr [47]. The oven temperature is measured by a thermocouple set into the wall of the oven.

The vacuum system is shown schematically in figure 5.7. The vacuum was provided by an oil vapour diffusion pump (Edwards EO2 series 'C') backed by a rotary pump. After baking at 100°C for a few hours while pumping, a high vacuum of about 10^{-8}torr, as measured on an ionisation gauge (Edwards ION7), could be achieved. For maintenance purposes (see section 5.1.4), the oven could be removed from the vacuum system without itself or the remainder of the vacuum system being exposed to air by shutting the two valves at either end of the bellows. During an experimental run (see section 5.3.2), it was necessary to leak noble gas (99.99+% pure) slowly into the system and then slowly remove it. Noble gas pressures near the oven in the range 0.001 to 1.1 torr were measured by a Chell baratron MKS manometer. The baratron's analogue voltage output, which is linearly related to pressure, is monitored by the microlink.

5.1.4 Maintenance of the caesium oven

During operation, the windows of the oven gradually became fogged due to a deposition accumulating on the inside. This deposit was not pure caesium since it could not be removed by the application of heat. Its exact chemical composition is not known. The baffles increase the working life of the windows by reducing the number of possible straight line paths to the windows from the liquid caesium in the bottom of the oven. Nevertheless after several hours of oven operation, it was necessary to change the windows. In order to change the windows the oven was removed from the vacuum system and placed in a nitrogen atmosphere in an 'Atmos' bag. At the same time more caesium (m.p. 28.5°C and 99.95% pure) could be introduced

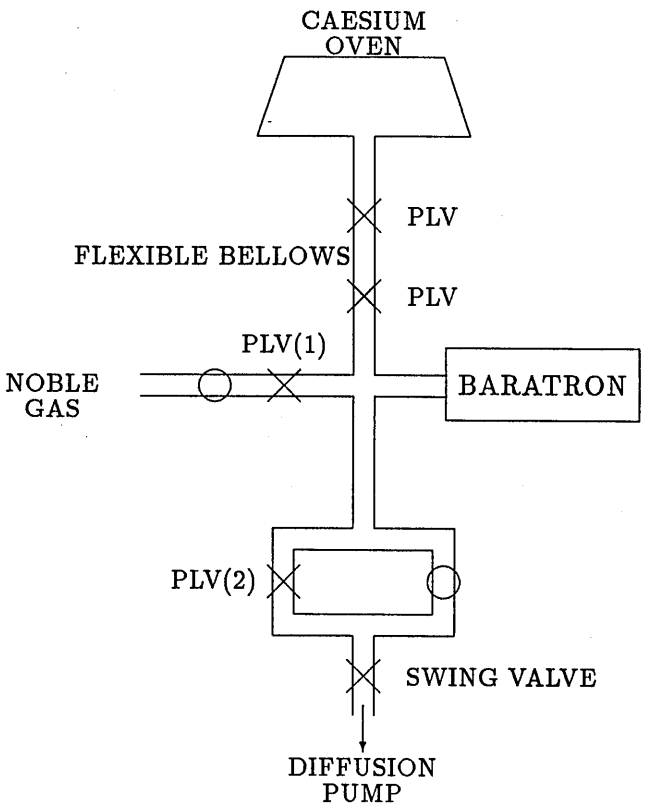

Figure 5.7 Schematic diagram of the vacuum system. Circles represent needle valves and crosses represent open/shut valves (either Edward's Pipe Line Valves or Swing Valve).

into the oven if necessary. Before removing the oven from the 'Atmos' bag, the retaining rings were tightened to ensure that the oven was air-tight. The oven was then reconnected to the vacuum system and pumped down to the working pressure. The retaining rings were then loosened. The removed windows were washed clean in distilled water and, after drying over deliquescent crystals, could be reused.

While the oven was disconnected from the vacuum system, the bellows were exposed to the air and therefore needed to be de-gassed before the valve to the oven was opened. This de-gassing involved heating for a few hours at about 100°C whilst pumping and then cooling whilst still pumping. Whenever any part of the vacuum system or the oven itself was exposed to the air it was similarly treated.

5.1.5 The White cell delay line

The interpulse delay (see figure 5.3) is provided by use of a White cell delay line [93]. The delay line (see figure 5.8) is composed of three concave dielectric coated mirrors each with a radius of curvature of 2.38m and high reflectivity (>99.8% at 455nm). A delay of about 100ns requiring 15 reflections is possible with only about a 3% loss in intensity and little beam degradation. The large mirror, 150mm in diameter, has its centre of curvature between the two smaller mirrors, which are both 50mm in diameter. These small mirrors have their centres of curvature on the face of the large mirror. Hence the mirrors are 2.38m apart. The distance between the centres of curvature of the two small mirrors on the surface of the large mirror determines the number of reflections within the White cell and hence the path length and the interpulse time. Beam divergence is not a problem because the mirrors refocus the beam at each reflection. Minor alterations to the divergence can be effected by adjusting the exact parallelism of the original input beam. For the experimental arrangement used the introduced delay, τ, is given by

$$\tau/\text{nsec} = 15.89 + 15.84l \qquad (l = 1, 3, 5...)$$

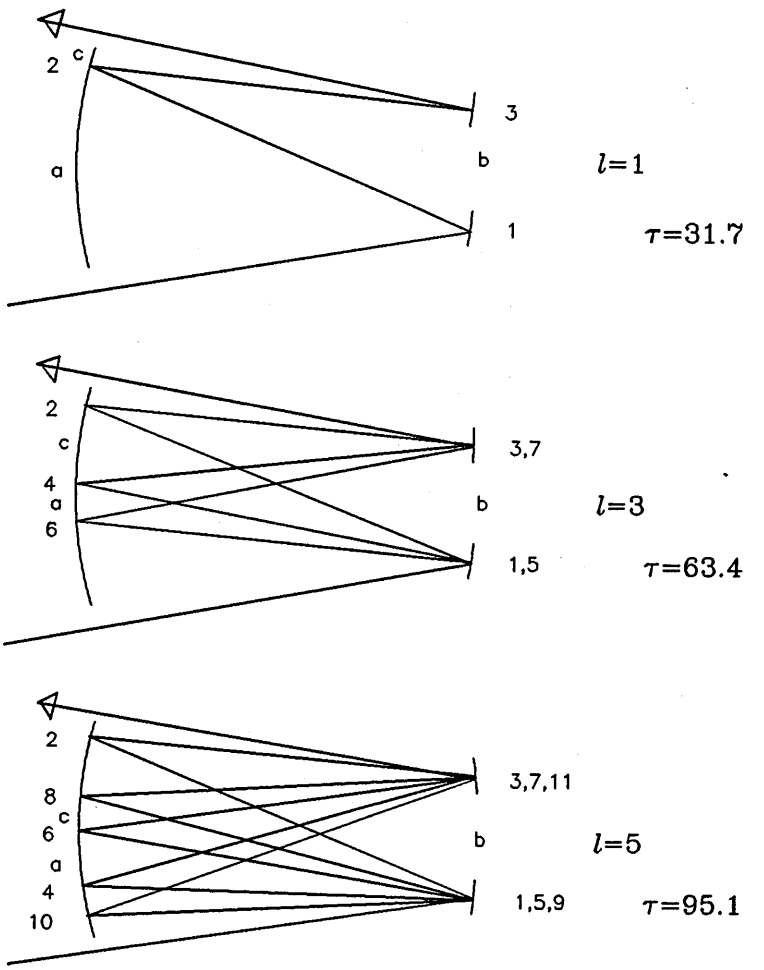

Figure 5.8 White cell delay line illustrating the paths for the first three possible delays: τ is the delay in nanoseconds; l the number of reflections on the large mirror, which has its centre of curvature at b. The numbers refer to consecutive reflections. The small mirror, where the first reflection (1) occurs has its centre of curvature at a and the other small mirror, where the third reflection (3) occurs has its centre of curvature at c. c is moved, by adjusting the angle of this latter mirror, to alter l and hence τ as shown.

where l is the number of reflections on the large mirror. To increase the interpulse time whilst having the exit beam leave the White cell along the same path, l must be increased by two. The interpulse times used in the experiment, in nanoseconds, were

31.7, 63.4, 95.1, 126.8, 158.5 and 190.1

While longer interpulse times are easily obtained using the white cell, the maximum useful interpulse time is limited by the caesium 7P lifetimes of about 120ns. At long interpulse times it is important to keep the optical components free from vibration and other influencies so as to ensure that the beam leaving the White cell follows the same path. In particular, for the experimental arrangement used, this meant diverting the output of the laser cooling fan away from the White cell mirrors.

5.2 Preliminary Experiments

In order to establish suitable operating conditions for the experiment some preliminary measurements were performed.

5.2.1 Linearity

The boxcar output voltage must vary linearly with the mean echo intensity, otherwise systematic errors will be introduced into the measured collisional decay rates. The most likely source of non-linearity is the photomultiplier tube. Non-linearity occurs when photomultiplier tubes have to deliver large currents. This happens at high gains and for intense light pulses. The tube was therefore operated at 0.95kV giving a gain of about 5×10^5, well within the manufacturers recommended maximum voltage of 1.2kV. The linear operating region of the photomultiplier tube was investigated by using the first laser pulse after its passage through crossed polarisers so that its intensity was approximately equal to that of the largest echo signals to be studied. By using neutral density filters in front of the photomultiplier tube a log-log plot was made of boxcar output versus laser pulse intensity over

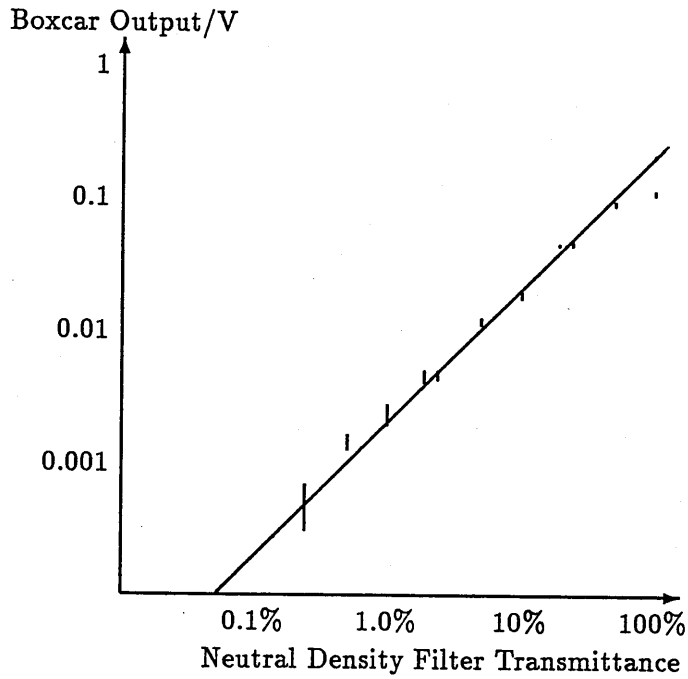

Figure 5.9 Photomultiplier tube (0.95kV) and boxcar response against relative laser pulse intensity.

the range of intensities expected in the echo experiments. The results of this investigation are shown in figure 5.9. The gradient of the plot was measured to be 0.99 ± 0.03, thus giving linearity to within 3%. To ensure that linearity is maintained it was sometimes necessary, when studying large echoes, to reduce the intensity impinging on the photomultiplier tube by using neutral density filters.

5.2.2 Out-gassing

After reasonable efforts had been made to minimise the out-gassing, when the oven and adjacent gas handling system was isolated from the pumps, by closing the swing value (see figure 5.7), the residual out-gassing caused a pressure rise of about 3×10^{-4} torr/min. Therefore the noble gas was introduced during an experimental run at a very much greater rate. In an experimental run (see section 5.3.2 for details), noble gas was let into the

system gradually over a period of two minutes by the suitable setting of a needle valve, up to a maximum pressure of between 0.06 and 0.4 torr. The maximum value depended on the interpulse time, τ, chosen. In the second part of an experimental run the gas was slowly pumped out through a second suitably set needle valve, reaching about 0.015 torr within a further 4 minutes. The pressure of noble gas throughout a run therefore always dominates the out-gassed pressure, by a factor of typically between 100 and 1000 whilst the noble gas pressure is rising. This is necessary to ensure that the measured cross sections are due to collisions with the noble gas under study and not the molecules out-gassed from the walls.

The out-gassing, of course, occurs irrespective of whether the noble gas pressure is rising or falling. Therefore as the total pressure, measured by the baratron, decreases in the second part of an experimental run the out-gassed gases progressively make up a higher proportion. The rejection of any run if its rising and falling relaxation rates differ by more than 5% ensures that out-gassing does not affect the results significantly. Typically the rising and falling relaxation rates are the same to within about 2%.

5.2.3 Faraday rotation

The experimental technique uses an axial magnetic field applied to the sample, which is placed between crossed polarisers. As a result, Faraday rotation of the laser pulses [44] will occur. However, unlike echo polarisation rotation, which occurs between and after the pulses (i.e. in the dark!) during the interval 2τ and is independent of sample length and optical density, Faraday rotation occurs only during the propagation of the pulses through the sample and does depend on oven length and optical density. (Both effects are dependent on magnetic field.) The Faraday rotation can therefore be very small even when the echo-polarisation rotation is large, of order $\pi/2$, which is required for echo detection. In an experimental investigation at 50°C, Faraday rotation on the 459nm line was negligible while on the 455nm line about a 10% increase in intensity of light passing the analyser could be seen at the largest magnetic field that was routinely used (13.5 gauss).

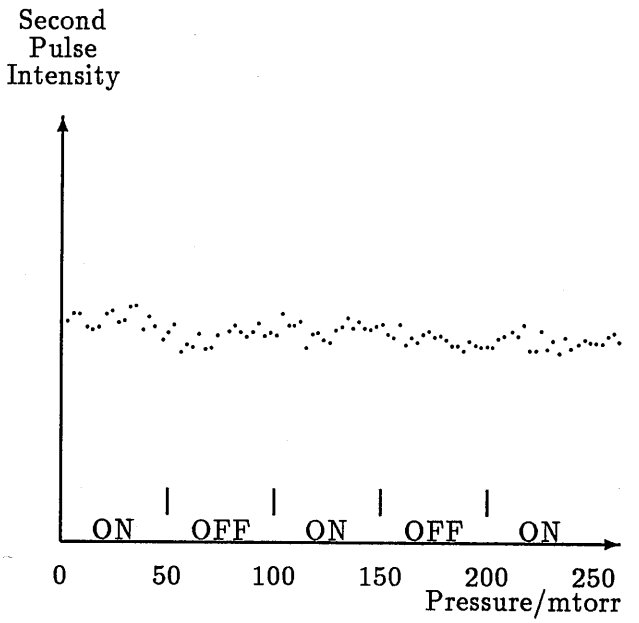

Figure 5.10 Faraday rotation as a function of noble gas pressure. The second pulse intensity was measured as the noble gas pressure rose and the magnetic field was switched off/on every 50 mtorr (being initially on). The slow reduction of the signal with pressure is due to laser drift.

Of more concern than the actual magnitude of the Faraday rotation is a possible dependence of Faraday rotation on noble gas pressure through, for example, collisional redistribution of population. This would produce an additional pressure dependence of the measured echo intensity and therefore a spurious contribution to the measured echo relaxation rate. To test for this, dummy runs were performed monitoring the laser pulse intensity passing the analyser (instead of the echo) while the noble gas pressure was cycled up and down as in the echo experiments and the magnetic field was switched on and off. Such switching was used to avoid misinterpretation of laser drift as evidence of variations in the Faraday rotation. The results showed no evidence of noble gas influence on the Faraday rotation on either the 455nm or 459nm lines (see figure 5.10).

5.2.4 Absorption length

It was necessary to choose a suitable vapour pressure at which to perform the experiments. If the optical density is too low or too high the echo signal is too small to work with. Using an optically thin vapour simplifies the theoretical analysis, since under such conditions the forward emission intensity, I_e, is proportional to the square of the number, n, of contributing atoms. As the number density increases so, initially, does the echo intensity. The echo intensity then peaks and decreases as the vapour becomes optically thick, absorbing the resonant light passing through it. Theoretically, for a non-degenerate two state system [32], the echo intensity peaks when αL equals 1.09, where α is the centre-of-line absorption coefficient and L the effective length of the oven. The largest echo intensity is thus obtained when vapour is no longer optically thin. Figure 5.11 shows a log-log plot of the echo intensity for τ = 31.7ns on the 455nm(F=4) line versus the number density of caesium atoms as calculated from the oven temperature using the saturated vapour pressure data [47]. The initial quadratic rise ($I_e \propto n^2$) is evident (gradient of two) and the peak is between 50°C and 60°C. The compromise temperature chosen for most of the relaxation measurements was 50°C.

5.2.5 Pulse area

The variation of echo intensity, I_e, with the excitation pulse areas, θ_1 and θ_2, for two-excitation-pulse echoes, is given by equation 2.20 and can be expressed as a function of pulse areas by

$$I_e \propto \sin^2\theta_1 \sin^4\frac{\theta_2}{2} \tag{5.1}$$

The optimum pulse sequence is therefore $\pi/2 : \pi$. The beam splitter BS2 (see figure 5.3) divides the laser light 1:4 by intensity which is 1:2 by area as required. It is however difficult to measure the exact pulse area which will vary across the diameter of the beam and from shot to shot of the laser. Furthermore, the characteristics of the second pulse are changed because of its longer path. By placing neutral density filters in the excitation pulse

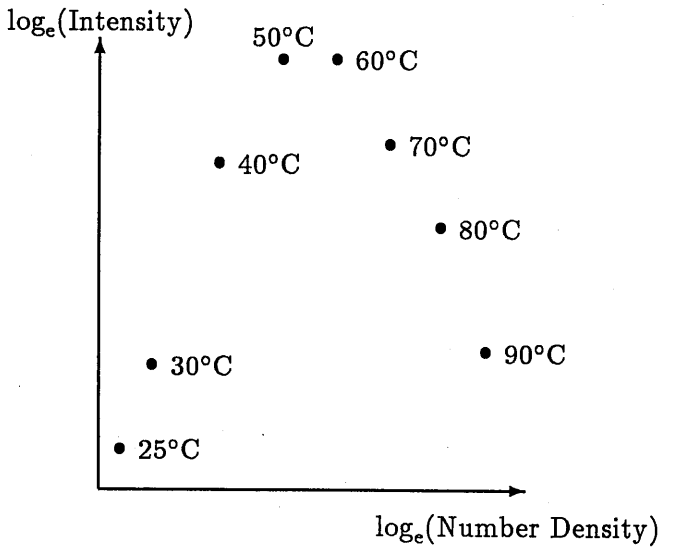

Figure 5.11 Logarithm of echo intensity against logarithm of number density. Points are at 25°C and every 10°C from 30°C to 90°C.

beams plots of average echo intensity against relative excitation pulse intensity were obtained for both the 455 and 459nm lines. The points are plotted in figure 5.12 for $\tau = 31.7$ns at about 50°C and are reproducible to within $\pm$3mV. These plots show that the measured average echo intensity is not simply described by equation 5.1. The discrepancies arise from the various averaging processes. These include the boxcar time average over the shot-to-shot variations, spatial averages over the beam diameter and averages over the caesium hyperfine and Zeeman structure. However from figure 5.12 it can be seen, that to within a few percent, the 100% laser power gives the largest echo signal. The final optimisation is best achieved by adjusting the overlap and diameters of the beams.

5.2.6 Temperature stability

In these experiments it is not necessary to know the absolute value of the caesium vapour pressure. It must however remain constant throughout a run, otherwise changes in the caesium vapour pressure would cause the echo

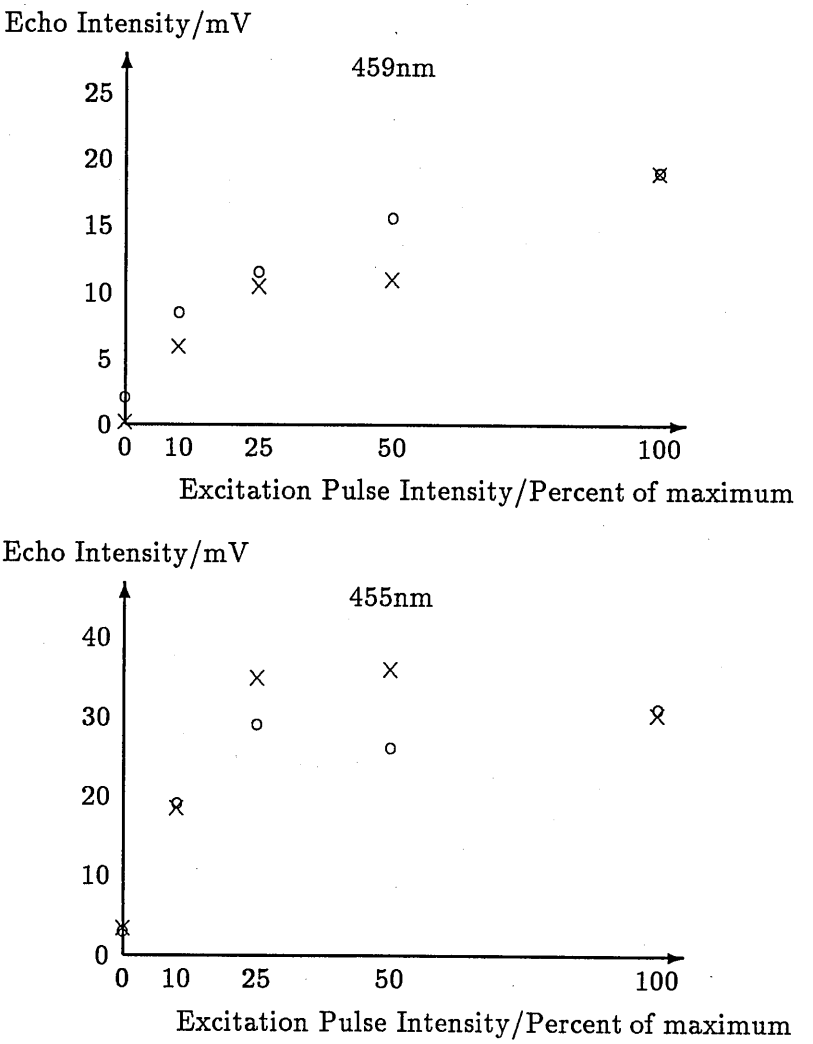

Figure 5.12 Echo intensity against excitation pulse intensity. Circles indicate first pulse and crosses second pulses data.

intensity to change. A value for the temperature of the caesium vapour, T, is obtained by using a thermocouple set in the oven wall. The temperature remains constant to within about a tenth of a degree over the period of many experimental runs. Furthermore, the temperature over the length of the oven differs by less than 2°C. This was established by measuring the temperature at a number of positions on the oven with calibrated thermocouples.

5.2.7 Uncertainty in echo time

It can be seen from equation 4.8 that in order to calculate the effective collisional cross section, $\sigma(\tau)$, from the measured relaxation rate, $\beta(\tau)$, the time which elapses between the first pulse and the time at which the echo is formed must be accurately known, since it is during this time that collisions give rise to the reduction in echo intensity. The theoretical analysis of chapter 2 showed that the echo is formed at a time 2τ after the first pulse. This analysis assumed negligible excitation pulse lengths. When the effects of finite pulse lengths are included [1, 24, 83] it is found that the echo can be formed at times different from 2τ by amounts of order of the pulse duration. However, the actual time between the first pulse and the echo can be measured to within about 3ns by observing the pulse sequence on an oscilloscope. The interpulse time, τ, can be calculated more precisely by measuring the path difference on the optical table and dividing by the speed of light. Measuring the distance between mirrors to an accuracy of 5mm gives the interpulse time to an accuracy of about 0.2% for all six delays. Table 5.1 shows that the values of 2τ so calculated are consistent with the observed echo time on the oscilloscope.

Taking an uncertainty in echo time of half an excitation pulse width (3.5ns) gives an error of 5% for the smallest interpulse time and linearly decreasing errors for the larger interpulse times.

l	Time/ns		
	2τ As calculated from optical path length	As observed on the oscilloscope	
		459nm	455nm
1	63.4 ± 0.1	64 ± 2	65 ± 2
3	126.8 ± 0.3	128 ± 2	128 ± 2
5	190.2 ± 0.4	192 ± 2	196 ± 2
7	253.6 ± 0.5	255 ± 5	255 ± 5
9	317.0 ± 0.6	320 ± 5	315 ± 5
11	380.4 ± 0.8	380 ± 5	382 ± 5

Table 5.1 Comparison between twice the interpulse time and the time at which the echo is formed on the 459 and 455nm lines.

5.3 Experimental Method

The apparatus described above in section 5.1 was used to measure the decay of the optical echo intensity with increasing noble gas pressure, from which collision cross sections can be deduced. In this section the experimental method is described. In section 5.3.1 the initial setting up procedure is described. Then in section 5.3.2 the procedures of an experimental run are given. Finally in section 5.3.3 the various techniques of the data analysis are described.

5.3.1 Setting up the experiment

The relevant cylinder of noble gas (99.99+% pure) was connected to the vacuum system and the caesium oven flushed clean of the previous gas. The oven stabilised at its working temperature of about 50°C to within ±0.1°C within half an hour of switching on and maintained this stability over the period of several experimental runs. At 50°C the vapour pressure of caesium is about 10^{-5}torr [47], which for a 100mm long oven gives a value of αL of about unity for the 455nm line (see section 5.2.4). As mentioned before, α is the centre-of-line absorption coefficient and L is the length of active vapour. The nitrogen laser repetition rate was set to about 30Hz. The transition

to be studied ($6S_{1/2}$–$7P_{1/2}$, 459nm or $6S_{1/2}$–$7P_{3/2}$, 455nm) was selected by tuning the dye laser cavity diffraction grating. The ground state hyperfine level (F=3 or 4) was selected by adjusting the dye laser intra-cavity etalon while watching for blue fluorescence from caesium vapour contained in a heated sealed glass cell which was temporarily placed in the laser beam. Most work was done using the F=4 ground state component. A value for the delay time was chosen by adjusting the number of reflections within the White Cell (see section 5.3). The other optics and the boxcar gate were adjusted to optimise the echo signal. A working value for the axial magnetic field was determined by carrying out a preliminary experiment measuring the averaged echo intensity as a function of the magnetic field. An example of the echo polarisation beat curve thus obtained is shown in figure 5.19. From such curves, a fixed value for the magnetic field was chosen for the echo relaxation measurements for each value of the interpulse delay, τ. Usually the chosen value was that corresponding to the first maximum on the beat curve. Having satisfactorily established the above experimental parameters, investigation of the pressure dependence of the echo intensity could begin.

5.3.2 An experimental run

An experimental run consisted of recording the averaged echo intensity as the noble gas pressure was first increased to a maximum then decreased again. Values of the noble gas pressure (as measured by the baratron) and the averaged echo intensity (the boxcar output) were collected by the microlink and stored by the microcomputer. The first pulse was simultaneously monitored to give a record of laser stability. In order to reduce the problems caused by out-gassing (see section 5.2.2) and by laser instability (especially its tendency to drift away from resonance) the experimental run was completed in about six minutes. Since the echo intensity falls more rapidly with pressure for the longer interpulse times, it was necessary to alter the rate at which the noble gas entered the vacuum system for different interpulse times. Thus, between 0.06 and 0.4 torr of noble gas was let into the system

over a two minute period by the suitable setting of the needle valve near the noble gas cylinder (see figure 5.7).

To start an experimental run the swing valve just above the diffusion pump was shut with all the pipeline valves open. The needle valve, adjacent to pipeline valve PLV(1) (see figure 5.7), had been previously set to allow the noble gas to leak into the oven at a predetermined rate. When the noble gas pressure reached a pre-set maximum value the microcomputer bleeped to inform the operator (see Appendix C.1). This pre-set value had been previously determined to give a drop in echo intensity by a factor of approximately e^5. The final stage of the experimental run involved recording the echo intensity as the noble gas pressure slowly decreased. This slow pressure decrease was obtained by a reconfiguration of the vacuum system valves (see figure 5.7). The noble gas supply was isolated by closing the pipeline valve(1). Then the pipeline valve(2), in parallel with the other needle valve, was shut and finally the swing valve was opened. The gas in the vacuum system, and therefore that in the oven, was slowly pumped away through this latter needle valve. A suitable setting of this needle valve allowed the pressure to reduce to about 0.015 torr within a further 4 minutes.

The recorded averaged echo intensity versus noble gas pressure obtained from each experimental run forms two approximately exponential curves, one for increasing pressure and one for decreasing pressure. Examples can be seen in figures 5.13a, b and c. From such curves the echo relaxation rate, β, was calculated as described in section 5.3.3. The collisional relaxation of echoes is assumed to be an exponential function of pressure (equation 4.6). However, the rising pressure data shows distinct non-exponential behaviour at low pressure (see figures 5.13a, b and c). This flattened top at the start of a run is mainly due to instrumental time constant effects. Appendix B shows that only the initial portion of the curve is non-exponential. Therefore by simply ignoring this portion of the data the relaxation rate, independent of instrumental effects, can be obtained. This initial portion can be determined by performing a run in which only the instrumental time constant effects are present. Such runs were performed experimentally by blocking the first pulse

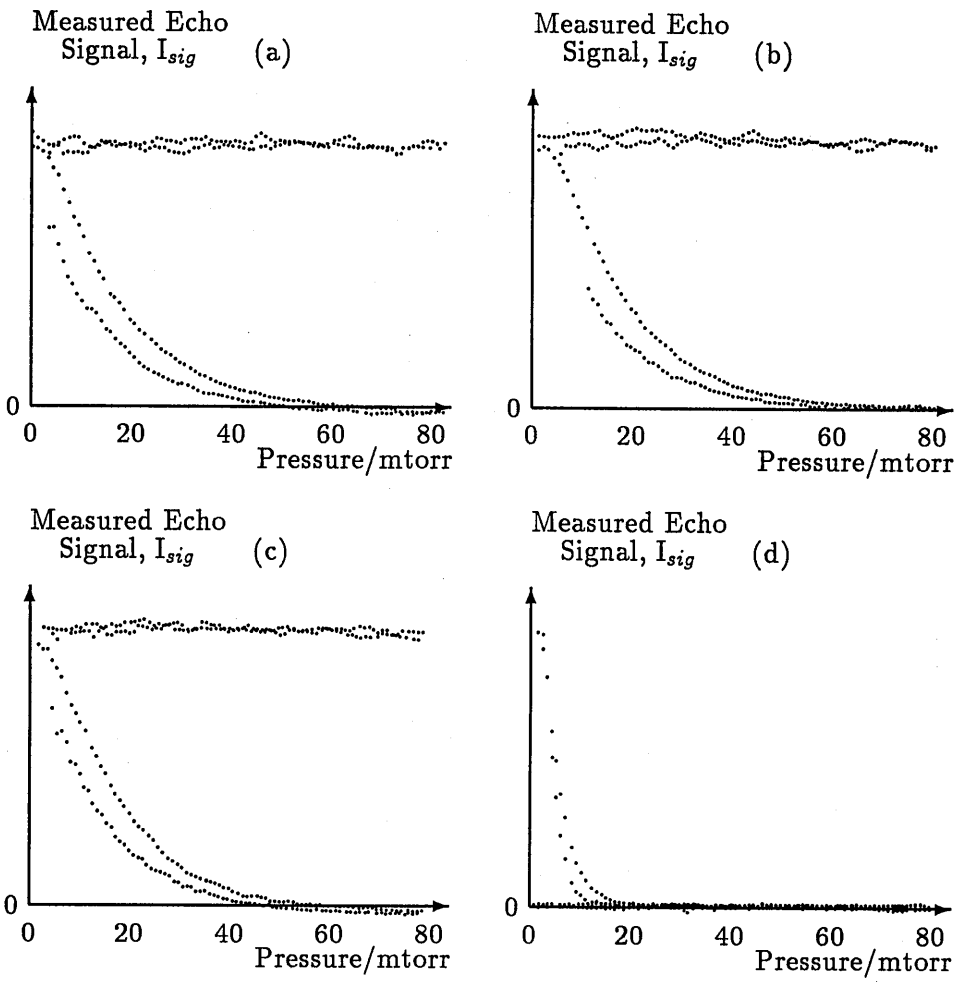

Figure 5.13 Typical data (455nm(F=4) τ=126.1ns Argon Perturber). Curves (a),(b) and (c) show the approximately exponential decay of echo intensity with noble gas pressure. The lower of each pair of curves is the falling pressure data. The monitored first pulse intensity is also shown, this is the approximately horizontal line. Curve (d) was obtained by blocking the first pulse as the pressure rise was commenced. This curve contains information about instrumental time constants.

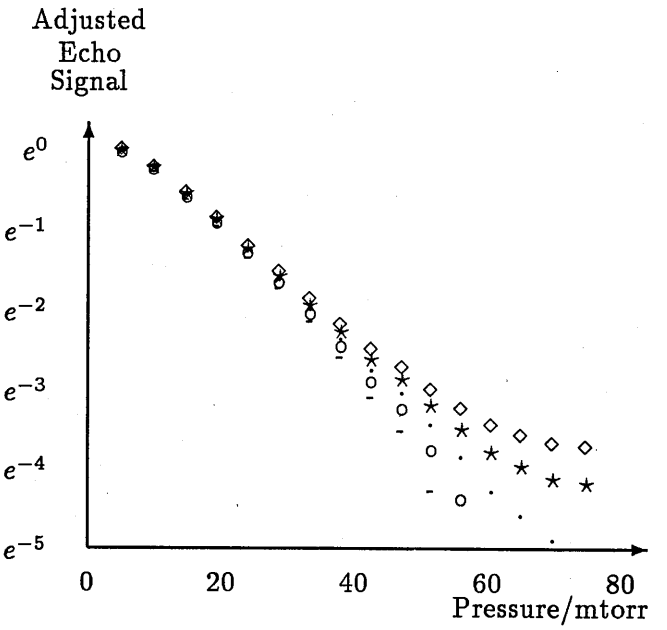

Figure 5.14 Logarithm of adjusted echo signal against pressure illustrating the problem of uncertainty in the intensity base line. The data are the rising pressure data of figure 5.13a. The graphs are plotted each assuming a different value of A (see equation 5.2). The values chosen are a small percentage of the initial intensity ($\diamond$: 1%; $\star$: 2%; . 3%; o: 4%; -: 5%).

just as the pressure rise was started. The echo immediately disappeared. However, the boxcar output, corresponding to the averaged echo intensity, decayed away at a rate determined by the instrumental time constant. An example of such a run is shown in figure 5.13d and indicates that the first 9 mtorr of the corresponding normal runs, at this interpulse time, should be ignored. This is consistent with the prediction of the theoretical model of time constant effects given in Appendix B.

5.3.3 Data analysis

Assuming that the instrumental time constant effects can be compensated for, the measured echo signal is of the form

$$I_{sig} = A + I'_0 e^{-\beta P} \tag{5.2}$$

The constant term, A, is the difference between the zero set on the boxcar (the horizontal axis in figures 5.13) and the actual zero of the measured echo signal (i.e. $I_{sig}(P \rightarrow \infty)$). I'_0 is the true echo signal in the absence of collisions. P is the noble gas pressure and β the pressure relaxation parameter (see equation 4.7). If the constant A were equal to zero then a plot of the natural logarithm of I_{sig} against P would be a straight line with gradient $-\beta$. However, if A is non-zero then the plot of the natural logarithm of I_{sig} against P will be non-linear. Plotting $\log_e(I_{sig} - A)$ against P will always be a straight line. Therefore the value of A needs to be estimated. This can best be done from the curves of the type shown in figure 5.13. This is illustrated in figure 5.14 which shows the data of figure 5.13a plotted for five assumed values of A. Evidently the true value of A corresponds to the points shown by dots (.) in figure 5.14. The other points in figure 5.14 assume values of A which differ by a few percent of $I_{sig}(P = 0)$. The reason for collecting the data out to high pressures where the echo signal is very small (about e^{-5} of its initial value) is now clear. The curving of the logarithmic plots at high pressure becomes a very sensitive indicator of the wrong choice of A. If the data collection is truncated at the lower values of P the logarithmic plots can appear to give straight lines, with different gradients, for a range of assumed values of A. For example, if the data of figure 5.14 was truncated to e^{-4} of its initial value then only the upper plot ($\diamond$) would be seen to curve. The other four plots would appear to be straight lines but with gradients up to 15% from the true value.

A set of at least 11 runs was obtained for each value of the magnetic field, B, and interpulse time, τ, chosen. The standard deviation of the 22 or more values (two per run i.e. rising and falling gradients) of β measured was usually between $\pm 2\%$ and $\pm 3\%$ of the mean. The values of β are related to the effective collisional cross section, $\sigma(\tau)$, by equation 4.8. The effective collisional cross sections are shown in figures 5.15 and 5.16 on pages 94 and 95 and will be discussed in the next section.

5.4 Presentation and Discussion of Results

The results, in the form of effective collisional cross sections, $\sigma(\tau)$, against interpulse time, τ, are shown graphically in figures 5.15 and 5.16. Each point on these graphs is the average of the results of some eleven experimental runs. The error bars on these graphs show only the statistical standard deviations from experimental run to run, this deviation is about 4%. In agreement with similar work on other metal vapours [35, 50, 52], which has been discussed in section 4.4, the effective collisional cross section for caesium-noble gas collisions, $\sigma(\tau)$, is found to increase with interpulse time, τ, although in the case of the present experiments the observed increase is only just significant over the range of interpulse times studied.

Attributing this increase to the effects of diffractive velocity changing collisions, an initial quadratic rise of effective collisional cross section, $\sigma(\tau)$, with interpulse time is expected (see equation 4.13 on page 63). Thus, for small τ, the graphs of $\sigma(\tau)$ against τ^2 should be straight lines. The experimental data of figures 5.15 and 5.16 are replotted in figures 5.17 and 5.18 with τ^2 as the abscissa. Computer least squares fits [87] were used to obtain values for the gradient and ordinate intercept of the best straight lines. The points were weighted to reflect the fractional uncertainty in the interpulse time, due to the laser pulse duration. This fractional uncertainty decreases linearly as the interpulse time is increased. The scatter of the data points about the best straight lines was taken to reflect the random error. The interpretation of the effective collisional cross section is discussed in detail in section 4.3. Figures 5.17 and 5.18 are now analysed using this interpretation. From equation 4.13 on page 63 the ordinate ($\tau^2 = 0$) intercept of the best straight line gives the phase interrupting collisional cross section, σ_{pic}, which is related to the traditionally measured broadening constant, γ, by equation 4.16 on page 63. From the gradient of the best straight line and the above value of σ_{pic}, equation 4.15 on page 63 gives the velocity changing collisional cross section, σ_{vcc}. The average velocity change, δu, following a diffractive velocity changing collision can be calculated from equation 4.14 on page 63 using the values of σ_{pic} and σ_{vcc}. The determined values of σ_{pic},

σ_{vcc}, δu and γ are shown in table 5.2.

		σ_{pic} / Å^2	σ_{vcc} / Å^2	δu / ms^{-1}	γ / cm^2
459nm $6S_{1/2}$-$7P_{1/2}$	Xe	1436 ± 19	328 ± 211	$0.59 \pm .04$	$2.50 \pm .06$
	Ar	1123 ± 6	229 ± 47	$0.68 \pm .01$	$2.86 \pm .04$
	He	556 ± 2	143 ± 8	$0.95 \pm .06$	$3.98 \pm .05$
455nm $6S_{1/2}$-$7P_{3/2}$	Xe	1328 ± 6	442 ± 75	$0.57 \pm .01$	$2.31 \pm .03$
	Ar	997 ± 9	500 ± 105	$0.65 \pm .02$	$2.54 \pm .04$
	He	415 ± 7	80 ± 21	$1.12 \pm .02$	$2.97 \pm .08$

Table 5.2 Collision cross sections and diffractive velocity changes for caesium($6S_{1/2}$-$7P_{1/2}$, $7P_{3/2}$)–noble gas collisions at 323K. The broadening constant calculated from these values is shown adjusted to 400K for comparison with table 1.1.

This thesis describes the first major application of the polarisation rotation technique to the measurement of collisional relaxation rates. Tests for systematic effects are the subject of the next section of this chapter.

5.5 Possible Systematic Effects

Although polarisation rotation is a simple technique to use to discriminate in favour of echoes, there are two major concerns that arise when it is used to measure relaxation rates. These are associated with echo intensity beating effects (see chapter 3) and propagation effects.

The intensity beats result from interference between echo contributions formed on the coherently excited hyperfine levels and Zeeman sub-levels of the 7P excited state as well as the Zeeman sub-levels of the ground state. This is described in section 3.3. If different echo contributions have different pressure relaxation rates then the calculated cross sections would depend on the relative contributions. The relative contributions depend on the inter-pulse time, τ, and the axial magnetic field, B. For the case of the caesium 6S-7P transitions, the theory of collisional relaxation of echoes [3, 91] predicts that the relaxation rate is independent of the Zeeman and hyperfine structure contribution. In order to confirm this some experiments were

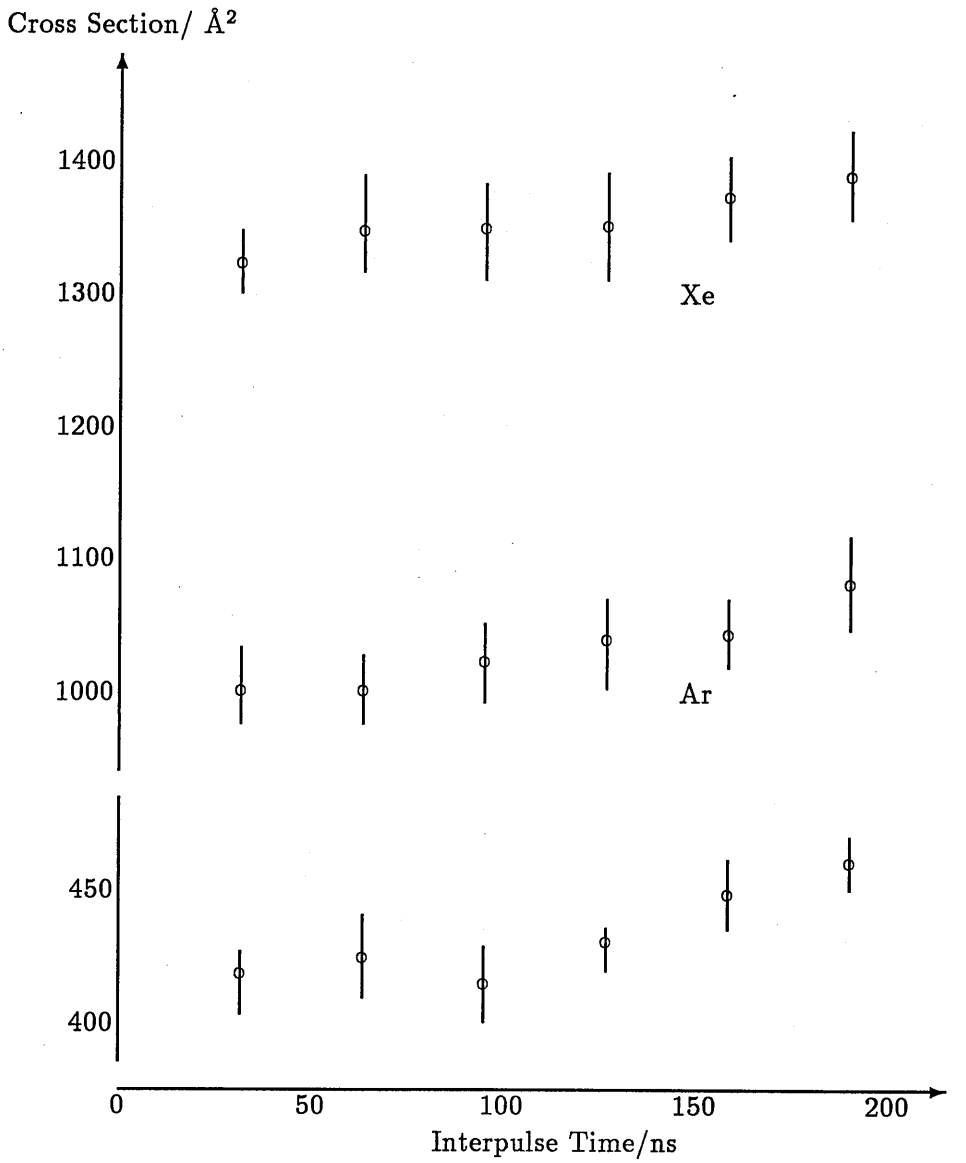

Figure 5.15 Effective collisional cross section, $\sigma(\tau)$, against interpulse time for the $6S_{1/2}$-$7P_{3/2}$ transition of caesium (455nm) for helium, argon and xenon gases. The error bars indicate the standard deviations of data obtained in 11 or more runs per experimental point.

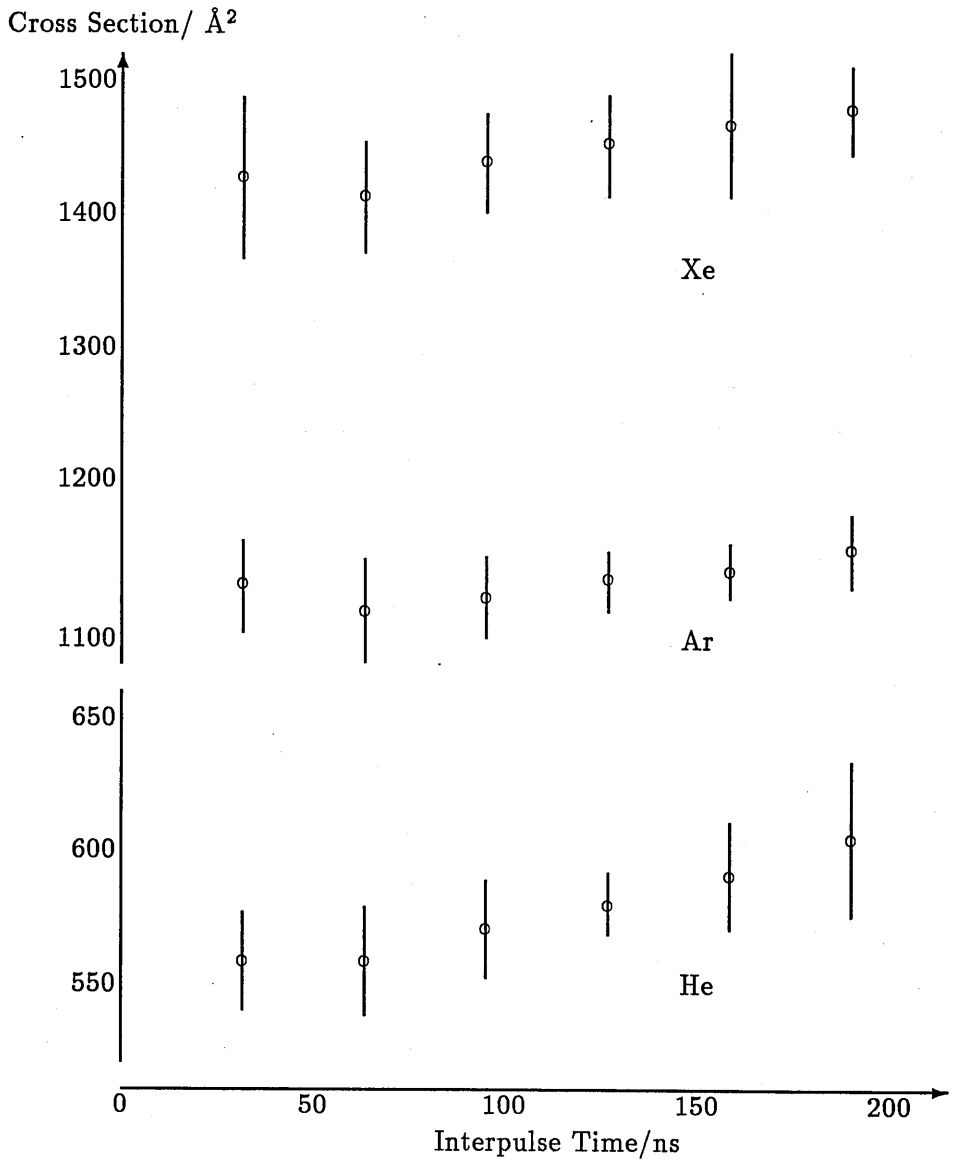

Figure 5.16 Effective collisional cross section, $\sigma(\tau)$, against interpulse time for the $6S_{1/2}$-$7P_{1/2}$ transition of caesium (459nm) for helium, argon and xenon gases. The error bars indicate the standard deviations of data obtained in 11 or more runs per experimental point.

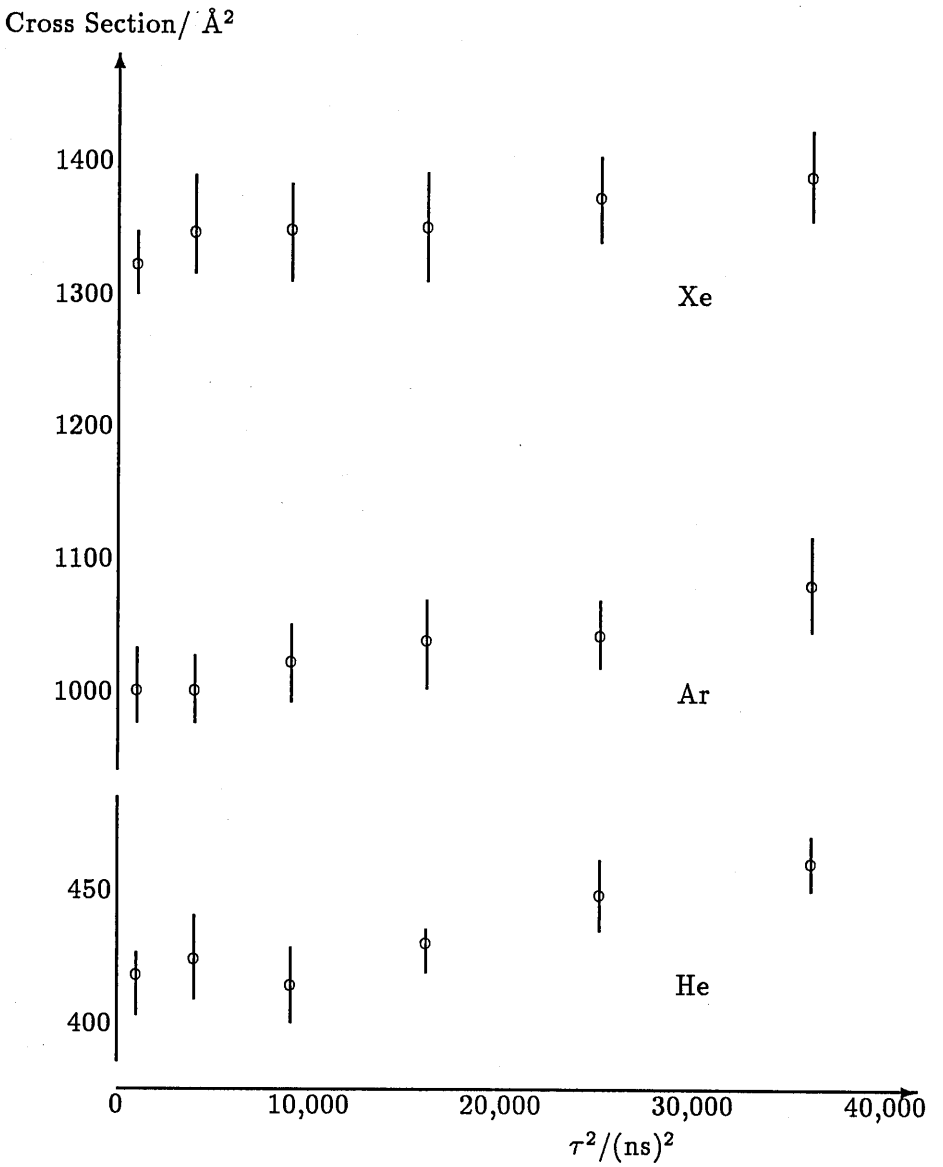

Figure 5.17 Effective cross section, $\sigma(\tau)$, against interpulse time squared for the $6S_{1/2}$-$7P_{3/2}$ transition of caesium (455nm) for helium, argon and xenon. The error bars indicate the standard deviations of data obtained in 11 or more runs per experimental point.

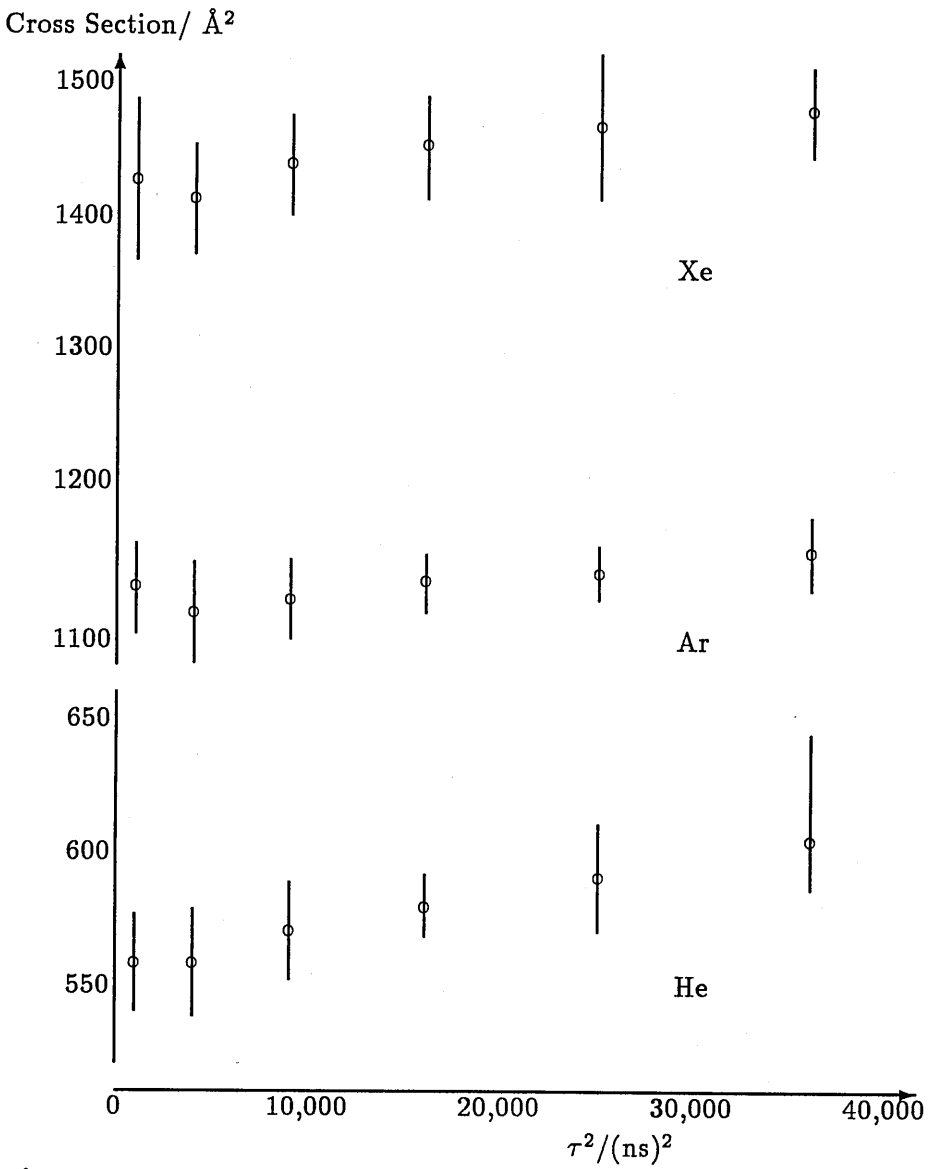

Figure 5.18 Effective cross section, $\sigma(\tau)$, against interpulse time squared for the $6S_{1/2}$-$7P_{1/2}$ transition of caesium (459nm) for helium, argon and xenon. The error bars indicate the standard deviations of data obtained in 11 or more runs per experimental point.

performed where the relaxation measurements were repeated at different positions on the echo intensity beat curve, that is, for different values of interpulse time, τ, and axial magnetic field, B, (see sections 5.5.1 and 5.5.2 respectively).

If the propagation effects were dependent on noble gas pressure then the measured echo signal would not have the simple exponential relationship to the noble gas pressure that was predicted in chapter 4 (see equation 4.7 on page 54) and the calculated cross sections would be in error. These propagation effects might depend on axial magnetic field, B, as well as caesium number density or temperature, T.

The above mentioned beating and propagation effects depend on one or more of the experimentally controlled parameters τ, B and T. The strategy for the investigation was therefore to vary each of these parameters independently and to observe the effect, if any, on the calculated cross section.

Section 5.5.1 describes measurements taken with the interpulse time, τ, varied on the time scale of the reciprocal of the hyperfine structure splitting (of order a nanosecond). Section 5.5.2 describes the measurements taken at different values of the axial magnetic field, B. Section 5.5.3 describes measurements taken at different caesium vapour number densities by varying the temperature, T, of the oven. Finally, in section 5.5.4 the results of preliminary work on stimulated echoes are compared with the two-excitation-pulse echo results. Stimulated echo experiments do not require an applied magnetic field.

5.5.1 Small alterations in interpulse time

In the case of the 459nm line ($6S_{1/2}$-$7P_{1/2}$) the hyperfine splitting of the $7P_{1/2}$ state is 400MHz, giving a beat period of 2.5ns. Variation of the interpulse time on this time scale varies the relative contributions of the hyperfine levels to the echo signal.

In order to confirm the prediction that all the hyperfine levels relax at the same rate the echo relaxation measurements were repeated on the $6S_{1/2}$-$7P_{1/2}$ transition using interpulse times that were longer by approximately

Axial Magnetic Fields/G	Collision Cross Section/Å^2
5.1	1130± 30
6.0	1136± 30
12.8	1132± 40
19.5	1125± 30
27.6	1120± 40

Table 5.3 Effective cross sections, $\sigma(\tau)$, at a variety of axial magnetic fields (459nm,F=4,τ=95.1ns Argon).

half of the $7P_{1/2}$ hyperfine beat period ($1\frac{1}{4}$ns). Figure 5.21 on page 104 shows that to within experimental error the effective collisional cross sections calculated from these measured relaxation rates ($\oplus$) lay on the same monotonically increasing curve as the effective collisional cross sections determined from measurements made at the standard, slightly shorter, interpulse times (o).

5.5.2 Magnetic field effects

To establish the manner, if any, in which the measured collisional relaxation rate depended on the value of the magnetic field, the pressure induced relaxation rate at a particular interpulse time was remeasured at an additional four magnetic field values. These were chosen to be near the maxima of the echo intensity against magnetic field curve and are shown in figure 5.19. For a given interpulse time the routinely used magnetic field was that of the first maximum of the appropriate echo intensity against magnetic field curve.

The four additional magnetic field measurements are indicated in figure 5.21 by the arrows ($\rightarrow$) and show that to within the experimental error there is no magnetic field dependence of the collisional cross section. The values are also given in table 5.3. This null result also shows that any magnetic field dependent propagation effects do not affect the results.

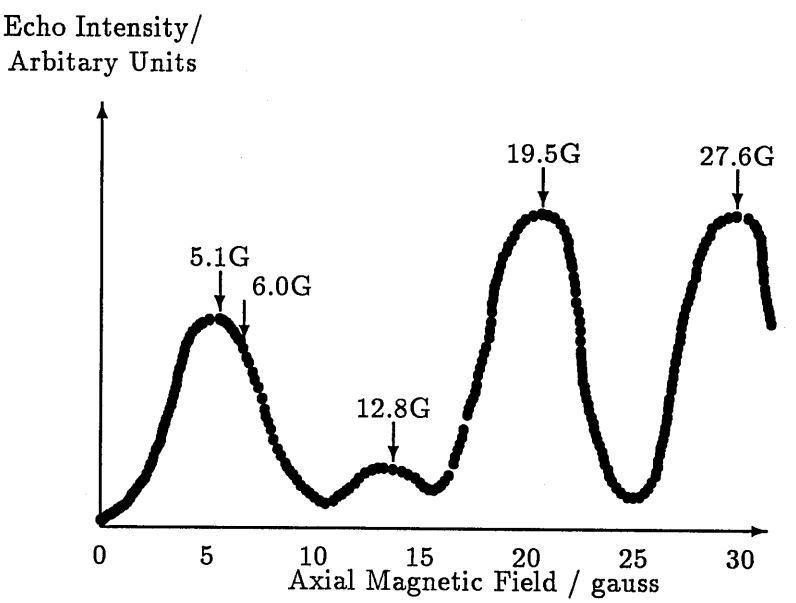

Figure 5.19 Echo Intensity (459nm,F=4,τ = 95.1ns) against magnetic field.

5.5.3 Temperature effects

To determine whether or not intensity dependent propagation effects are important, the relaxation rates were measured at different optical densities. These were most easily obtained by varying the caesium vapour temperature, T, since the optical density varies considerably for temperature changes over which the cross section hardly changes.

Most of the relaxation measurements were performed at about 50°C, however, some measurements were repeated at about 40°C and 60°C (see figure 5.21 points shown by $\bigtriangledown$ and $\bigtriangleup$ respectively). The effective cross section, $\sigma(\tau)$, is expected to vary very slowly with temperature. If a van der Waals interaction is assumed then the collisional cross section will have a $T^{-0.2}$ temperature variation. Thus the cross section measured at 40°C should be only about 1% larger than that measured at 60°C. Such a variation will be unobservable due to the experimental error. However the caesium vapour pressure varies by a factor of about 5 over this range [47]. The measured cross sections show no significant temperature variation indicating that propagation effects do not affect the results.

5.5.4 Comparison with stimulated echo experiments

Further evidence to support the conclusion that the measured effective collisional cross section does not depend on the applied magnetic field comes from some preliminary stimulated echo experiments where no axial magnetic field is applied. In these experiments the three excitation pulse stimulated echo was used to measure the noble gas induced collisional relaxation rates of the caesium 6S-7P transitions. The optical arrangement was similar to that used by Fujita et al for sodium [37] where the echo propagates in nearly the opposite direction to the first two pulses and at an angle of some 20mrad from the third with orthogonal polarisation. With the second and third pulses occurring almost at the same time the measured relaxation rates should be identical to those measured in two-excitation-pulse echo experiments. The results are shown in figure 5.20($\otimes$) and the agreement between the results is further evidence for the reliability of the echo polarisation

rotation technique. Stimulated echoes are further discussed in section 6.2.

5.6 Comparison with Previous Results

Echo relaxation measurements of broadening constants have many advantages over spectral line profile measurements. They do not suffer from the effects of transit time broadening [23], Doppler broadening, laser power broadening or optical pumping. The uncertainty in the interpulse time, τ, which limits the precision of experiments in the nanosecond regime is not a fundamental limitation of the technique (nor is it a major source of error in the work of chapter 5) and it could be significantly reduced by the use of pico-second laser pulses which can now be generated. A further advantage of echo techniques is that they can be used to study the effects of diffractive velocity changing collisions which cannot be observed by traditional techniques.

In section 5.6.1 the measurements of phase interrupting collisional cross sections by both echo relaxation and traditional spectral line profile techniques are compared. The measurements considered are for certain electric dipole allowed transitions of lithium, sodium and ytterbium as well as of caesium. Only helium, argon and xenon perturber gases are considered. In section 5.6.2 the general trends concerning the diffractive velocity changing collisional cross sections, and the associated average magnitudes of the velocity changes, obtained from the experimental results of this thesis are compared with the results of previous experiments on lithium and ytterbium.

5.6.1 Echo relaxation and spectral line broadening results

The phase interrupting collisional cross sections, σ_{pic}, for caesium determined by traditional spectral line profile studies are consistantly larger than those determined by the echo techniques of this work for both the $6S_{1/2}$-$7P_{1/2}$ and $6S_{1/2}$- $7P_{3/2}$ transitions for all perturbers studied. Similar discrepancies exist for the experiments on lithium and sodium. These discrepancies are reviewed below.

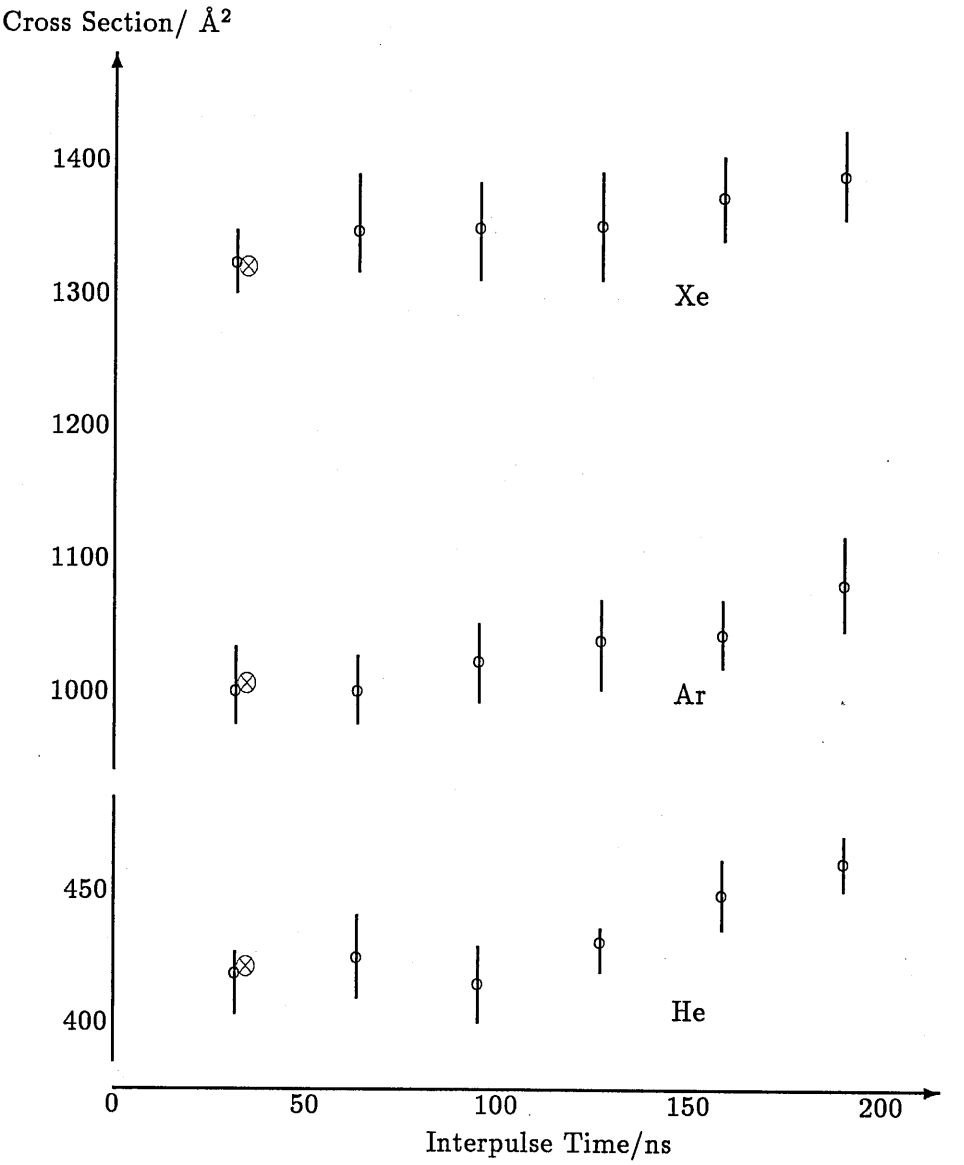

Figure 5.20 Effective collisional cross section, $\sigma(\tau)$, against interpulse time for the $6S_{1/2}$-$7P_{3/2}$ transition of caesium (455nm) for helium, argon and xenon gases. The error bars indicate the standard deviations of data obtained in 11 or more runs per experimental point. The stimulated echo data ($\otimes$) were measured with an effective delay time of 32.5ns (the first point of the standard data is at 31.7ns, the difference is exaggerated in the figure). The stimulated echo work is briefly discussed in sections 5.5.4 and 6.2.

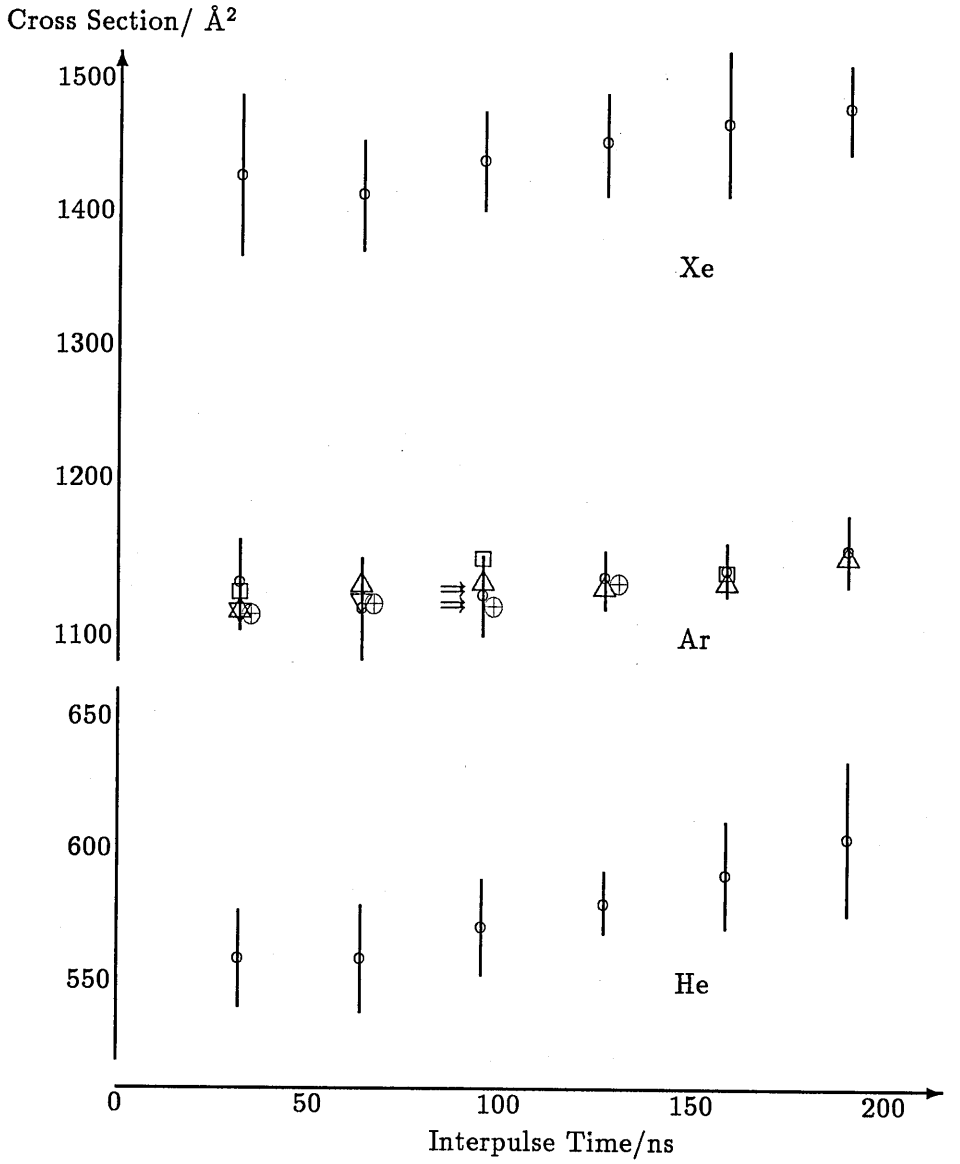

Figure 5.21 Effective collisional cross section, $\sigma(\tau)$, against interpulse time for the $6S_{1/2}$-$7P_{1/2}$ transition of caesium (459nm) for helium, argon and xenon gases. The error bars indicate the standard deviations of data obtained in 11 or more runs per experimental point. Most data (o) was collected under certain standard conditions: 50°C and F=4 ground state. The magnetic field was the first beat maximum for a given delay. As discussed in the text, measurements were repeated with one parameter at a time altered from the standard setting. Such data points were obtained with F=3(□), 40°C(▽) and 60°C(△). The arrowed positions at 95.1ns are measurements at different magnetic fields (from top to bottom these are 6.0,12.8,19.5 and 27.6 gauss). The ⊕ points are with an extra 1.25ns delay (this extra delay is exaggerated in the figure).

Table 5.4 shows the phase interrupting collisional cross sections, σ_{pic}, determined by both two-excitation-pulse echo and traditional line profile techniques for a number of atomic resonance lines perturbed by noble gases. The results presented are for ytterbium $(6s^2)^1S_0$-$(6s6p)^3P_1$ [35] and the D-lines of sodium (3S-3P) [50], lithium (2S-2P) [52] and caesium (6S-7P) [chapter 5]. The alkali metal D-lines are the visible emission lines to the ground state (D_1: $P_{1/2}$-$S_{1/2}$; D_2: $P_{3/2}$-$S_{1/2}$). These results show a number of discrepancies between the echo and line profile measurements. As mentioned above, all the caesium echo results are smaller than the corresponding line profile ones. Also there are discrepancies between the two techniques for the D_1 line of sodium perturbed by both argon and xenon. This is also the case for the lithium D_1 line perturbed by both helium and argon. Other slight discrepancies also exist. In addition, there are discrepancies among the line profile results especially for the D_1 lines of caesium perturbed by xenon and of sodium perturbed by both helium and xenon.

The lithium and sodium echo results have large fractional errors because the measurements were made at interpulse times that were not very much larger than the laser pulse duration. This source of error was discussed in section 5.2.7. Because of these large errors it is common to consider the ratio of the cross sections for the two D lines for a given perturber, which should be independent of this source of error. The errors in the line profile results are, of course, compounded and not reduced by taking such ratios. Table 5.5 shows these ratios for both the echo and line profile results and emphasises the discrepancies between these two techniques for the lithium and sodium results as discussed above. For caesium, the ratios of the line profile results reasonably closely agree with the appropriate ratios of the echo results. This emphasises the fact that the caesium echo results are between about 10% and 20% smaller than the corresponding line profile results. Presumably there exist as yet unappreciated systematic errors in the two techniques that would explain this.

It has been suggested [52] that these discrepancies between the echo and line profile results arise since the echo measurements are performed

		echo	line profile		
^{7}Li	ref.	[52]	[59]		
	temp.	525K			
	^{4}He D_1	102 ± 13	86 ± 3		
	D_2	91 ± 12	86 ± 3		
	^{40}Ar D_1	161 ± 25	164 ± 8		
	D_2	156 ± 24	143 ± 7		
	^{131}XeD_1	221 ± 31	265 ± 10		
	D_2	215 ± 31	227 ± 8		
^{23}Na	ref.	[50]	[18]	[63]	
	temp.	450K			
	^{4}He D_1	1290 ± 80	1300 ± 30	1400 ± 70	
	D_2	1410 ± 90	1590 ± 11	1620 ± 150	
	^{40}Ar D_1	3250 ± 180	4250 ± 30	4230 ± 300	
	D_2	3230 ± 200	3220 ± 80	3470 ± 300	
	^{131}Xe D_1	4400 ± 300	5150 ± 110	4600 ± 400	
	D_2	4500 ± 300	4370 ± 100	4100 ± 400	
^{133}Cs	ref.	[*]	[54]	[78]	[85]
	temp.	323K			
	^{4}He D_1	556 ± 2	-	610 ± 30	-
	D_2	415 ± 7	-	490 ± 30	-
	^{40}Ar D_1	1123 ± 6	-	1320 ± 100	1350 ± 60
	D_2	997 ± 9	-	1160 ± 60	1270 ± 60
	^{131}Xe D_1	1436 ± 19	1630 ± 60	-	1810 ± 120
	D_2	1328 ± 6	1600 ± 300	-	-
^{173}Yb	ref.	[35]	[35]		
	temp.	723K			
	^{4}He	107 ± 16	103 ± 10		
	^{40}Ar	307 ± 31	337 ± 34		
	^{131}Xe	366 ± 37	354 ± 35		

[*] Table 5.2 on page 93

Table 5.4 Phase interrupting collisional cross sections, σ_{pic}, determined by line profile and echo methods. Temperature differences have been compensated for by assuming a van der Waals interaction.

		echo	line profile		
^{7}Li	ref.	[52]	[59]		
	^{4}He	$1.07 \pm .04$	$1.00 \pm .05$		
	^{40}Ar	$1.03 \pm .03$	$1.14 \pm .07$		
	^{131}Xe	$1.01 \pm .04$	$1.17 \pm .05$		
^{23}Na	ref.	[50]	[18]	[63]	
	^{4}He	$0.92 \pm .01$	$0.83 \pm .03$	$0.87 \pm .12$	
	^{40}Ar	$1.00 \pm .01$	$1.32 \pm .04$	$1.22 \pm .19$	
	^{131}Xe	$0.98 \pm .02$	$1.18 \pm .05$	$1.13 \pm .20$	
^{133}Cs	ref.	[*]	[54]	[78]	[85]
	^{4}He	$1.34 \pm .03$	-	$1.25 \pm .13$	-
	^{40}Ar	$1.13 \pm .02$	-	$1.14 \pm .15$	$1.07 \pm .10$
	^{131}Xe	$1.08 \pm .02$	$1.02 \pm .23$	-	-

[*] Table 5.2 on page 93

Table 5.5 Ratios of the phase interrupting collisional cross sections, σ_{pic}, for the D_1 and D_2 lines for alkali metals(Li, Na and Cs) for both echo and line profile measurements. The echo ratios are independent of error in the interpulse time.

on the Doppler-free low pressure line shape in the core region, whilst most line profile measurements are made at substantially higher pressures and in the wings of the spectral line where the impact approximation is beginning to fail as evidenced by the reported asymmetric line shapes [43, 54, 84]. The line core is mainly sensitive to the long range parts of the interatomic potential. The wing measurements correspond to small impact parameter collisions where the form of the potential is not well known and any discrepancies may result in a non Lorentzian profile. Echo measurements would therefore be expected to agree with line profile measurements when the latter are performed strictly in the impact regime. Biraben et al [11] used two photon spectroscopy (see section 1.2.1(ii)) to obtain Doppler free line profile measurements of electric dipole forbidden transitions of sodium broadened by noble gases. These line core results are in agreement with the corresponding tri-level echo work of Flusberg et al [31]. However, the errors in both experiments are about 10%. In the case of ytterbium [35] echo relaxation and Doppler free line profile broadening of an electric dipole allowed transition have been compared. This was the work of Forber et al, who used saturation spectroscopy as well as two-excitation-pulse echoes to compare collisional parameters of the $(6s^2)^1S_0$-$(6s6p)^3P_1$ transition of ytterbium perturbed by noble gases (He, Ar and Xe). But again the experimental errors, at 10%, are relatively large. Kielkopf and Allard [54] measured the broadening constants for many caesium lines perturbed by xenon (see section 1.3). They used a line profile technique which apparently gives high quality line core data. Their work is, however, not in good agreement with the results of table 5.2 nor with the other line profile work on xenon [85]. The experimental situation regarding the measurement of broadening constants is therefore unsatisfactory.

5.6.2 Diffractive velocity changing collisions

To date, only through echo experiments has information on diffractive velocity changing collisions been obtained (see section 4.1). The average magnitudes of diffractive velocity changes, δu, resulting from these collisions

are discussed below. But first the relative magnitudes of the diffractive velocity changing collisional cross sections, σ_{vcc}, and the phase interrupting collisional cross sections, σ_{pic}, are discussed.

From table 5.2, it can be seen that for this work σ_{pic} is about four times larger than σ_{vcc}. This is in contrast with most of the results for the experiments on lithium [52] and ytterbium [35] where σ_{pic} and σ_{vcc} were found to be approximately equal. This is possibly because the lithium and ytterbium experiments involved no change of principle quantum number. Therefore the orbitals of the ground and excited states will be of approximately the same physical size. For the work of this thesis on caesium the excited state is of larger principle quantum number and hence has a larger orbital than that of the ground state. The double hard sphere model [9] predicts

$$\frac{\sigma_{pic}}{\sigma_{vcc}} = (\frac{r_u}{r_l})^2$$

where r_u and r_l are the hard sphere radii associated with scattering from the upper and lower states respectively. Associating these radii with the interatomic potential well minima [76] for caesium(6S-7P)-noble gas collisions gives $\sigma_{pic}/\sigma_{vcc} \sim 4$, which in is reasonable agreement with the experimental results.

In this work on caesium, as only the initial quadratic rise of effective collisional cross section with interpulse time could be obtained experimentally, equation 4.14 on page 63 was used to determine the value for the average magnitude of the diffractive velocity changes, δu. The lithium [52] and ytterbium [35] results were not limited to this initial quadratic regime (see section 4.4) therefore δu and σ_{vcc} as well as σ_{pic} were determined independently. Equation 4.14 shows that for the double hard sphere model δu is inversely proportional to the mass of the active atom, M, and depends only weakly on the total collisional cross section, $(\sigma_{pic} + \sigma_{vcc})$. In agreement with this model the δu for the caesium-noble gas collisions are of about the same magnitude as those for the ytterbium work and are about an order of magnitude smaller than for the lithium experiments.

5.7 Recommended Improvements to the Apparatus

A computer programme has recently been written that averages the data from the eleven or so experimental runs. The implementation of this software will significantly reduce the time required to obtain the relaxation rates from the experimental data. A further software advance would be a computer fitting to the correct semi-log graph gradient. However the algorithm necessary is not a simple least squares fitting because of the need for a floating zero, due to the base line intensity uncertainty (section 5.3.3). Possible algorithms are being sought.

Another area for improvement is the gas handling system. An all glass oven may reduce the problems of window fogging, which are encountered with 'O' ring sealed windows (section 5.1.4). Such an oven may also improve the caesium vapour characteristics, which are reputedly unreliable in metal heat pipe type ovens. The reader is reminded that echo relaxation measurements do not require the active vapour characteristics to be well known (section 5.2.6). It is only necessary that the vapour density remains constant during an experimental run.

Direct monitoring of the caesium vapour pressure would reinforce the indirect checks of its stability that are currently used (see sections 5.2.6 and 5.5.3). Direct monitoring could easily be achieved if a narrow bandwidth laser was used to generate the excitation pulses. If a steady signal from such an excitation pulse was then monitored this would indicate, not only laser stability as is currently the case (section 5.1.2), but also that the laser was tuned to a resonance and that the caesium vapour density was remaining constant.

Chapter 6

Future Echo Work On Caesium

Rydberg states can be conveniently studied by optical echo techniques. These are discussed in section 6.1. Stimulated echoes can be used to investigate the velocity changing effects of collisions on populations as well as on coherences. These are discussed in section 6.2. Electric dipole forbidden transitions can be studied using tri-level echoes. Such a study of the collisional relaxation on the $7P_{1/2}$-$7P_{3/2}$ transition was performed by Manners and Durrant in 1986 [64].

6.1 Rydberg State Echoes

In caesium the P and F Rydberg states can be accessed by optical transitions from the $5D_{5/2}$ level (see figure 6.1). This level has a lifetime of about 1000ns compared with the 120ns lifetime of the $7P_{3/2}$ level and can therefore be populated by decay from the optically excited $7P_{3/2}$ level [62]. The branching ratio is about 10% to the $5D_{5/2}$ level with about 90% to the ground state. In figure 6.1 the relevant energy levels are shown schematically. For such echo experiments involving Rydberg levels two lasers would be required, one tuned to 455nm to populate the $7P_{3/2}$ level and the other to perform the actual echo experiments between the $5D_{5/2}$ level and the P and F Rydberg levels. Alternatively, S and D Rydberg levels could be studied by optical transitions from either of the 6P levels (see figure 6.2). These would need to be populated from the ground state by excitation with

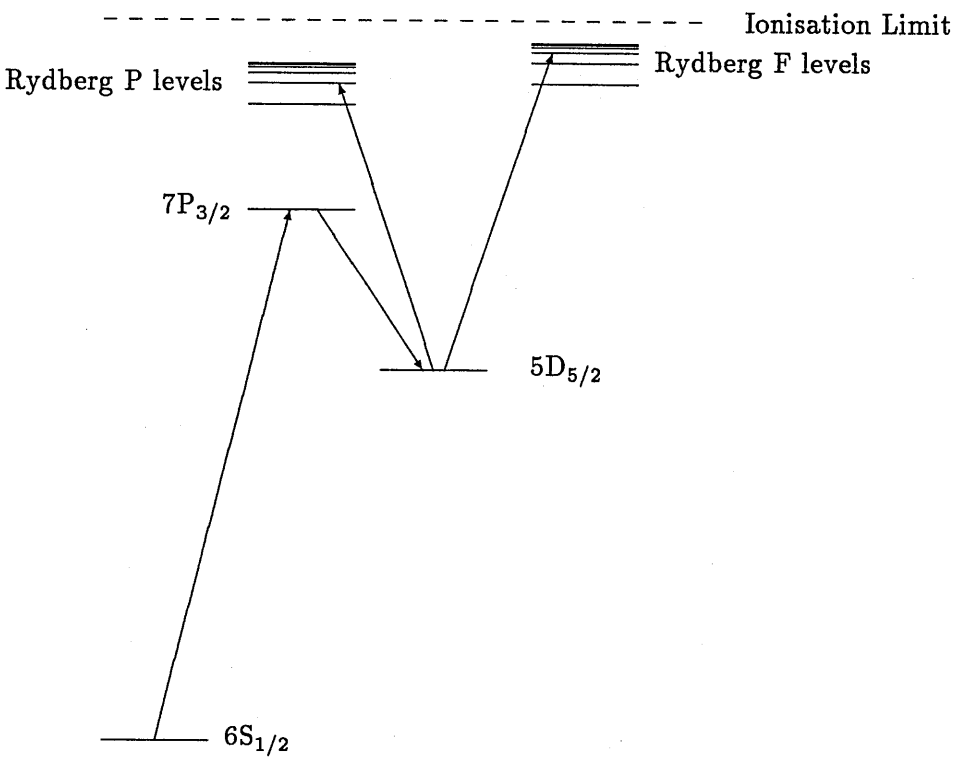

Figure 6.1 Schematic energy level diagram for Caesium, showing the energy levels of interest to the P and F Rydberg level studies. The upward transition to the $7P_{3/2}$ level would be laser induced, spontaneous decay would then populate the $5D_{5/2}$ level. From this level echoes could be generated on optical transitions with Rydberg levels. Two such transitions are indicated.

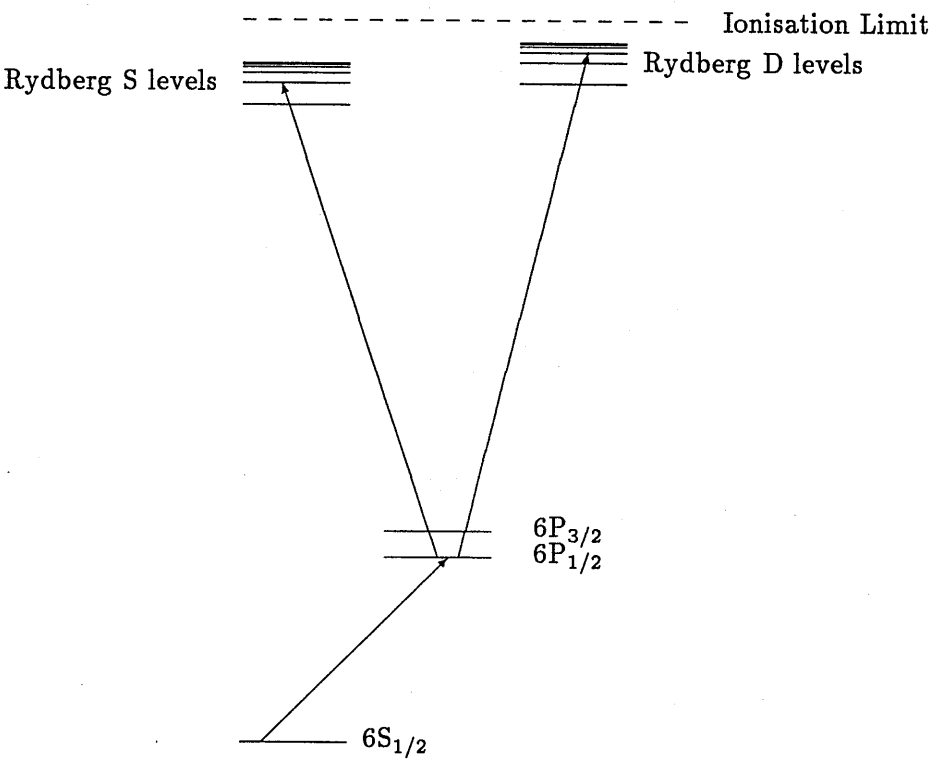

Figure 6.2 Schematic energy level diagram for Caesium, showing some energy levels of interest to the S and D Rydberg level studies. The transitions from either of the 6P levels to the Rydberg levels are at optical frequencies. Both of the 6S-6P transitions are in the infrared. Only transitions involving the $6P_{1/2}$ level are indicated.

infrared radiation: $6S_{1/2}$-$6P_{1/2}$ (894nm) or $6S_{1/2}$-$6P_{3/2}$ (852nm).

In addition to the measurements of broadening constants for the Rydberg transitions, optical echo intensity beats (see chapter 3) could be used to investigate Rydberg level energy separations, Landé g factors and hyperfine coupling constants.

6.2 Stimulated Echoes

The stimulated echo is generated in a two level system by a sequence of three laser pulses [37, 39, 49, 69, 74, 83]. The first and second excitation pulses are separated by a time τ_{12} and the second and third by a time τ_{23}.

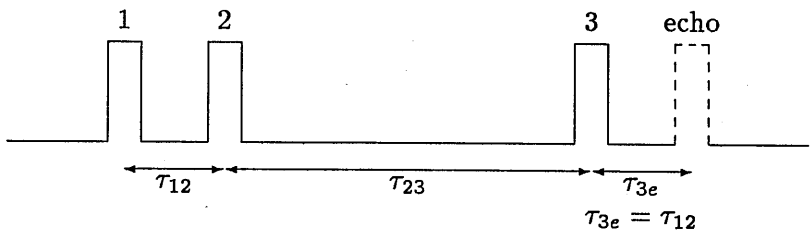

Figure 6.3 Pulse sequence for a stimulated echo experiment.

The third pulse stimulates an echo to occur a time τ_{12} later (see figure 6.3).

For the stimulated echo phase matching can be obtained by a number of configurations with non-collinear excitation pulses. A configuration of special interest, from equation 11a of reference [37], gives the echo wave vector as

$$\mathbf{k}_e = \mathbf{k}_1 - \mathbf{k}_2 + \mathbf{k}_3$$

where $\mathbf{k}_1$, $\mathbf{k}_2$ and $\mathbf{k}_3$ are respectively the wave vectors of the first, second and third excitation pulses. If the first and third excitation pulses counter propagate ($\mathbf{k}_1 = -\mathbf{k}_3$) then

$$\mathbf{k}_e = -\mathbf{k}_2$$

That is, the echo travels in the opposite direction to the second pulse. In addition, if the second pulse propagates at a suitable angle ($\sim$ 20mrad) from the first excitation pulse then the echo propagates in a direction which isolates it from all the other pulses. It should be noted that with beams angled at 20mrad the phase matching condition of section 2.5.2 prevents formation of any two-excitation-pulse echoes. In the experimental arrangement used by Fujita et al for their work on sodium [37] the echo is generated with orthogonal polarisation to the third pulse. Figure 6.4 shows a similar arrangement that was used to obtain the results given in section 5.5.4 for caesium. The different polarisations arise because the second and third excitation pulses are polarised orthogonally to first. No magnetic field is applied. A suitably orientated polariser can then be used to help protect the detector from saturation by stray scattered or reflected light.

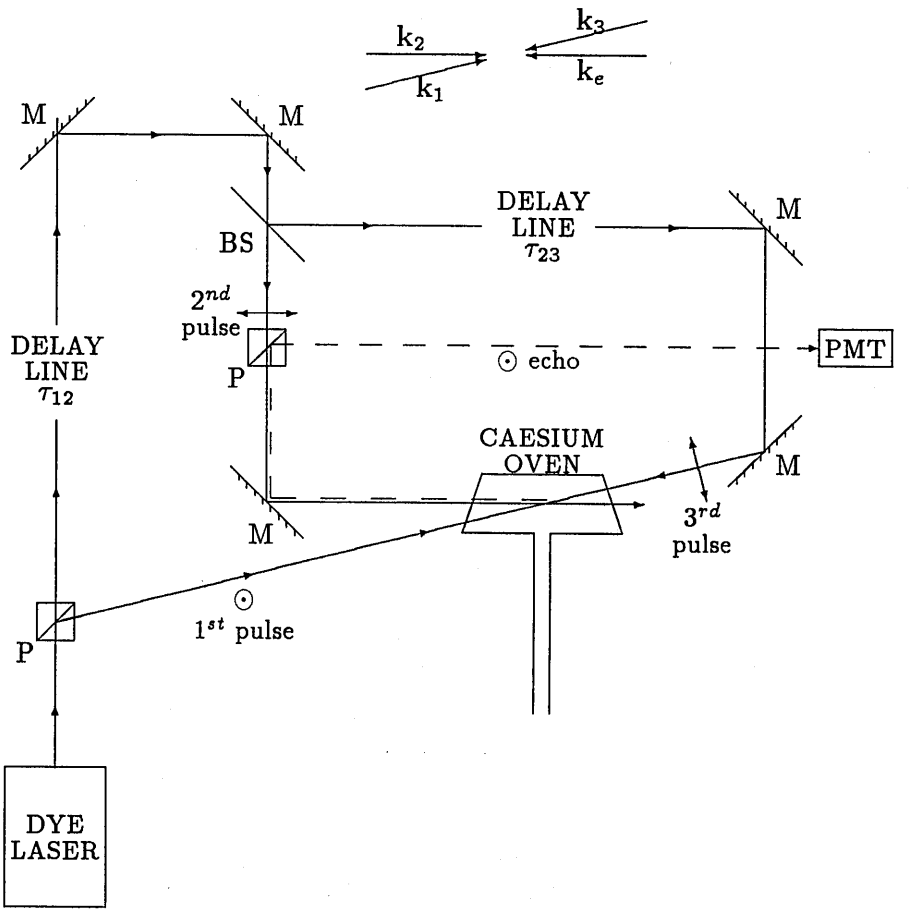

Figure 6.4 Schematic diagram of the stimulated echo optical arrangement. Arrowed lines represent laser beams. BS: beam splitter; M: mirror; P: polariser; PMT: photomultiplier tube. The polarisation of the three excitation pulses and the echo are also shown: 1^{st} pulse and echo ($\odot$); 2^{nd} and 3^{rd} pulses ($\leftrightarrow$).

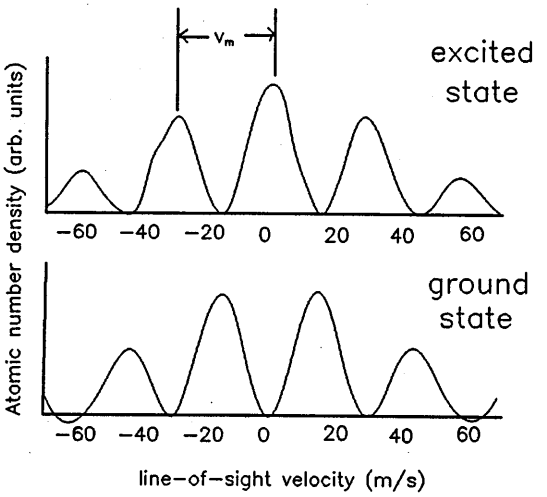

Figure 6.5 Velocity modulation of atomic number density. The Atomic number density, for both ground and excited states, is plotted against line-of-sight velocity following the first two excitation pulses. The overall envelope is the usual gaussian.

The effects of collisions on the echo intensity are now considered. During the intervals τ_{12} and τ_{3e} (see figure 6.3) the echo information is carried by the relative phase of the two level amplitudes (i.e. the optical coherence) and therefore phase interrupting and diffractive velocity changing collisions will result in a reduction of echo intensity (see chapter 4). If the first two pulses have the same polarisation then in the interval τ_{23} the echo information is carried as a velocity modulation of the populations of the level amplitudes [49, 74](see figure 6.5) and not by the relative phase of the level amplitudes. Thus phase interrupting collisions do not affect the echo during this interval. The velocity modulation of the population, which is induced by the first and second excitation pulses [49], has a period, v_m, given by

$$v_m = \lambda/\tau_{12} \tag{6.1}$$

where λ is the wavelength of the laser light. Collisions which results in population velocity changes greater than about v_m will disrupt this modulation and this results in a reduction in the echo intensity. Thus during the interval τ_{23} effects of velocity changing collisions on the population with impact

parameters less than, as well as greater than, the Weissklopf radius can be studied. If the first two pulses have orthogonal polarisation then the echo information is carried during τ_{23} by the Zeeman coherences as well as by the population. Yodh et al [95] have measured depolarising cross sections in ytterbium perturbed by noble gases in this way.

The stimulated echo intensity, I_{se}, as a function of perturber pressure, P, (c.f. equation 4.7) [49, 37, 74] is given by

$$\log_e(I_{se}/I_0) = -\beta' P \tag{6.2}$$

where

$$\beta' = \beta_{12} + \beta_{23} + \beta_{3e} \tag{6.3}$$

β_{ij} describes the reduction in echo intensity due to collisions in the interval τ_{ij}. The β_{ij} are functions of the interpulse time intervals τ_{12} and τ_{23}, but for clarity this is not shown explicitly. β' can be determined, using equation 6.2, from experiments like those of section 5.3 with the optical apparatus shown in figure 6.4.

During the intervals τ_{12} and τ_{3e} both phase interrupting and diffractive velocity changing collisions will result in a reduction in echo intensity. The relaxation parameters β_{12} and β_{3e} are therefore the same as the relaxation parameter in two-excitation-pulse echo experiments. That is

$$\beta_{12}(\tau_{12}) = \beta_{3e}(\tau_{3e}) = \frac{1}{2}\beta(\tau) \qquad \text{with } \tau = \tau_{12} = \tau_{3e}$$

where $\beta(\tau)$ is the relaxation parameter for optical coherence of chapter 4. β_{23}, on the other hand, describes the reduction in echo intensity resulting from population velocity changes greater than about v_m (and from depolarising collisions if the first and second pulses have orthogonal polarisations) in the interval τ_{23}. Thus

$$\beta_{23} \neq \frac{1}{2}\beta(\tau_{23})$$

If the second and third pulses occur simultaneously (i.e. $\tau_{23} = 0$) then $\beta_{23} = 0$ (no collisions occur in no time!) and the collisional cross sections determined from $\beta' = 2\beta_{12} = \beta(\tau_{12})$ should be identical to those determined by two-excitation-pulse echo experiments. Such experiments with $\tau_{23} = 0$

were recently performed to check the equivalent two-excitation-pulse echo measurements for certain systematic errors. The results are described in section 5.5.4.

With τ_{23} non zero, β_{23} can be determined using equation 6.3 from the experimental value of β' and the previously determined value of $\beta_{12} = \beta_{3e}$. That is

$$\beta_{23} = \beta' - 2\beta_{12}$$

If the first two pulses have parallel polarisation then the effects of collisions occurring in the interval τ_{23} reduce the echo intensity only if they disrupt the population velocity modulation. Equation 6.1 shows that at large τ_{12} the modulation period, v_m, is small so even small collisional velocity changes will disrupt the velocity modulation and a large β_{23} will be measured. At small τ_{12} v_m is large so only a few collisions have velocity changes that are large enough to affect the modulation. Therefore a small value of β_{23} will be measured. Thus measurements of β_{23} as a function of τ_{12} can be used to determine the probability distribution of velocity changes following a collision. The functional form of the collisional distribution of velocity changes has been investigated by stimulated echo experiments using sodium perturbed by helium [70] and by carbon monoxide [49]. A review of collisional studies using stimulated echoes is given by Le Gouët and Keller [39].

Appendix A

Effective Time For Random Phase Acquisition

In this appendix consideration is given to the effect of the phase reversal induced by the second pulse on the effective time for acquisition of a random phase by an atom suffering a velocity changing collision before the second pulse. This will explain why the integral in equation 4.10 is over a range τ rather than 2τ.

Obviously for terms in the integrand of equation 4.10 that are independent of t integrating over $t = 0$ to $t = \tau$ and then doubling the result is equivalent to integrating over $t = 0$ to $t = 2\tau$. Therefore only the terms dependant on t will be considered in this appendix. This means that only velocity changing collisions will be considered (Γ_{vcc} in equation 4.10). The effective time for acquisition of a random phase following a velocity changing collision can be found by modifying the analysis of section 2.4.

Suppose a collision causing an isotropic velocity change, $\delta\boldsymbol{u}$, occurs before the second pulse at a time $t = t_c$ ($0 < t_c < \tau$). Then equations 2.17 become

$$\begin{aligned} \mathbf{r}(0) = &\quad \mathbf{R} - \mathbf{v}t_c - (\mathbf{v} + \delta\boldsymbol{u})(t - t_c) \\ \mathbf{r}(\tau) = &\quad \mathbf{R} - (\mathbf{v} + \delta\boldsymbol{u})(t - \tau) \end{aligned}$$

The echo macroscopic polarisation is then given by equation 2.18 appropriately modified. Taking $\mathbf{C} = -\frac{in}{2}\mathbf{D}\sin\theta_1 \ \sin^2(\theta_2/2)$ and ignoring terms not

leading to an echo gives

$$\begin{aligned}\mathbf{P}_e(\mathbf{R},t) &= \mathrm{C}e^{i(\mathrm{k.R}-\omega t)} \\ &\times\langle e^{-i\mathrm{k}.\{2(\mathrm{v}t-\mathrm{v}\tau+\,\delta\boldsymbol{u}t-\,\delta\boldsymbol{u}\tau)-(\mathrm{v}t_c+\mathrm{v}t-\mathrm{v}t_c+\,\delta\boldsymbol{u}t-\,\delta\boldsymbol{u}t_c)\}}\rangle_{\mathrm{v},\,\delta\boldsymbol{u},t_c} \\ &\quad +\mathrm{c.c.}\end{aligned}$$

where the angled brackets indicate an average over the velocity changes following collisions ($\delta\boldsymbol{u}$) and the collision times (t_c) as well as over thermal distribution (v). Collecting terms in v and $\delta\boldsymbol{u}$ and cancelling gives

$$\mathbf{P}_e(\mathbf{R},t) = \mathrm{C}e^{i(\mathrm{k.R}-\omega t)}\langle e^{-i\mathrm{k.v}(t-2\tau)}\rangle_{\mathrm{v}}\langle e^{-i\mathrm{k}.\,\delta\boldsymbol{u}(t-2\tau+t_c)}\rangle_{\,\delta\boldsymbol{u},t_c} + \mathrm{c.c.}$$

The average over v is negligibly small except at $t = 2\tau$, when it is unity, thus

$$\mathbf{P}_e(\mathbf{R},2\tau) = \mathrm{C}e^{i(\mathrm{k.R}-\omega 2\tau)}\langle e^{-i\mathrm{k}.\,\delta\boldsymbol{u}t_c}\rangle_{\,\delta\boldsymbol{u},t_c} + \mathrm{c.c.}$$

Thus an active atom suffering a velocity changing collision at time t_c, before the second pulse, effectively accumulates its random phase only over the interval t_c, not over $(2\tau - t_c)$ the time between the collision and the echo time. Thus the maximum time for which such an atom can accumulate its random phase is τ (i.e. when the collision occurs just before the second pulse, $t_c = \tau$). Obviously if an atom suffers a velocity changing collision after the second pulse it accumulates a random phase over the interval $(2\tau - t_c)$, which has a maximum of τ when $t_c = \tau$. Hence the effects of velocity changing collisions are the same in both periods. This explains the factor 2 multiplying the integral in equation 4.10 and why its limits run from $t = 0$ to $t = \tau$.

Appendix B

Instrumental Time Constant Effects

In this appendix the main deviations of the experimental curves from true exponentials are given theoretical consideration. The boxcar gated integrator performs an exponential average of the echo intensity. The equation for exponential averaging is

$$\mathrm{V}(t) = A \int_{-\infty}^{t} \mathrm{I}_e(t') e^{-k(t-t')} dt' \tag{B.1}$$

where $\mathrm{V}(t)$ is the boxcar output voltage at time t, $\mathrm{I}_e(t')$ is proportional to the echo intensity at time t' before t, k^{-1} is proportional to the boxcar time constant and A is a proportionality constant.

In the experiment the pressure is set to increase linearly from time $t = 0$, at a rate ρ_{in}, this can be modelled by

$$\left.\begin{array}{lll} P & = 0 & t < 0 \\ P & = \rho_{in} \mathrm{t} & t > 0 \end{array}\right\} \text{rising pressure} \tag{B.2}$$

The echo intensity is given as a function of pressure by equation 4.7 which can be written as

$$\mathrm{I}_e = \mathrm{I}_0 e^{-\beta P} \tag{B.3}$$

Substituting equation B.3 and equations B.2 into equation B.1 and writing $A' = \mathrm{I}_0 A$ gives the boxcar output voltage for rising pressure, V_{in}, as

$$\begin{aligned} \mathrm{V}_{in}(t) &= A' \textstyle\int_{-\infty}^{0} e^{-k(t-t')} dt' + A' \int_{0}^{t} e^{-\beta \rho_{in} t'} e^{-k(t-t')} dt' \\ &= A' \tfrac{k e^{-\beta \rho_{in} t} - \beta \rho_{in} e^{-kt}}{k(k - \beta \rho_{in})} \end{aligned}$$

or as a function of pressure as

$$V_{in}(P) = A' \frac{k e^{-\beta P} - \beta \rho_{in} e^{-kP/\rho_{in}}}{k(k - \beta \rho_{in})} \tag{B.4}$$

Typical values for these parameters are (for caesium-argon collisions on the 455nm transition with a 126.8ns delay)

$$\begin{aligned} k &\sim 0.3 \text{ s}^{-1} \\ \rho_{in} &\sim 0.0007 \text{ torr/s} \\ \beta &\sim 80 \text{ torr}^{-1} \end{aligned}$$

implying

$$V_{in}(P/\text{torr}) \propto \frac{(0.3)e^{-80P} - (0.056)e^{-430P}}{0.073}$$

Once the pressure has risen to a few millitorr the decay rate of the echo decay curve is not affected by instrumental time constant effects. For the above values when P is greater than 9 mtorr the second exponential term which is due to the instrumental time constant is less than 1% of the first. For this reason the first few data points (the first 9 mtorr for caesium argon 455nm at τ=126.8ns) of the rising pressure curve are ignored (see figures B.1 and 5.13).

For the falling pressure case it is not so obvious what model to use for the pressure decrease. However taking a linear model:

$$\left.\begin{aligned} P &= -\rho_{out} t \quad t < 0 \end{aligned}\right\} \text{falling pressure}$$

and integrating equation B.1 from $-\infty$ to 0. The whole of the falling pressure curve is therefore obtained at times $t < 0$. This equation and equation B.1 gives the boxcar output voltage for falling pressure, V_{out}, as

$$V_{out}(t) = A' \frac{e^{\beta \rho_{out} t}}{k + \beta \rho_{out}}$$

or as a function of pressure as

$$V_{out}(P) = A' \frac{e^{-\beta P}}{k + \beta \rho_{out}} \tag{B.5}$$

The decay rate of this curve is not affected by the instrumental time constant. Comparing this equation with equation B.4 (once the transient time

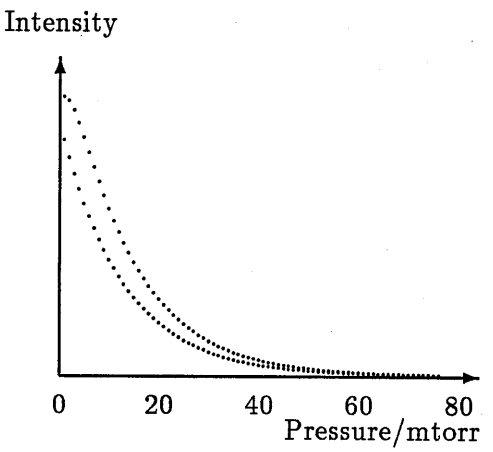

Figure B.1 Theoretical plot showing the effect of the instrumental time constant on the rising and falling pressure exponential curves. The typical parameters used are those given in the text.

constant effects have disappeared) shows that the falling and rising output voltages have different magnitudes; V_{in} is larger than V_{out} at a given pressure by the factor $\frac{k+\beta\rho_{out}}{k-\beta\rho_{in}}$. This can be seen qualitatively in the experimental results (see figure 5.13) and is shown in figure B.1, where equations B.4 and B.5 are plotted using the above typical values with ρ_{out} assumed equal to ρ_{in}. If the data affected by transient time constant effects is ignored, then the relaxation rates determined from the two curves of any experimental run should be the same. This is why in the data analysis (section 5.3.3) if the rising and falling pressure relaxation rates differ by more than 5% the run is rejected.

In some cases corrected curves were obtained by subtracting the instrumental time constant effects from the experimental curves by computer. The relaxation rates determined from these corrected curves, were the same as those determined by the usual method using the unaltered experimental curves. The corrected curves still had slightly rounded tops showing that the transient instrumental effects are not fully explained by the above analysis.

Appendix C

Computer Programmes

The programmes given in this Appendix are for a Hewlett-Packard HP-86/87 micro computer [45, 46] controlling a Biodata microlink III [12] (see section 5.1.2). In section C.1 the programme used to collect the experimental data of section 5.3.2 is given. In section C.2 the programme used to output the semi-log graphs of the data analysis (see section 5.3.3) is given.

The programmes are written in Hewlett-Packard basic [45, 46]. The exclamation mark (!) is the Hewlett-Packard comment symbol and the 'each at' (@) is their goon symbol. 'DISP' is the display to screen command and LOG(x) will give the natural logarithm of x.

C.1 Data Aquisition Programme

```
10 !   GOTO 1490 ! 1490+ for hard copy (1120+ for VDU display)
20 LATCH=0 @ RUNNUMBER=1
30 CLEAR
40 RESET 5
50 DISP "Do you require:          Experimental run  (R)"
60 DISP "                         Quit              (Q)"
70 DISP "                              or"
80 DISP "   Microlink to boxcar and baratron check (C)"
90 DISP "              R,Q or C";@ INPUT TEST$
```

```
100 IF TEST$="R" THEN GOTO 400 ! experimental run
110 IF TEST$="" THEN GOTO 400 ! experimental run
120 IF TEST$="Q" THEN DISP "Finished" @ END
130 IF TEST$="C" THEN GOTO 140 ELSE GOTO 90 !
lines 140-380 run the calibration procedures
140 DISP "Press 'k1' to finish" @ ON KEY# 1 GOTO 30
150 DISP "Set module 00 offset and gain with appropriate
Baratron readings, if necessary adjust Baratron."
160 DISP "    Also set module 01 offset with
Boxcar on function B "
170 DISP " Press 'CONT' to start" @ PAUSE
180 Pold=99999 ! Absurd value to over ride line 340
190 SEND 5 ; TALK 7 SCG 0 MLA ! SCG:- 0-Pressure
200 ENTER 5 USING "#,W" ; X ! gets value from microlink
210 SEND 5 ; UNT
220 P=X*.9315/4095 ! Pressure
230 P=1/10000*IP (P*10000+.5) ! sets miniumum
change that is shown
240 SEND 5 ; TALK 7 SCG 1 MLA ! SCG:- 1-Echo
250 ENTER 5 USING "#,W" ; Y
260 SEND 5 ; UNT
270 E=(1500-Y)*10/1300
280 E=1/900*IP (E*900+.5)
290 SEND 5 ; TALK 7 SCG 2 MLA ! SCG:- 2-1st PULSE
300 ENTER 5 USING "#,W" ; Z
310 SEND 5 ; UNT
320 F=(Z-10)/500
330 F=1/900*IP (F*900+.5)
340 IF P<> Pold THEN Pold=P @ Eold=E @ Fold=F @ GOTO 370 !
these three lines check whether the display needs
changing
350 IF E<> Eold THEN Eold=E @ Fold=F @ GOTO 370
```

```
360 IF F<> Fold THEN Fold=F @ GOTO 370 ELSE GOTO 190
370 DISP USING "15A,Z.4D,5X,6A,DZ.2D,5X,11A,4D.DD" ;
      "Pressure/torr =",P,"Echo =",E,"1st pulse =",F
380 GOTO 190
390 ! Experimental Run Programme
400 ! lines 410-480 set file details
410 IF LATCH=1 THEN GOTO 480
420 LATCH=1
430 DISP "Enter today's date as a four figure number
eg for 17th June enter 1706"
440 DISP "day month";@ INPUT D$
450 IF D$[1,3]=" " THEN DISP
"Don't separate numbers with space." @ GOTO 440
460 DISP "Run number";@ INPUT RUNNUMBER
470 GA$="ARGON" ! Argon is chosen
480 F$="ED"&D$&"7"&VAL$ (RUNNUMBER)&"PI:D701"
490 DISP "Max Pressure in torr";@ INPUT Pmax
500 DISP "You should have checked echo zero and
maximum and the oven temperature."
510 DISP "Valves 1,2 and 3 should all be open."
520 ON KEY# 7 GOTO 990 ! sets interupt/finish key
530 T=0 @ R=0
540 CREATE F$,912,8
550 ASSIGN# 1 TO  F$ ! opens file
560 N=0 @ P0=9999 ! lines 570-620 and 1280-1480 prepare plotter
570 PLOTTER IS 1 @ GCLEAR @ LOCATE 10,130,10,80 @ GOSUB 1280
580 T2=0 @ CSIZE 6
590 MOVE .2*Pmax/.35,.7
600 LABEL USING "DZ.D" ; T2/60
610 MOVE .25*Pmax/.35,.7
620 LABEL "min"
630 CLEAR @ DISP "Press 'CONT' to start."
```

```
640 DISP "Then close swing valve 3 and
crack open needle valve by valve 1."
650 PAUSE ! waits for 'CONT', then starts
660 RT=TIME ! sets RT as the start time
670 ! Start of experimntal run
680 SEND 5 ; TALK 7 SCG 0 MLA ! Pressure
690 ENTER 5 USING "#,W" ; X
700 SEND 5 ; UNT
710 P=X*.9315/4095
720 SEND 5 ; TALK 7 SCG 1 MLA ! Echo
730 ENTER 5 USING "#,W" ; Y
740 SEND 5 ; UNT
750 SEND 5 ; TALK 7 SCG 2 MLA ! 1 st PULSE
760 ENTER 5 USING "#,W" ; Z
770 SEND 5 ; UNT
780 IF R=1 THEN GOTO 800
790 IF P>Pmax THEN R=1 @ PRINT# 1 ; TIME -RT,I,0 @
GOSUB 1740 ! this subroutine informs operator that the
pre-set maximum pressure has been reached
800 IF P>Pmax THEN GOTO 670
810 T1=TIME -RT
820 IF IP (T1/6)=IP (T2/6) THEN GOTO 880
830 PEN -1
840 MOVE .2*Pmax/.35,.7 @ LABEL USING "DZ.D" ; T2/60
850 PEN 1
860 MOVE .2*Pmax/.35,.7 @ LABEL USING "DZ.D" ; T1/60
870 T2=T1
880 IF ABS (P-P0)<.0025*Pmax/.25 THEN GOTO 670
890 I=(1500-Y)*10/1300
900 F=Z/500
910 IF T=1 THEN GOTO 930
920 T=1 @ i=I/.87 @ f=F/.92
```

```
930 PRINT# 1 ; P,I,F
940 PLOT P,I/i @ PEN UP
950 PLOT P,F/f @ PEN UP
960 N=N+1
970 P0=P
980 IF N<> 500 THEN GOTO 670
990 PRINT# 1 ; TIME -RT,-99,0
1000 CLEAR @ DISP N;" data points",IP ((TIME -RT)/6)/10;
" min Total run time"
1010 ASSIGN# 1 TO  * @ RESET 5
1020 DISP "For next run:"
1030 DISP " Check zero echo, at high pressure, by opening
valve 1 and looking at boxcar. If neceesry adjust
boxcar zero."
1040 DISP " Then check and record maximum echo signal by
opening valve 2 and reading meter."
1050 DISP
1060 DISP " Also record oven temperature."
1070 RUNNUMBER=RUNNUMBER+1
1080 DISP
1090 GOTO 40
1100 ! lines 1110-1270 look at individual file contents
1110 CLEAR @ DISP "Offset";@ INPUT B ! ! Allows
trial of zero offsets
1120 F$="ED1111739P:D701" ! 39th file of
11th November 1988 i.e. (11117)(39)
1130 T=0 @ Pmax=.06
1140 GA$=""
1150 ASSIGN# 1 TO  F$
1160 PLOTTER IS 1
1170 LOCATE 10,130,10,80
1180 GCLEAR @ GOSUB 1280 @ MOVE .5*Pmax,1.01 @ DEG @
```

```
LDIR 0 @ LABEL "File No.";F$ ! For plotting
1190 ON ERROR GOTO 1260 ! stops at end of file
1200 READ# 1 ; P,I,F
1210 IF T=1 THEN GOTO 1230
1220 T=1 @ i=(I+B)/.87 @ f=F/.92
1230 PLOT P,(I+B)/i @ PEN UP
1240 PLOT P,F/f @ PEN UP
1250 GOTO 1200
1260 ASSIGN# 1 TO  *
1270 END
1280 Pmax=1000*Pmax ! lines 1290-1480 set up plotter
1290 SCALE 0,Pmax,-1,10.9
1300 MULT=10^IP (LGT (Pmax)) @ VALUE=Pmax/MULT
1310 IF VALUE<2 THEN TICK=.2*MULT @ GOTO labelling
1320 IF VALUE<4 THEN TICK=.5*MULT @ GOTO labelling
1330 IF VALUE<8 THEN TICK=1*MULT ELSE TICK=2*MULT
1340 labelling: LAXES -TICK,111,0,-1,1,1,1
1350 SCALE 0,Pmax,-.1,1.09
1360 LINE TYPE 5
1370 PLOT 0,0 @ PLOT Pmax*1000,0 @ PEN UP
1380 LINE TYPE 1
1390 DEG @ LDIR 0 @ LORG 1 @ CSIZE 3
1400 MOVE .105*Pmax/.35,-.25 @ LABEL GA$;" PRESSURE /mtorr"
1410 MOVE .02*Pmax/.35,1.01 @ LABEL "INTENSITY /arb. units"
1420 LORG 8 @ CSIZE 3
1430 MOVE -(.008*Pmax/.35),.5 @ LABEL "5"
1440 MOVE -(.008*Pmax/.35),1 @ LABEL "10"
1450 MOVE -(.008*Pmax/.35),0 @ LABEL "0"
1460 Pmax=Pmax/1000 @ LORG 1
1470 SCALE 0,Pmax,-.1,1.09
1480 RETURN
1490 ! lines 1500-1730 give hard copy output
```

```
1500 PLOTTER IS 505 @ CSIZE 3
1510 GCLEAR
1520 Pmax=.06 @ GA$="ARGON"
1530 ! six files for hard copy
1540 GOTO 1580
1550 F$="ED1111734P:D701" @ LOCATE 5,68,71,100 @ GOSUB 1620
1560 F$="ED1111735P:D701" @ LOCATE 73,136,71,100 @ GOSUB 1620
1570 F$="ED1111736P:D701" @ LOCATE 5,68,38,67 @ GOSUB 1620
1580 F$="ED1111737P:D701" @ LOCATE 73,136,38,67 @ GOSUB 1620
1590 F$="ED1111738P:D701" @ LOCATE 5,68,5,33 @ GOSUB 1620
1600 F$="ED1111739P:D701" @ LOCATE 73,136,5,33 @ GOSUB 1620
1610 END
1620 PEN 1 @  ASSIGN# 1 TO  F$
1630 T=0 @ GOSUB 1280 ! For plotting
1640 MOVE .5*Pmax,.7 @ DEG @ LDIR 0 @ LABEL "File No.";F$
1650 ON ERROR GOTO 1720 ! stops at end of file
1660 READ# 1 ; P,I,F
1670 IF T=0 THEN i=I/.87 @ f=F/.92 @ T=1 @
MOVE .25*Pmax/.35,1.01 @ LABEL IP (i*5+.5);"mV"
1680 IF P>Pmax THEN PEN 2
1690 PLOT P,I/i @ PEN UP
1700 PLOT P,F/f @ PEN UP
1710 GOTO 1660
1720 ASSIGN# 1 TO  *
1730 RETURN
1740 BEEP 34,200 @ WAIT 200 ! lines 1740-1820 inform
operator that the pre-set maximum pressure
has been reached
1750 BEEP 34,200 @ WAIT 10 @ BEEP 20,200
1760 CLEAR @ DISP "Now leak out gas:"
1770 DISP "   Close valves 1 then 2 and
then open swing valve 3."
```

```
1780 DISP " Having noted 'pressure ratio' take
action at end of run if necessary."
1790 MOVE .2*Pmax/.35,.6
1800 LABEL "Press 'k7' to finish"
1810 ALPHA
1820 RETURN
```

C.2 Data Analysis Programme

```
10 ! File nos. (here 25 to 34) and corresponding offset
20 DATA 25,-.18,-.18,26,-.04,-.04,27,-.03,-.03,
30 DATA 28,-.02,-.02,29,-.03,-.03,31,-.06,-.06
40 DATA 32,-.03,-.03,33,0,0,34,-.05,-.05
50 Pmax=.03 @ LINE$="459nm, F=4"! experimental details
60 X=0 @ Y=0 @ M=0 @ D=0 @ N=0 @ d2S=0 @ XY=0 @ XX=0
70 CLEAR
80 READ F$ ! DISP "FILE";@ INPUT F$
90 F$="ED07097"&F$&"PI:D701" ! files of 25th April 1988
100 ASSIGN# 1 TO  F$
110 GA$="X" ! These files are with xenon
120 IF UPC$ (GA$[1,1])="H" THEN GA$="Helium" @
GAS=4 @ GOTO 190
130 IF UPC$ (GA$[1,1])="N" THEN GA$="Neon" @
GAS=20 @ GOTO 190
140 IF UPC$ (GA$[1,1])="A" THEN GA$="Argon" @
GAS=40 @ GOTO 190
150 IF UPC$ (GA$[1,1])="K" THEN GA$="Krypton" @
GAS=84 @ GOTO 190
160 IF UPC$ (GA$[1,1])="X" THEN GA$="Xenon" @
GAS=131 @ GOTO 190
```

```
170 IF UPC$ (GA$[1,1])="R" THEN DISP "I don't believe you"
180 GOTO 110
190 T=52 ! temperature
300 IF T<270 THEN T=T+273
310 DELAY=221.8 @ OVEN$="short" ! experimental details
320 RT=17.65/DELAY*SQR (T/(.00752+1/GAS))
330 READ B !  rising zero offset
340 READ B2 ! falling zero offset
350 PLOTTER IS 505 ! hard copy device
360 LOCATE 7,65,7,65 ! sets rising pressure plotting area
370 SCALE 0,1,-4.8,.2
380 FRAME
390 MOVE .095,2.3 @ LABEL "Temperature: ";T;"K"
400 MOVE .714,2.3 @ LABEL "Line: ";LINE$
410 MOVE 1.19,2.3 @ LABEL "Oven: ";OVEN$
420 MOVE 1.286,1.7 @ LABEL "Total"
430 MOVE 1.429,2 @ LABEL "Falling Pressure"
440 MOVE 1.667,2.3 @ LABEL "Delay: ";DELAY;"nsec"
450 MOVE .095,2 @ LABEL "Rising Pressure"
460 CSIZE 5
470 MOVE .476,2.6 @ LABEL "logI = -BP + const"
480 CSIZE 3
490 MOVE .119,3 @ LABEL "Logarithmic plot of
echo intensity, I, against ";GA$;" pressure, P."
500 MOVE 1.643,3 @ LABEL " File No. ";F$
510 GOSUB 640  ! draws, scales and labels axes
520 GOSUB 1040 ! plots rising pressure data
530 GOSUB 860  ! calculates best straight line
540 GOSUB 950  ! outputs values
550 LOCATE 80,137,7,65 ! falling pressure plotting area
560 SCALE 0,1,-4.8,.2
570 B=B2
```

```
580 FRAME
590 GOSUB 640  ! draws, scales and labels axes
600 GOSUB 1250 ! plots falling pressure data
610 GOSUB 860  ! calculates best straight line
620 GOSUB 950  ! outputs values
630 DISP "Replace paper and then press 'CONT'" @
PAUSE @ GOTO 60
640 LORG 8 ! rest of programme as described lines 510-620
650 MOVE -.014,-4 @ LABEL "   1"
660 MOVE -.014,-2 @ LABEL " 100"
670 MOVE -.014,0 @ LABEL "10000"
680 LINE TYPE 5
690 MOVE 0,0
700 DRAW 1,0
710 MOVE 1,-4
720 DRAW 0,-4
730 LINE TYPE 1
740 LORG 1
750 MOVE .238,-5.3 @ LABEL GA$;" pressure (mtorr)"
760 CSIZE 3 @ DEG @ LDIR 90
770 MOVE -.095,-3.75 @ LABEL "Echo intensity (arb. units)"
780 SCALE 0,Pmax*1000,1,6
790 MULT=10^IP (LGT (Pmax*1000)) @ VALUE=Pmax*1000/MULT
800 IF VALUE<2 THEN TICK=.02*MULT @ GOTO labelling
810 IF VALUE<4 THEN TICK=.05*MULT @ GOTO labelling
820 IF VALUE<8 THEN TICK=.1*MULT ELSE TICK=.2*MULT
830 labelling: LAXES -TICK,9,0,1,10,30,5
840 SCALE 0,Pmax,-4.8,.2
850 RETURN
860 m=(XY-X*Y/N)/(XX-X*X/N)
870 c=(Y-m*X)/N
880 DISP N
```

```
890 LORG 5
900 XX=-((4.8+c)/m)
910 IF XX>Pmax THEN MOVE Pmax,m*Pmax+c ELSE MOVE XX,-4.8
920 LABEL "*"
930 MOVE 0,c @ LABEL "*"
940 RETURN
950 DEG @ LDIR 0 @ LORG 1
960 CSIZE 3 @ PEN 1
970 MOVE 0,.4 @ LABEL USING "21A,4D,15A" ;
" Cross Section      (";-(m*RT);") sq.Angstrom"
980 MOVE 0,.7 @ LABEL USING "21A,3D.D,9A" ;
" -ve Gradient,B     (";-m;") 1/torr"
990 MOVE 0,1 @ LABEL USING "16A,Z.2D,7A,Z.2D" ;
"             x: ";B-.01;"    <: ";B-.02
1000 MOVE 0,1.2 @ LABEL USING "16A,Z.2D" ;
"             .: ";B
1010 MOVE 0,1.4 @ LABEL USING "16A,Z.2D,7A,Z.2D" ;
" Zero offset o: ";B+.01;"    +: ";B+.02
1020 MOVE 0,1.7 @ LABEL USING "16A,3D,4A" ;
"       Run time ";P;" sec"
1030 RETURN
1040 READ# 1 ; P,I
1050 i=I @ PP=0 @ II=0
1060 LORG 5 @ CSIZE 1
1070 READ# 1 ; P,I
1080 I=I/i+B
1090 IF P>25 THEN GOTO 1240
1100 IF I>0 THEN L=LOG (I) ELSE GOTO 1070
1110 X=X+P @ Y=Y+L @ XY=XY+P*L @ XX=XX+P*P @ N=N+1
1120 PP=PP+P @ II=II+I
1130 IF N MOD 5=0 THEN P=PP/5 @ I=II/5 ELSE GOTO 1070
1140 PP=0 @ II=0
```

```
1150 PLOT P,LOG (I) @ PEN UP
1160 IF P>Pmax THEN GOTO 1070
1170 MOVE P,LOG (I+.02) @ LABEL "+"
1180 MOVE P,LOG (I+.01) @ LABEL "o"
1190 IF I<.01823 THEN GOTO 1070
1200 MOVE P,LOG (I-.01) @ LABEL "x"
1210 IF I<.02823 THEN GOTO 1070
1220 MOVE P,LOG (I-.02) @ LABEL "^"
1230 GOTO 1070
1240 RETURN
1250 X=0 @ Y=0 @ M=0 @ D=0 @ N=0 @ d2S=0 @ XY=0 @
XX=0 @ PP=0 @ II=0
1260 LORG 5 @ CSIZE 1
1270 ON ERROR GOTO 1440 @ READ# 1 ; P,I@ OFF ERROR
1280 I=I/i+B
1290 IF I<-25 THEN GOTO 1440
1300 IF I>0 THEN L=LOG (I) ELSE GOTO 1270
1310 X=X+P @ Y=Y+L @ XY=XY+P*L @ XX=XX+P*P @ N=N+1
1320 PP=PP+P @ II=II+I
1330 IF N MOD 5=0 THEN P=PP/5 @ I=II/5 ELSE GOTO 1270
1340 PP=0 @ II=0
1350 PLOT P,LOG (I) @ PEN UP
1360 IF P>Pmax THEN GOTO 1270
1370 MOVE P,LOG (I+.02) @ LABEL "+"
1380 MOVE P,LOG (I+.01) @ LABEL "o"
1390 IF I<.01823 THEN GOTO 1270
1400 MOVE P,LOG (I-.01) @ LABEL "x"
1410 IF I<.02823 THEN GOTO 1270
1420 MOVE P,LOG (I-.02) @ LABEL "^"
1430 GOTO 1270
1440 OFF ERROR @ ASSIGN# 1 TO  *
1450 RETURN
```

Bibliography

[1] L. Allen and J. H. Eberly *OPTICAL RESONANCE AND TWO-LEVEL ATOMS* (John Wiley & Sons: New York, London, Sidney, Toronto 1975)

[2] S. Aoki *Phys. Rev. A* **20** (5) 2013 (1979) Photon-echo quantum beats on the $7P_{3/2}$-$6S_{1/2}$ transition in cesium

[3] T. Baer *Phys. Rev. A* **18**(6) 2570 (1978) Spherical-tensor treatment of coherent transients

[4] T. Baer and I. D. Abella *Phys. Lett.* **59A** (5) 371 (1976) PHOTON ECHOES ON THE 6S-7P TRANSITIONS IN Cs VAPOR

[5] T. Baer and I. D. Abella *Phys. Rev. A* **16** 2093 (1977) Polarization rotation of photon echoes in cesium in a magnetic field

[6] R. Beach, B. Brody and S. R. Hartmann *Phys. Rev. A* **27** (6) 2925 (1983) Photon echoes in lithium vapor with the use of angled excitation beams

[7] P. R. Berman *Phys. Rev. A* **5** (2) 927 (1972) Quantun-Mechanical Transport Equation for Atomic Systems

[8] P. R. Berman, J. M. Levy and R. G. Brewer *Phys. Rev. A* **11** (5) 1668 (1975) Coherent optical transient study of molecular collisions: Theory and observations

[9] P. R. Berman, T. W. Mossberg and S. R. Hartmann *Phys. Rev. A* **25**(5) 2550 (1982) Collision kernels and laser spectroscopy

[10] P. R. Berman *Les Houches, Session XXXVIII 1982* New trends in atomic physics pp. 451-515 COLLISIONS IN ATOMIC VAPORS

[11] F. Biraben, B. Cagnac, E. Giacobino and G. Grynberg *J. Phys. B: At.*

Mol. Phys. **10** 2369 (1977) Broadening and shift of the sodium 3S-4D and 3S-5S two-photon lines perturbed by noble gases

[12] *Microlink Users Manual* (Biodata Limited, Manchester, England.)

[13] B. Bölger and J. C. Diels *Phys. Lett.* **28A** (6) 401 (1968) PHOTON ECHOES IN Cs VAPOUR

[14] M. v. Borstel, G. Hermann and G. Lasnitschka *Z. Phys. D- At. Mol. Clust.* **9** 15 (1988) Broadening and shift of thallium $nP_{1/2,3/2}$ states (n=6-10) perturbed by noble gases

[15] B. H. Bransden and C. J. Joachain *Physics of atoms and molecules* (Longman: London, New York 1983)

[16] C. Bréchignac, R. Vetter and P. R. Berman *J. Phys. B: At. Mol. Phys.* **10** (17) 3443 (1977) Influence of collisions on saturated-absorption profiles of the 557 nm line of Kr I

[17] R. G. Brewer and R. L. Shoemaker *Phys. Rev. A* **6**(6) 2001 (1972) Optical Free Induction Decay

[18] R. H. Chatham, A. Gallagher and E. L. Lewis *J. Phys. B: At. Mol. Phys.* **13** L7 (1980) Broadening of the sodium D lines by rare gases

[19] S. Y. Ch'en and M. Takeo *Rev. Mod. Phys.* **29** 20 (1957) Broadening and Shift of Spectral Lines Due to the Presence of Foreign Gases

[20] S. Y. Ch'en, E. L. Lewis and D. N. Stacey *J. Phys. B: At. Mol. Phys.* **2** 274 (1969) Broadening of the hyperfine components of Cs I 4555Å line by argon

[21] M. S. Child *Monographs in Theoretical Chemistry* vol. 4 Molecular Collision Theory (Academic Press, London 1974)

[22] C. R. Cowley *The Theory of Stellar Spectra* (Gordon and Breach: New York 1970)

[23] L. J. Curtis and P. Erman *J. Opt. Soc. Am.* **67** (9) 1218 (1977) Distortion effects in measurements of long optical lifetimes

[24] A. V. Durrant and J. Manners *Optica Acta* **31** (10) 1167 (1984) Relaxation of photon echoes by phase-interrupting collision during the second optical pulse

[25] A. V. Durrant and J. Manners *Opt. Comm.* **49** 293 (1984) Photon Echo

Relaxation In Caesium Perturbed By Noble Gas

[26] A. V. Durrant and J. Manners *J. Phys. B: At. Mol. Phys.* **17** L701 (1984) Collision cross sections for the noble-gas broadening of the Cs 6S-7P doublet using photon echoes

[27] EG&G Models 165 and 166 Gated Integrators Operating and Service Manual page IV-8

[28] I. V. Evseev, V. M. Ermachenko and V. A. Reshetov *Sov. Phys. JETP* **60**(4) 687 (1984) Theory of photon echo produced at resonant levels with hyperfine structure

[29] I. V. Evseev and V. A. Reshetov *Opt. Spectrosc.(USSR)* **57**(5) 531 (1984) Photon (light) echo in a magnetic field stimulated by pulses of arbitrary shape

[30] A. V. Evseev, I. V. Evseev and V. A. Reshetov *Opt. Spectrosc.(USSR)* **58**(3) 313 (1985) Polarization properties of stimulated photon echo with the hyperfine structure of resonance levels taken into account

[31] A. Flusberg, R. Kachru, T. Mossberg and S. R. Hartmann *Phys. Rev.* **19**(4) 1607 (1979) Foreign-gas-induced relaxation of Rydberg S andD states in atomic sodium

[32] R. Friendberg and S. R. Hartmann *Phys. Lett.* **37A** (4) 285 (1971) SUPERRADIANT DAMPING AND ABSORPTION

[33] H. M. Foley *Phys. Rev.* **69**(11 & 12) 616 (1946) The Pressure Broadening of Spectral Lines

[34] R. A. Forber, J. E. Thomas, L. Spinelli and M. S. Feld *Spectral Line Shapes* (Proc. 6^{th} Int. Conf. 1982) p.945 TOTAL OPTICAL COHERENCE-PERTURBER COLLISION CROSS SECTIONS USING VELOCITY SELECTIVE PHOTON ECHOES

[35] R. A. Forber, L. Spinelli, J. E. Thomas and M. S. Feld *Phys. Rev. Lett.* **50**(5) 331 (1983) Observation of Quantum Diffractive Velocity-Changing Collisions by Use of Two-Level Heavy Optical Radiators

[36] K. L. Foster, S. Stenholm, and R. G. Brewer *Phys. Rev. A* **10**(6) 2318 (1974) Interference pulses in optical free induction decay

[37] M. Fujita, H. Nakatsuka, H. Nakanishi and M. Matsuoka *Phys. Rev.*

Lett. 42(15) 974 (1979) Backward Echo in Two-Level Systems

[38] J. P. Gordon, C. H. Wang, C. K. N. Patel, R. E. Slusher and W. J. Tomlinson *Phys. Rev.* **179** (17) 3001 (1978) A suitable system for studying the effect of velocity-changing collisions in saturated absorption: Xe He

[39] J-L. Le Gouët and J. C. Keller pp. 309-334 *Spectral Line Shapes* (Walter de Gruyter & Co., Berlin, New York 1985)

[40] J-L. Le Gouët *J. Phys. B: At. Mol. Phys.* **11** (17) 3001 (1978) A suitable system for studying the effect of velocity-changing collisions in saturated absoption: Xe He

[41] J-L. Le Gouët and P. R. Berman *Phys. Rev. A* **17** (1) 52 (1978) Effect of velocity-changing collisions upon coherences in a three-level system

[42] E. L. Hahn *Phys. Rev.* **80** 580 (1950) Spin Echoes

[43] M. Harris, E. L. Lewis, D. McHugh and I. Shannon *J. Phys. B: At. Mol. Phys.* **17** L661 (1984) The full Voigt profile and collision time asymetry for profiles of calcium 442.7nm perturbed by krypton

[44] see for example E. Hecht and A. Zajac *OPTICS* p. 265 (Addison-Wesley: Massachusetts, California, London, Amsterdam, Ontario, Sidney 1974)

[45] *HP-86/87 Operating and BASIC Programming Manual* (Hewlett-Packard Company 1982)

[46] *I/O Programming Guide SERIES 80* (Hewlett-Packard Company 1980)

[47] R. E. Honig and D. A. Kramer *RCA REVIEW* **30** 285 (1969) VAPOR PRESSURE DATA FOR THE SOLID AND LIQUID ELEMENTS

[48] W. R. Hindmarsh and J. M. Farr *Progress in Quantum Electronics vol. 2 part 3* pp.141-213 COLLISION BROADENING OF SPECTRAL LINES BY NEUTRAL ATOMS

[49] R. Kachru, T. W. Mossberg and S. R. Hartmann *Opt. Comm.* **30** (1) 57 (1979) STIMULATED PHOTON ECHO STUDY OF Na($3^2S_{1/2}$)-CO VELOCITY-CHANGING COLLISIONS

[50] R. Kachru, T. W. Mossberg and S. R. Hartmann *J. Phys. B: At. Mol. Phys.* **13** L363 (1980) Noble-gas broadening of the sodium D lines measured by photon echoes

[51] R. Kachru, T. J. Chen, S. R. Hartmann, T. W. Mossberg and P.R. Berman *Phys. Rev. Lett.* 47 (13) 902 (1981) Measurement of a Total Atomic-Radiator–Perturber Scattering Cross Section

[52] R. Kachru, T. J. Chen, T. W. Mossberg and S. R. Hartmann *Phys. Rev. A* **25** (3) 1546 (1982) Relative noble-gas-induced broadening of the *D* lines of atomic lithium

[53] J. C. Keller and J. L. Le Gouët *Phys. Rev. Lett.* **52**(23) 2034 (1984) Stimulated Photon Echo for Collisional Study in Yb Vapor

[54] J. F.Kielkopf and N. F. Allard *J. Phys. B: At. Mol. Phys.* **13** 709 (1980) Determination of Cs(np)–Xe interactions from spectral line profile measurements

[55] H. G. Kuhn *Atomic Spectra* (Longmans: London 1969)

[56] N. A. Kurnit, I. D. Abella and S. R. Hartmann *Phys. Rev. Lett.* **13** 567 (1964) Observation of a Photon Echo

[57] L. Q. Lambert, A. Compaan and I. D. Abella *Phys. Rev. A* 4(5) 2022 (1971) Effects of Nearly Degenerate States on Photon-Echoes Behavior

[58] K. P. Leung, T. W. Mossberg and S. R. Hartmann *Phys. Rev. A* **25**(6) 3097 (1982) Noble-gas-induced collisional broadening of the $6P_{1/2}$-$6P_{3/2}$ transition of Tl by Raman echoes.

[59] E. L. Lewis *Phys. Rep.* **58** (1) 48 (1980) Collisional relaxation of atomic excited states, line broadening and interatomic interactions

[60] E. Lindholm *Archiv. Mat. Astr. O. Fys.* **28B** (3) (1941) Theory of Broadening of Spectral Lines

[61] H. A. Lorentz *Proc. Royal Acad. Amsterdam* **8** (1906) The absorption and emission lines of gaseous bodies

[62] H. Lundberg and S. Svanberg *Z. Physik* **290** 127 (1979) Determination of Natural Radiative Lifetimes and Landé Factors for Highly Excited States in Cesium

[63] N. Lwin, D. G. McCartan and E. L. Lewis *J. Phys. B: At. Mol. Phys.* **9** (6) L161 (1976) Semiclassical collision calculations for the broadening and shift of the sodium D lines by noble gases

[64] J. Manners and A. V. Durrant *Opt. Comm.* **58** (6) 389 (1986) NOBLE-

[65] E. Margenau *Phys. Rev.* 48 755 (1935) Theory of Pressure Effects of Foreign Gases on Spectral Lines

[66] A. A. Michelson *Astrophys. J.* **2** (4) 251 (1895) ON THE BROADENING OF SPECTRAL LINES

[67] D. Mihalas *Stellar Atmospheres* (Freeman: San Francisco 1978)

[68] T. Mossberg, A. Flusberg, R. Kachru and S. R. Hartmann *Phys. Rev. Lett.* **39** (24) 1523 (1977) Tri-Level Echoes

[69] T. W. Mossberg, R. Kachru, S. R. Hartmann and A. M. Flusberg *Phys. Rev. A* **20**(5) 1976 (1979) Echoes in gaseous media: A generalized theory of rephasing phenomena

[70] T. Mossberg, A. Flusberg, R. Kachru and S. R. Hartmann *Phys. Rev. Lett.* **42** (25) 1665 (1979) Total Scattering Cross Section for Na on He Measured by Stimulated Photon Echoes

[71] T. W. Mossberg, R. Kachru and S. R. Hartmann *Phys. Rev. Lett.* 44 (2) 73 (1980) Observation of Collisional Velocity Changes Associated With Atoms in a Superposition of Dissimilar Electronic States

[72] T. W. Mossberg, E. Whittaker, R. Kachru and S. R. Hartmann *Phys. Rev. A* **22**(5) 1962 (1980) Noble-gas-induced collisional broadening of the $3P_{1/2}$-$3P_{3/2}$transition of sodium measured by the trilevel-echo technique

[73] T. W. Mossberg, R. Kachru, K. P. Leung, E. Whittaker and S. R. Hartmann pp. 1093-1110 *Spectral Line Shapes* (Walter de Gruyter & Co., Berlin, New York 1981)

[74] T. W. Mossberg pp. 889-915 *Spectral Line Shapes, Vol. 2* (Walter de Gruyter & Co., Berlin, New York 1983)

[75] P. Münster and J. Marek *J. Phys. B: At. Mol. Phys.* 14 1009 (1981) Determination of cross sections of excitation transter between the fine-structure components of Cs(7^2P), Rb(6^2P) and Rb(7^2P) induced by collisions with rare-gas atoms

[76] J. Pascale and J. Vandeplanque *J. Chem. Phys.* **60** (6) 2678 (1974)

Excited molecular terms of the alkali-rare gas atom

[77] C. K. N. Patel and R. E. Slusher *Phys. Rev. Lett.* **20** 1027 (1968) Photon Echoes In Gases

[78] F. Rostas and J. L. Lemaire *J. Phys. B: At. Mol. Phys.* 4 555 (1971) Low pressure measurement of the broadening and shift of the caesium 4555Å and 4593Å lines by helium and argon

[79] A. Schenzle, S. Grossman and R. G. Brewer *Phys. Rev. A* **13**(5) 1891 (1976) Theory of modulated photon echoes

[80] F. Schuller and W. Behmenburg *Phys. Rep.* **12**(4) 273 (1974) PERTURBATION OF SPECTRAL LINES BY ATOMIC INTERACTIONS

[81] M. Scully, M. J. Stephen and D. C. Burnham *Phys. Rev.* **171** (1) 213 (1968) Photon Echoes In Gaseous Media

[82] R. L. Shoemaker and E. W. Stryland *J. Chem. Phys.* **64**(4) 1733 (1976) Direct measurements of transition dipole matrix elements using optical nutation

[83] R. L. Shoemaker Chapter 3 *Laser and Coherence Spectroscopy* (Plenum Press: New York, London 1978)

[84] G. Smith *J. Phys. B: At. Mol. Phys.* 5 2310 (1972) Collision broadening in the resonance line of calcium

[85] G. Smith *J. Phys. B: At. Mol. Phys.* 8 (13) 2273 (1975) Collision broadening and shift in the 6s-7p doublet of caesium

[86] I. I. Sobelman Chapter 10 *Introduction to the Theory of Atomic Spectra* (Pergamon Press: Oxford, New York, Toronto, Sydney, Braunschweig 1972)

[87] G. L. Squires *Practical Physics* (McGraw-Hill: London, New York, Sydney, Toronto, Mexico, Johannesburg, Panama 1968)

[88] A. P. Thorne *Spectrophysics* (Chapman and Hall & Science Paperbacks: London 1974)

[89] G. B. Ury and L. Wharton *J. Chem. Phys.* **56**(12) 5832 (1972) Absolute Total Scattering Cross Sections of ^{7}Li-Ar

[90] R. Walkup, B. Stewart and D. E. Pritchard *Phys. Rev. A* **29** 169 (1984)

Collisional line broadening due to van der Waals potentials

[91] C. H. Wang *Phys. Rev. B* 1(1) 156 (1970) Effects of Mixing Collisions on Photon Echoes in Gases

[92] V. Weisskopf *ZS. f. Phys.* **75** 287 (1932) Zur Theorie der Kopplungsbreite. 'On the Theory of Pressure Broadening' *ZS. f. Phys.* **77** 398 (1932) Zur Theorie der Kopplungsbreite und der Stoßdämpfung. 'On the Theory of Pressure Broadening and Collision Damping'

[93] J. U. White *J. Opt. Soc. Am.* **32** 285 (1942) Long Optical Paths of Large Aperture

[94] I. V. Yevseyev and V. A. Reshetov *Optica Acta* **29**(1) 119 (1982) Dependence of the photon echo polarization on the second pulse area

[95] A. G. Yodh, J. Golub and T. W. Mossberg *Am. Phys. Soc.* **32**(2) 844 (1985) Collisional relaxation of excited-state Zeeman coherences in atomic ytterbium vapor

"And when echoes had ceased, like a sense of pain was the silence."

Longfellow

Evangeline (1847) 'Part the Second'; II; line 59